Design and fabrication of microscopic 3D printed fiber tip lenses for atomic quantum technology

Thomas Benedikt Beck

Masterarbeit in Physik
angefertigt im Physikalischen Institut

vorgelegt der
Mathematisch-Naturwissenschaftlichen Fakultät
der
Rheinischen Friedrich-Wilhelms-Universität
Bonn

October 2025

I hereby declare that this thesis was formulated by myself and that no sources or tools other than those cited were used.

Bonn, den 04.06.2025 . . . . . .
Signature

1. Gutachter: Prof. Dr. Sebastian Hofferberth
2. Gutachter: Prof. Dr. Stefan Linden

Contents

CHAPTER 1

Introduction

The manipulation, confinement, and probing of ultracold single atoms and atomic ensembles is central to quantum science and atom-based technology. Pivotal elements in these experiments, like optical tweezers[1], magneto-optical traps [2], transmission measurements, and efficient fluorescence collection, require the ability to shape optical beams. These technologies find application in various fields like quantum optics and quantum information [3], many-body physics [4], precision metrology [5], nanophotonics [6], and ultracold collision studies [7]. Existing experimental platforms that integrate these tools with ultracold atoms are predominantly macroscopic, architecturally complex, reliant on extensive calibration, and bound to tightly regulated laboratory conditions. Progress toward compact, robust, and operationally accessible implementations will depend on systematic simplification and further miniaturization.

Classical manufacturing of lenses based on grinding and polishing is limited in terms of scalability and cost-effectiveness for small batch sizes. Femtosecond-laser two-photon polymerization (2PP) lithography enables direct fabrication of customizable three-dimensional micro-optical components with sub-micrometer features and optical-quality surfaces [8]. The technology-opening demonstration of 2PP manufactured micro-optics appeared in 1997 [9]. Direct printing from a digital model reduces process complexity, accelerates design–fabrication iteration, and supports integration of freeform optical surfaces. These advantages have driven rapid expansion of the field. Successful fabrication of early micro-optical elements was shown in 2006 [10], and the release of commercial 3D lithography systems further accelerated progress. In micro-optics, freeform elements [11], stacked lens systems [12], and Fresnel lenses [13] have become prominent. The miniaturization process further enables the integration with optical fibers. Additional integration of functional microstructures on optical fiber tips shows strong potential for optical trapping [14, 15] and arbitrary beam manipulations[16]. Such components can be realized either by direct printing on the fiber facet [17]—when suitable alignment and fabrication infrastructure are available—or by mounting preprinted slip-on structures [18].

The resulting assemblies are extremely compact and lightweight, advantageous where volume, mass, and access are constrained, as in ultracold atom experiments. They add a substantial degree of flexibility to the architecture of the experimental setups. Although the large scale and architectural complexity of conventional ultracold atom experiments constrain their experimental flexibility, microprinted optics offer the potential to significantly reduce system footprint and operational overhead [19]. A key challenge is achieving optically smooth surfaces without relying on conventional manufacturing

techniques such as grinding and polishing. The surface quality of 2PP-printed optics is determined by various factors, including the specifics of the printing process and the properties of the employed resin, both of which require careful optimization. Post-processing methods can further enhance surface quality; however, these approaches often introduce additional complexity as an additional fabrication step and may not be universally compatible with all designs or resin types.

In practice, in-situ printing on fiber facets is limited by fabrication throughput, alignment tolerances, and fabrication process constraints. To mitigate this, the here presented work adopts a ferrule-based slip-on architecture. This approach preserves freeform design flexibility while avoiding direct facet printing. It simplifies assembly and alignment, supports batch fabrication, and facilitates iterative optical and process optimization. The objective is to advance the design and fabrication of such devices and to assess their feasibility for deployment in ultracold atom experiments. In prospective application experiments, it is essential to deliver tightly focused laser beams with high mode quality. Achieving this requires minimizing form deviation and maximizing surface quality of the micro-optical lens. These requirements drive the need for precise control over the fabrication process to ensure optimal optical performance. This work builds upon prior efforts by Berkis[1] and McKeever [20].

Unless stated otherwise, all uncertainty analyses in this work assume Gaussian error distributions. Input uncertainties are assumed uncorrelated and sufficiently small to justify first-order Taylor approximation.

AI-assisted tools were employed in this work for literature querying, language refinement, and code generation.

[1] Internal documentation

CHAPTER 2

Target application and parameters

Rydberg quantum optics experiments exploit the properties of highly excited (Rydberg) states in ultracold atoms to engineer strong, tunable photon–photon interactions, enabling phenomena such as single-photon level nonlinearities, quantum state control of light, and tailored few-photon dynamics. Measuring these effects with high fidelity requires a probe beam whose characteristics are tightly controlled to ensure reproducible coupling to the atomic ensemble. In the present rubidium setup, the probe beam interrogates the atomic cloud and its transmitted power encodes the system state.

Conventionally, this is implemented with a sequence of free-space fiber collimators, macroscopic lenses for focusing, mirrors for beam steering, and wave plates for polarization conditioning before and after the vacuum cell. (Fig. 2.1(a)) shows an exemplary setup by the rubidium experiment of the Nonlinear Quantum Optics Group. This architecture is spatially extended, consuming valuable space around the chamber, sensitive to mechanical drift and external perturbations, and lossy due to the accumulation required optical devices.

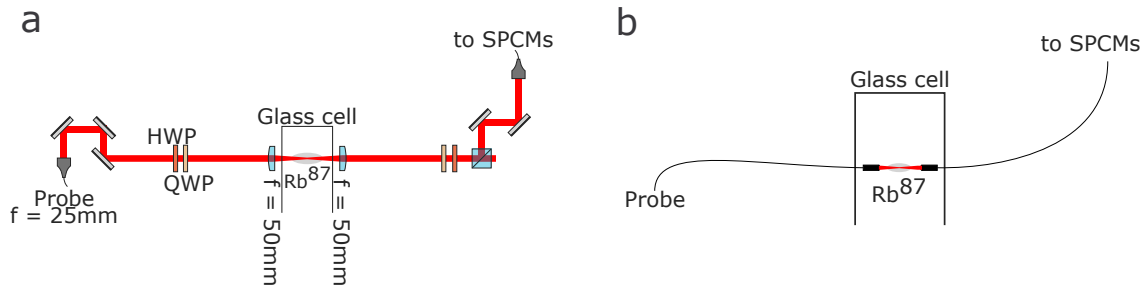

Figure 2.1: Comparison of probe beam configurations in the ultracold rubidium experiment. (a) Conventional setup with macroscopic lenses, mirrors, and wave plates for beam shaping and alignment. Exemplary setup by the rubidium experiment of the Nonlinear Quantum Optics Group. (b) Proposed configuration using fiber tip lenses inside the vacuum chamber for flexible, compact integration.

These constraints motivate replacing the bulky free-space setup with an integrated micro-optic solution: directly fabricated fiber tip lenses positioned inside the vacuum chamber close to the interaction region (Fig. 2.1(b)). In this configuration, the free-space propagation distance is shortened and the component count is reduced, lowering cumulative loss. Passive mechanical stability is

enhanced since the lenses are permanently aligned inside the glass cell and isolated from external perturbations. Additionally, polarization maintaining fibers allow fiber-based polarization control. The approach provides increased coupling efficiency while simplifying the overall architecture, forming the basis for the method developed in this work.

The lenses employed in this work feature a single refractive surface with a spherical profile. To analyze the refraction at such an interface, the ABCD matrix formalism is utilized. Here, we follow the formalism derived from [21]. The ABCD matrix for a spherical interface between two media with refractive indices n_1 and n_2 is given by:

$$M_{\text{interface}} = \begin{pmatrix} A & B \\ C & D \end{pmatrix} = \begin{pmatrix} 1 & 0 \\ \dfrac{n_1 - n_2}{R\, n_2} & \dfrac{n_1}{n_2} \end{pmatrix}$$

where R is the radius of curvature.

The complex beam parameter in medium 1 is

$$q_1 = -L_1 + i\, z_{R,1}, \qquad z_{R,1} = \frac{\pi n_1 w_{0,1}^2}{\lambda_0}$$

where L_1 is the distance from the waist to the interface, $w_{0,1}$ is the waist radius, and λ_0 is the vacuum wavelength.

After traversing the interface, the new complex beam parameter in medium 2 is

$$q_2 = \frac{A q_1 + B}{C q_1 + D}$$

with A, B, C, D as above.

For free-space propagation in medium 2 over a distance d:

$$q_2(d) = q_2 + d$$

The new waist position in medium 2 is found by solving

$$\Re(q_2(d)) = 0$$

and the corresponding Rayleigh range is

$$z_{R,2} = \Im(q_2)$$

The new waist radius is then

$$w_{0,2} = \sqrt{\frac{\lambda_0 z_{R,2}}{\pi n_2}}.$$

The target specifications were defined in collaboration with the rubidium ultracold atom experimental team from the Nonlinear Quantum Optics group to ensure compatibility with the existing apparatus and to meet the required performance criteria. The micro-optic is designed to provide a front focal length of 1 mm and a $\frac{1}{e^2}$ focal spot radius in the range of 3 to 5 µm at the operating wavelength of

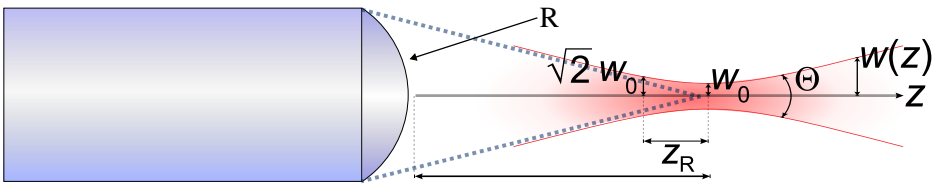

Figure 2.2: Schematic illustration of a fiber tip lens focusing a Gaussian beam. Key beam parameters are indicated for the focused beam behind the lens.

780 nm. A scheme is provided in Fig. 2.2. The beam waist is specified to be smaller than the typical atom cloud size, ensuring that the majority of the beam traverses the atomic ensemble. Beyond that a high quality Gaussian beam profile as well as a $M^2 \approx 1$ beam parameter is desired to ensure reproducible illumination.

The baseline design was modeled in Zemax (Fig. 2.3(c)), which is a raytracing software and performs the calculations described above as well as offering build in optimization tools. The cured IP-S polymer was assigned a refractive index $n = 1.507$ at 780 nm [22]. The single mode fiber was represented with NA = 0.13 and a mode-field diameter of 5.0 µm for the fundamental LP_{01} (Gaussian) mode, consistent with the employed fiber [23]. After removal of the protective coating, the fiber cladding diameter is 125 µm. To restrict the solution space and avoid non-manufacturable optimization solutions, the lens radius of curvature was fixed at 150 µm. Optimization of the total assembly length for minimum RMS focal-plane spot size yields 615 µm. Zemax predicts a corresponding $\frac{1}{e^2}$ focal-plane waist of 4.78 µm (Fig. 2.3(a)), satisfying the target specifications and establishing the geometric baseline. The divergence angle in this configuration is 3.01°. Ray-tracing simulations

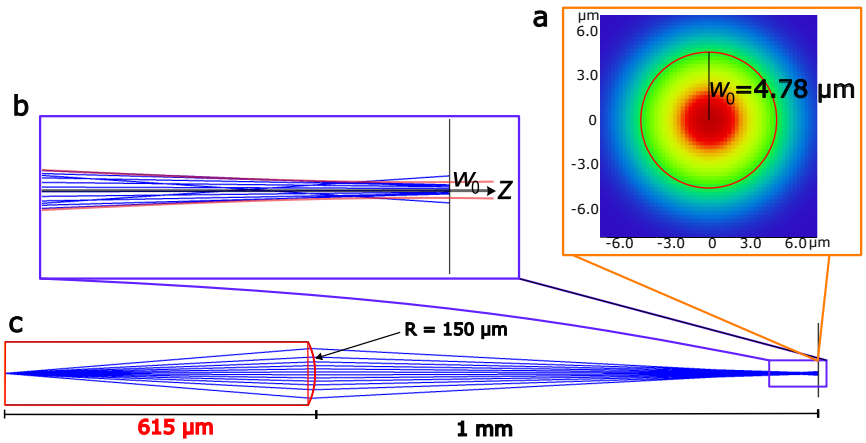

Figure 2.3: Zemax simulation of the baseline design for specification of design dimension and parameters. (a) 2D heatmap of the irradiance in the focal plane, showing a Gaussian intensity distribution. (b) Zoomed-in view of the rays close to the focal plane, showing signs of spherical aberrations. (c) Schematic of the baseline expansion tube and lens design. Variable parameters for the optimization process are written in red.

(Fig. 2.3(b)) indicate residual spherical aberration in the present spherical lens design. Although aspheric corrections are manufacturable with the employed fabrication process, they are deferred here to avoid added fabrication complexity at this developmental stage.

CHAPTER 3

Design, manufacturing and optimization of the ferrule-mounted fiber lens

The development of high-performance optical components through additive manufacturing requires careful consideration of both design parameters and fabrication constraints. Traditional manufacturing methods for optics often limit design complexity and come with scaling limitations. In contrast, 2PP 3D printing enables rapid prototyping and testing of complex optical geometries, allowing for systematic investigation of design variations and manufacturing parameters. This chapter introduces one potential application as a lens for the probing laser in ultracold atom experiments, presents the interim design choice, and discusses the optimization procedure to achieve best optical performance. The methodology demonstrates how digital manufacturing techniques can be leveraged to systematically explore the design space and identify optimal solutions for specialized optical applications.

3.1 Overview of the design

In this section, the design of the ferrule-mounted fiber lens is introduced. Fig. 3.1 shows a cross-sectional wireframe with an interactive 3D model, while Fig. 3.2 provides a technical drawing. The assembly comprises three functional subsystems: ferrule, expansion tube, and lens. The ferrule passively centers the fiber core on the optical axis and forms the mechanical interface to the expansion tube. The expansion tube enlarges the emerging beam to efficiently fill the aperture of the lens. The lens focuses the beam to the target waist. To reduce optimization complexity, development was modularized into these subsystems and performed consecutively. Ferrule and expansion tube designs were iteratively refined until acceptable alignment and beam expansion performance were obtained. In contrast, the lens required a dedicated process-parameter optimization methodology; this strategy is introduced below and initial results are reported. Additional design features and general considerations are summarized in Sec. 3.6. For details on the fabrication and assembly process, see Sec. 4.1 and Sec. 4.2.

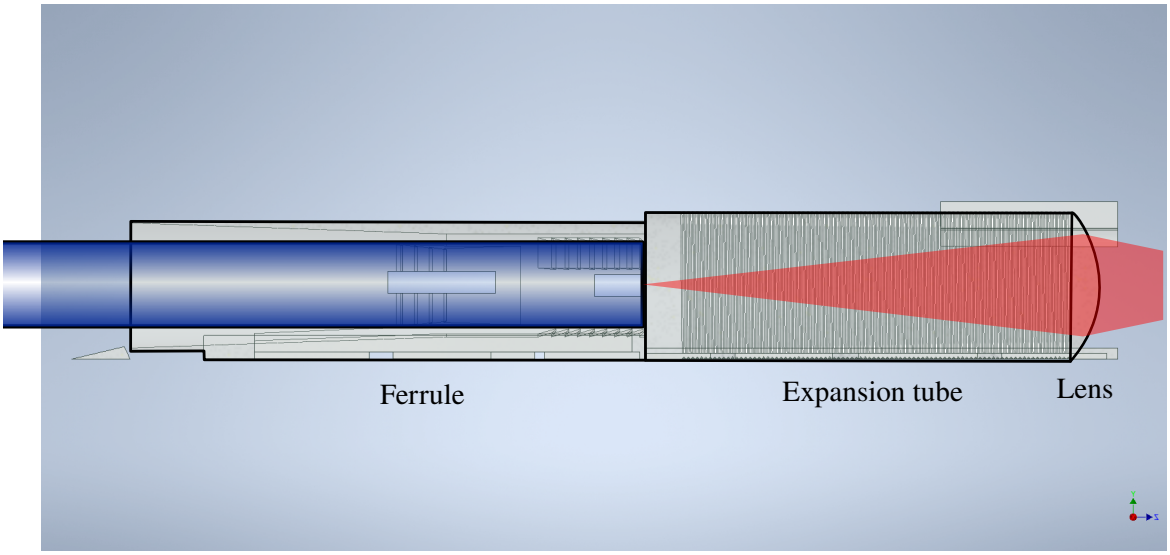

Figure 3.1: Graphical depiction of the final ferrule-mounted fiber lens design as a wire body with concealed edges. An interactive 3D model is provided for detailed inspection.[1]

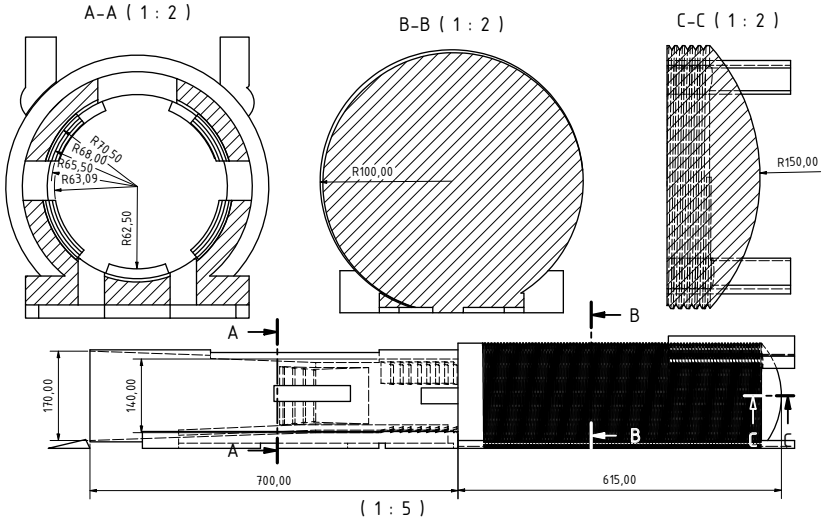

Figure 3.2: Technical drawing of the ferrule-mounted fiber lens with key functional dimensions. At the bottom, the overall assembly is shown at 1:5 scale, highlighting the ferrule taper from 170 µm to 140 µm in diameter, as well as the ferrule and combined length of expansion-tube and lens. At the top, full sections A–A, B–B, and C–C are shown at 1:2 scale. Section A–A through the ferrule shows the tapered shark-teeth structures that enable passive alignment during fiber insertion. Section B–B intersects the expansion tube, indicating a radius of 100 µm. Section C–C is a horizontal section through the center of the spherical lens with radius of curvature $R = 150$ µm. All dimensions are in micrometers.

[1] For this view Acrobat Reader or a compatible viewer is required.

3.2 Ferrule design and optimization

The ferrule (Fig. 3.3 highlighted in red) constitutes the mechanical and passive-alignment interface between the fiber and the expansion-tube. It centers the fiber core on the optical axis and provides axial retention. The total length is 700 µm, while the bore tapers from 170 µm at the entrance to 140 µm near mid-length. The enlarged entrance aperture reduces the likelihood of edge collision and wall abrasion during insertion, while the narrower section increases lateral constraint and thus centering precision. Further reduction of the clear bore would unacceptably raise the risk of wall abrasion during fiber insertion. The cleaved fiber end presents sharp glass edges that can scrape the polymer, generate debris, induce jamming, or contaminate the endface. To mitigate these risks while improving passive centering, shark-tooth microstructures are patterned on the inner bore. Two circumferential rows, azimuthally offset, containing four and eight concentric tooth rings respectively, provide staged guidance. The tooth crests narrow to a minimum inner diameter of 125 µm. During insertion, the teeth deflect elastically, imposing a uniform radial preload that increases static friction and arrests lateral motion, thereby self-locking the fiber in a coaxial position after insertion. Compared to earlier, shorter variants (470 µm) with fewer teeth and a larger minimum inner diameter for the teeth crests (128 µm), the present design exhibits markedly improved centering performance. As shown in Fig. 3.4, the initial design Fig. 3.4(a) produced a substantial decenter in the lens-plane beam spot, whereas the optimized ferrule Fig. 3.4(b) yields good coaxial alignment.

Several openings are added to the ferrule to allow the uncured resin to flow out of the ferrule during the development process. To suppress reflections arising from residual gaps between the fiber and

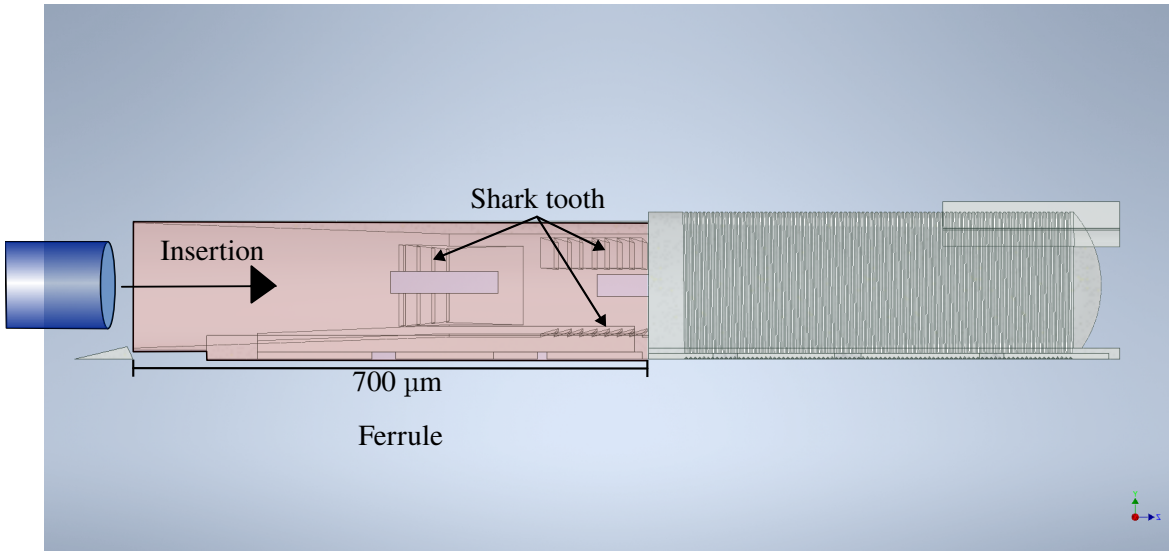

Figure 3.3: Graphical depiction of the ferrule-mounted fiber lens design as a cross section of a wire body with concealed edges. The ferrule is highlighted in red. An interactive 3D model is provided for detailed inspection.[1]

the expansion tube, we apply an index-matching gel [24] to the fiber tip prior to insertion. The gel's

[1] For this view Acrobat Reader or a compatible viewer is required.

refractive index follows a Cauchy-type dispersion,

$$n(\lambda) = 1.4338 + 10520 \cdot nm^2\,\lambda^{-2}. \tag{3.1}$$

At the operating wavelength of 780 nm this evaluates to $n \approx 1.46$, closely matching the printed polymer and silica fiber core of ≈ 1.507 [22] and ≈ 1.46 [23] respectively. Additionally, the gel acts as a lubricant, reducing insertion friction and increasing the achievable insertion depth prior to substrate detachment. Sufficient insertion depth is essential for reliable detachment from the substrate and for pre-aligning the fiber ahead of the final insertion step. For a more detailed description of the fiber insertion process, see Sec. 4.2.

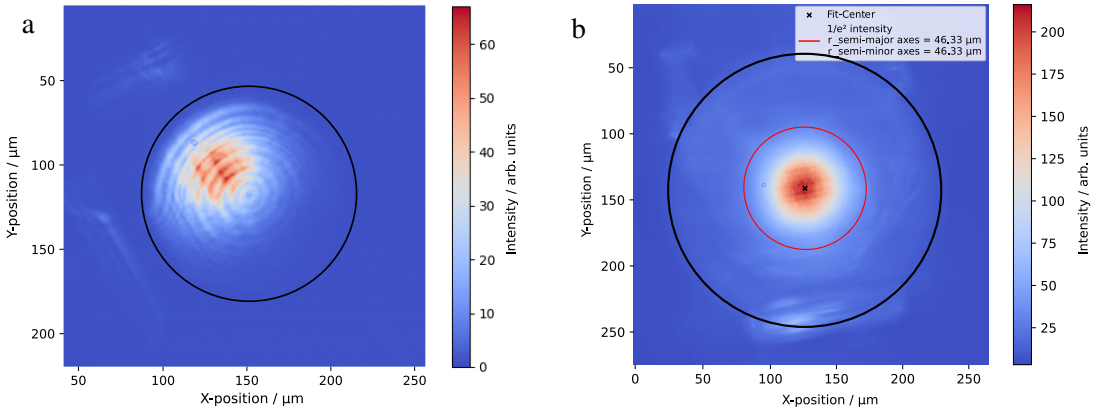

Figure 3.4: Comparison of ferrule designs and their influence on coaxial alignment of the beam in the lens plane. (a) Initial ferrule (length 470 µm) with fewer shark-teeth features and a larger minimum inner diameter (128 µm). Owing to severe beam-profile distortion, no intensity fit is applied. The distortions originate from stray light and interference within the expansion tube; see Sec. 3.3 or remaining gaps at the interface between fiber and expansion tube. The pronounced decenter is nevertheless evident relative to the traced lens contour (black). (b) Optimized ferrule exhibiting a well-centered beam spot. A 2D elliptical Gaussian fit is applied and its $1/e^2$ contour overlaid (red); the fitted beam center coincides with the center of the lens contour center (black).

3.3 Expansion tube design and optimization

The expansion tube (Fig. 3.5) serves to expand the emerging beam such that the lens aperture is optimally filled, thereby minimizing the focal spot radius. This involves a trade-off between minimizing the focal spot radius and increasing clipping losses and reflections at the edge of the expansion tube. Its length, measured to the apex of the lens, is 615 µm, following the Zemax-optimized design. The beam divergence inside the tube is determined by the fiber numerical aperture and the refractive index of the printed polymer; the half-angle follows from

$$\theta = \arcsin(\mathrm{NA} \cdot \frac{1}{n}). \tag{3.2}$$

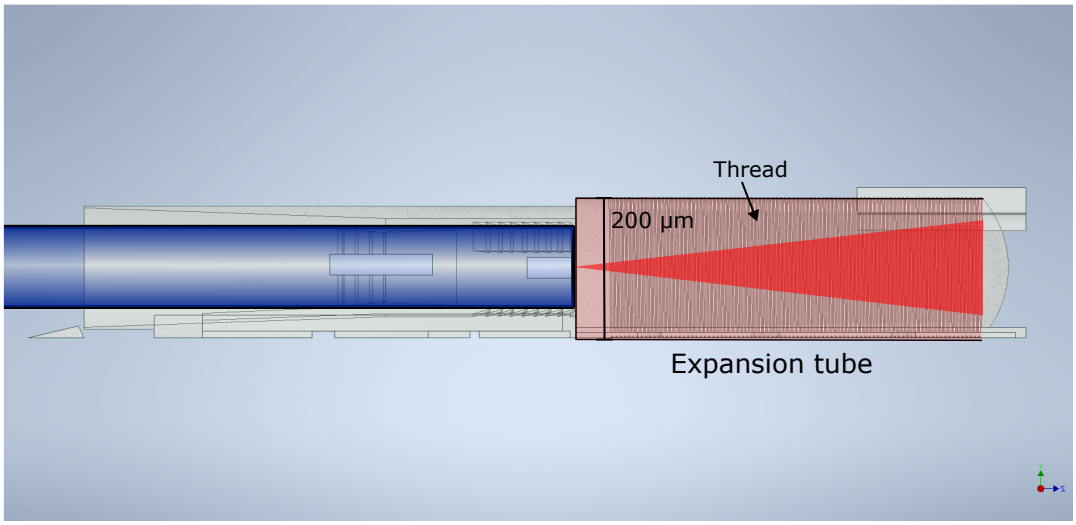

Figure 3.5: Graphical depiction of the ferrule-mounted fiber lens design as a cross section of a wire body with concealed edges. The expansion tube is highlighted in red.

where n is the refractive index of the printed resin and NA is the numerical aperture. The numerical aperture of the fiber is 0.13[23] and the refractive index of the printed resin is 1.507[22] yielding an divergence angle of 4.9°. For the present geometry, the $1/e^2$ beam radius at the lens yields $\approx 53.3\,\mu m$. The finite clear aperture of the tube inevitably truncates the Gaussian beam. To suppress clipping over the required propagation length, a larger diameter is beneficial. Because the expansion tube is fabricated as a solid element, it dominates the assembly mass; excessive mass risks gravitational induced deflection of the structure or supporting fiber, introducing tilt or decenter. A trade-off between transmitted (encircled) power and mechanical stability therefore motivated increasing the tube diameter from 125 µm to 200 µm, based on the following consideration according to the power loss.
For a Gaussian irradiance $I(r) = I_0 \exp(-2r^2/w^2)$, the relative encircled power within radius R can be calculated as:

$$F(R) = \frac{P(R)}{P_{\text{tot}}} = 1 - \exp\left(-\frac{2R^2}{w^2}\right).$$

$$\text{Where } P(R) = 2\pi I_0 \int_0^R r\, e^{-2r^2/w^2}\, dr = \frac{\pi I_0 w^2}{2}\left(1 - e^{-2R^2/w^2}\right)$$

$$\text{and } P_{\text{tot}} = \lim_{R\to\infty} P(R) = \frac{\pi I_0 w^2}{2}$$

Evaluated for our final design($R_{tube} = 100\,\mu m$) and $w = 53.3\,\mu m$,

$$F = 1 - \exp\left[-2\left(\frac{100}{53.3}\right)^2\right] \approx 0.9991,$$

thus 99.91 % of the power is theoretically transmitted and the clipping loss is ≈ 0.09 %.

For comparison, the former design (125 µm diameter tube (R_{tube} = 62.5 µm)) leads to

$$F \approx 1 - \exp\left[-2\left(\frac{62.5}{53.3}\right)^2\right] \approx 0.936,$$

resulting in a clipping loss of ≈ 6.4 %.
It should be noted that the power classified as "lost" is not necessarily absorbed or dissipated, but may instead be reflected back into the beam path, potentially giving rise to interference effects.

Even though clipping losses are minimized, to ensure no back reflections in the optical path, the outer rim of the tube is micro-textured by a shallow thread. This causes scattering of light at the tube edge, further enhancing the suppression of potential interference effects. Performance differences

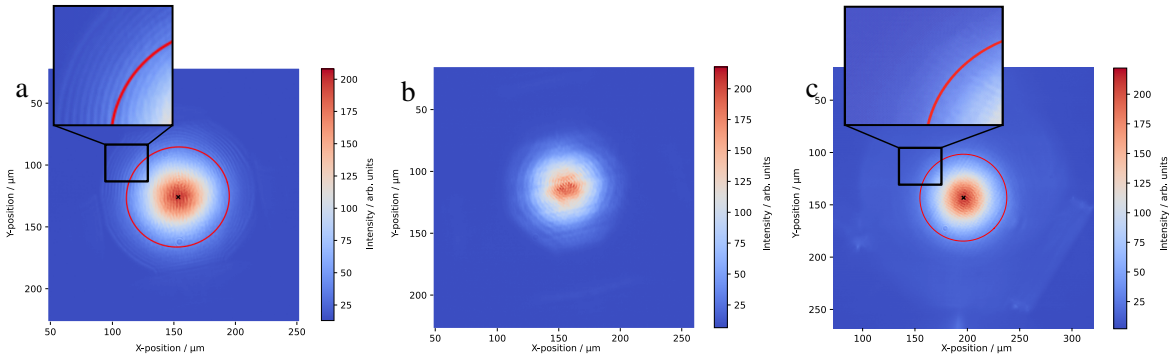

Figure 3.6: Comparison of beam profiles for initial and optimized expansion tube designs. (a) Initial tube (diameter 125 µm, unthreaded) exhibits pronounced concentric interference fringes at the lens plane near the aperture edge. (b) Same initial design imaged 100 µm downstream of the lens: fringes contract toward the beam center and strongly distort the profile. (c) Optimized tube (diameter 200 µm with circumferential threading) yields a near-Gaussian irradiance distribution at the lens plane with the interference rings suppressed. Red contours mark the fitted $1/e^2$ intensity profile.

between the initial and optimized expansion-tube designs are assessed from the recorded beam profiles in Fig. 3.6. The initial design (tube diameter 125 µm, unthreaded) produces pronounced concentric interference fringes (Fig. 3.6(a)) at the lens plane near the aperture edge, which evolve into centrally concentrated rings and severe beam distortion 100 µm beyond the lens (Fig. 3.6(b)). In contrast, the optimized design (tube diameter 200 µm, circumferential threading) yields a near-Gaussian intensity distribution at the lens with the interference structure suppressed (Fig. 3.6(c)).

We evaluated an alternative route in which only a thin-walled shell of the expansion tube is printed by 2PP, followed by ex-situ bulk curing of the resin confined inside the shell using ultraviolet illumination. The motivation was to obtain a highly homogeneous polymer core, thereby suppressing print-induced structural signatures in the propagating beam. However, the refractive index of the polymer (IP-S) depends sensitively on the degree of conversion [25]. Ex-situ UV curing would therefore produce a refractive index different from that achieved by 2PP, leading to a refractive-index mismatch between the 2PP-printed shell and the UV-cured core. For this reason, this approach was not pursued.
An microscope image of the assembly with the optimized ferrule and expansion tube is shown in Fig. 3.7. A visible laser is coupled in the fiber to allow visual inspection of the beam. The beam is

well centered, and the scattered-light envelope indicates that the geometric beam footprint fills the full clear aperture of the lens. The lens in this assembly was not printed with the optimized parameter set: the laser power was evidently too high, as indicated by the weld-like regions between the bottom plate and the lens perimeter.

The clear visibility of the beam within the expansion tube indicates that the tube contributes to scattering, which is particularly evident when compared to the fiber core, where the beam remains invisible. To quantify the associated losses, a measurement was conducted in which the input power was recorded prior to the fiber connector and compared to the output power at the lens. This approach captures the cumulative losses from the fiber connector, the fiber itself, the expansion tube, and the lens. The total measured loss was approximately 11 %. Given that the fiber connector alone introduces significant attenuation, the combined losses are presently considered acceptable. Further optimization of the expansion tube and lens should be pursued once satisfactory lens surface quality has been achieved.

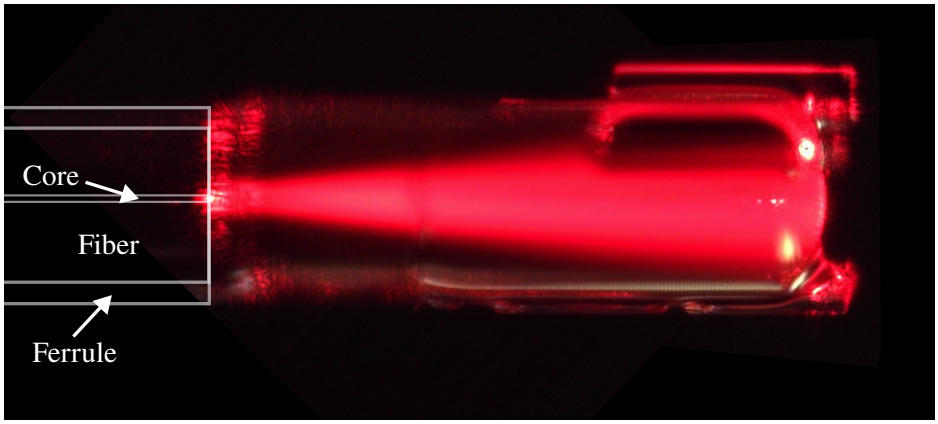

Figure 3.7: Microscope image of the ferrule-mounted fiber lens assembly with optimized ferrule and expansion tube. The beam is well centered on the lens, and the geometric beam footprint fills the full clear aperture of the lens. The lens was printed with excessive laser power, as indicated by the weld-like regions between the bottom plate and the lens perimeter. Because the microscope field of view is limited, the image shown is a mosaic assembled from multiple frames.

3.4 Lens design and optimization

The lens is the critical optical element of the assembly and the most demanding component to fabricate. The design target, introduced in the Zemax analysis in Sec. 2, is a spherical surface with radius of curvature $R = 150\,\mu\text{m}$. Although the geometric specification is simple, realizing the required optical surface accuracy by 2PP remains nontrivial. For the selected IP-S resin, which exhibits a pronounced proximity effect that promotes surface smoothness (see Sec. 4.1.2), the resulting lens surface quality remains highly sensitive to the specific process parameters employed. After mitigation of ferrule-induced alignment errors and suppression of interference effects in the expansion tube, the beam reaches the lens essentially unperturbed. However, near-field beam images recorded immediately downstream exhibit pronounced profile distortions (compare Fig. 3.18) attributable to residual form and mid-spatial-frequency surface errors. These observations identify lens-surface optimization as the

next priority. Given the high dimensionality, ad hoc comparison of beam profiles is insufficient. A structured, quantitative optimization framework was therefore developed.

3.4.1 Lens optimization strategy

A quantitative methodology was required to systematically evaluate the impact of individual printing parameters on lens surface quality. Surface texture errors are commonly classified into three principal categories, as illustrated in Fig. 3.8: (i) figure errors, which result in deviations from the intended focal length; (ii) mid-spatial-frequency errors (waviness), typically spanning 1 to 1×10^3 mm^{-1}, which induce beam deformations; and (iii) high-spatial-frequency errors (roughness), typically in the range 1×10^2 to 1×10^5 mm^{-1}, which cause light scattering and consequently reduce the intensity at the focus.

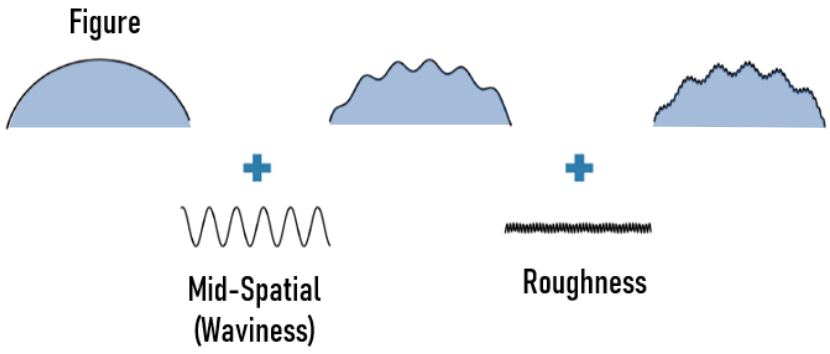

Figure 3.8: Classification of surface spatial frequency range of typical metrology equipment. This graphic is adapted from Edmund Optics [26].

For measurement devices, there is a tradeoff between lateral resolution and field of view. While higher spatial frequencies can be measured with higher lateral resolution, the field of view is typically reduced and therefore larger frequencies cannot be determined with such devices. For our application, the primary objectives are to achieve the specified focal length and a Gaussian beam profile with beam quality factor of $M^2 \approx 1$. Consequently, figure errors and waviness errors are the most critical surface texture deviations at this stage of the project. To quantitatively assess these error classes, a custom scanning white-light interferometer (SWLI) was built to measure lens surface deviations, following the classification scheme presented in Fig. 3.9 and described by [26]. Also compared to atomic force microscopy, the SWLI provides substantially higher throughput (no sample preparation), reduced cost, and greater operational flexibility under standard laboratory conditions. Significant roughness and strong surface curvature are known to induce systematic measurement errors in SWLI metrology, limiting the image field on spherical surfaces and induce reconstruction uncertainties [27]. These limitations have been measured and respected for the specific application. The operating principles, instrument architecture, calibration protocol, and evaluation of associated error sources are presented in Sec. 4.4.

For our analysis, it is particularly important to distinguish between waviness and figure errors. This is accomplished by fitting two different spherical reference surfaces to the reconstructed lens profile: (i)

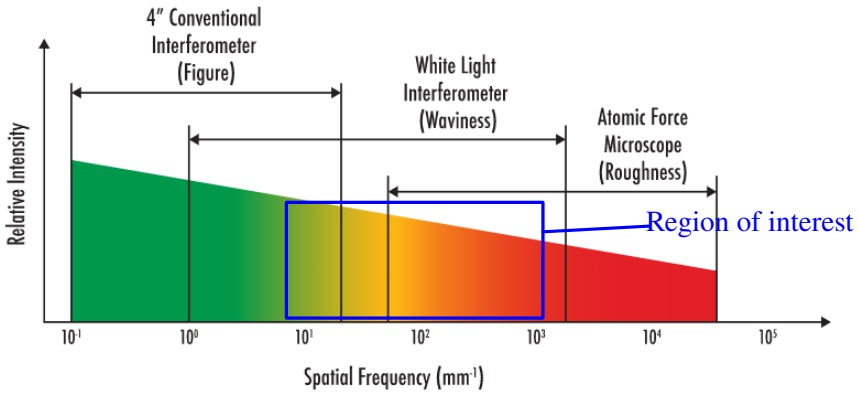

Figure 3.9: Classification of surface spatial frequency range of typical metrology equipment. Relative signal intensity decreases with increasing spatial frequency and requires more accurate measurement devices. This graphic is adapted from Edmund Optics [26].

a sphere with the fixed design radius $R = 150\,\mu\text{m}$, and (ii) a sphere with a variable radius, as illustrated in Fig. 3.10. The variable-radius fit compensates for potential figure errors, so the residuals represent primarily waviness. In contrast, the fixed-radius fit incorporates both figure and waviness errors; by comparing the results of the two fits, figure errors can be isolated. If no figure error is present, the variable-radius and fixed-radius fits converge, yielding identical results. To provide a single quantitative metric, we compute the root-mean-square error (RMSE) surface deviation for both fitting methods.

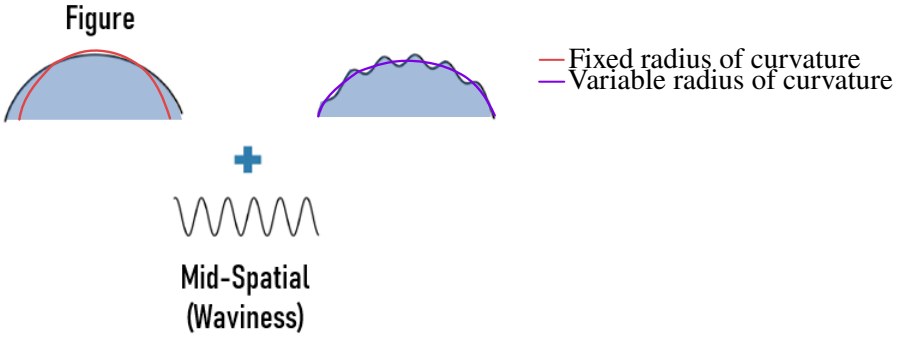

Figure 3.10: Comparison of two spherical fitting methods for quantifying lens surface errors. The reconstructed lens profile (blue) is fitted with (i) a sphere of fixed design radius (red line), and (ii) a sphere with a variable radius (violet line).

Because the fabrication-parameter space is high-dimensional and exhibits nontrivial cross-couplings, a large number of measurements is required to systematically explore this parameter space. Furthermore, both fabrication and reconstruction are subject to uncertainties, necessitating statistically robust evaluation based on a sufficiently large sample population. Assembly fabrication, manual fiber insertion into each ferrule and individual positioning of every specimen in the SWLI are the dominant throughput constraints. To mitigate these limitations, a high-throughput fabrication protocol was

adopted in which only the anterior sub-assembly (lens, support pillars, bottom plate, and a short proximal section of the expansion tube) is printed. An integrated stand stabilizes the construction, which is shown in Fig. 3.11.

The geometry of the anterior sub-assembly is maintained identical to that of the complete device in

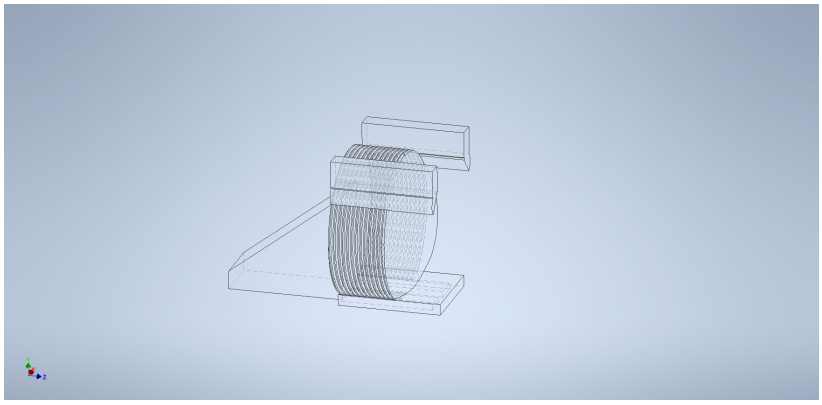

Figure 3.11: Graphical depiction of the lens (lens + short expansion-tube section + stand) with stand as a wire body with concealed edges.

order to eliminate design-related biases in the assessment of surface quality. The components are arranged in a linear array along the substrate edge to facilitate rapid, sequential SWLI measurements. Placement as close as possible to the edge is critical to ensure that the entire reflected signal from the curved surface is captured by the interference objective. A representative microscope image of such an edge array is presented in Fig. 3.12.

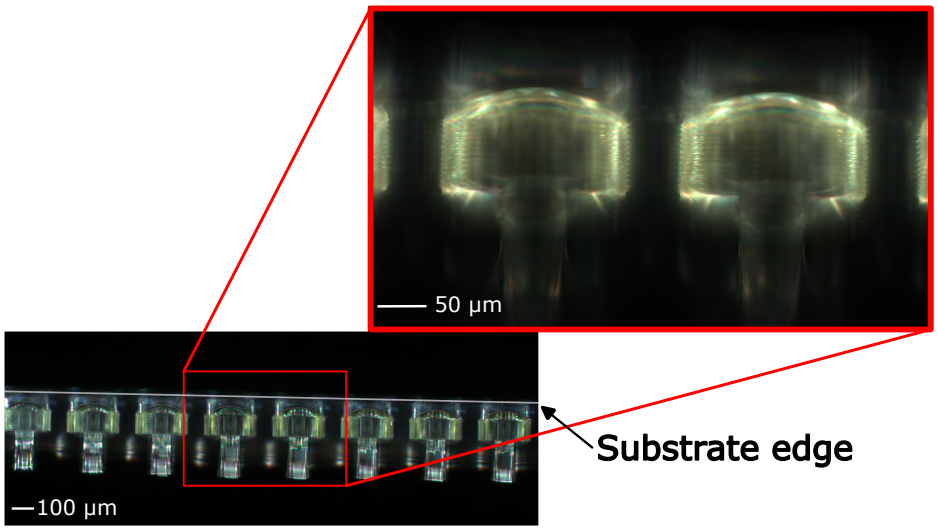

Figure 3.12: Array of lenses with stand (lens + short expansion-tube section + stand) printed along the substrate edge for high-throughput surface metrology. Edge placement ensures the full reflected signal from the curved surface enters the interference objective, enabling rapid sequential measurements.

Application of the optimization strategy and introduction to core print parameters and settings

To test the optimization strategy and isolate the print parameters that govern lens surface quality, it was applied to a targeted subset of fundamental print parameters and settings. Their influence is summarized below, while a detailed description of the underlying two-photon polymerization process and a detailed description of the printing workflow and settings is provided in Sec. 4.1.

For each parameter set, two nominally identical lenses were fabricated and characterized to assess both printer repeatability and the robustness of the surface reconstruction / RMSE evaluation. The paired data in Figs. 3.13, 3.14, and 3.15 show deviations up to 25 % in RMSE values between nominally identical prints, indicating that the current process reproducibility is limited. This highlights the importance of the high throughput approach, which enables the acquisition of statistically significant results.

This first test constitutes a preliminary, predominantly qualitative assessment of the methodology. Because print parameters were not held strictly constant across all runs and the age of resin differs (see Sec. 4.1.2), the results are only directly comparable within the same measurement series.

Printing laser power As discussed in Sec. 4.1, scan speed and laser power are intrinsically coupled. Increasing the scan speed is desirable to reduce fabrication time; however, the reduced deposited energy per unit volume must then be compensated by raising the laser power according to Eq. 4.1. This compensation is not neutral with respect to feature fidelity: a higher laser power enlarges the focal intensity distribution, increasing the volume enclosed by the iso–intensity surface at the polymerization threshold [28]. Resolution is additionally limited by the pronounced proximity effect of the IP-S resin. Excess energy deposition must be avoided because (i) overexposure degrades the optical properties of the cured polymer—visibly manifested as a brownish, burnt appearance—and (ii) the cumulative proximity effect can induce local swelling and weld-like defects at sharp transitions (cf. Fig. 3.7).

To constrain the experimental parameter space, the scan speed was fixed at $50\,\mathrm{mm\,s^{-1}}$, which provides acceptable build times, while later experiments have to be conducted to evaluate the cross effects of laser power and scan speed. The optimization strategy of Sec. 3.4.1 was then applied to lenses fabricated with laser powers spanning 21 to 33 % of the maximum available output (Fig. 3.13). A clearly monotonic increase of both RMSE values with increasing laser power is observed, indicating improved surface quality and reduced figure errors at lower exposure levels. The trend suggests that operating below 21 % laser power would likely yield further reductions in surface error. The value 21 % was selected as it lies only slightly above the polymerization threshold for the chosen scan speed, ensuring robust curing. Future tests at lower powers are recommended; however, only marginal additional improvement is expected before insufficient polymerization leads to surface degradation.

Slicing and hatching distance Hatching distance refers to the lateral spacing between adjacent scan lines, while slicing distance denotes the vertical separation between successive layers. Both parameters must be carefully optimized: they should be small enough to prevent voids between partially overlapping voxels, yet sufficiently large to avoid excessive dose due to the overlap with neighboring laser pulses. The pronounced proximity effect of the IP-S resin facilitates secondary curing of regions between neighboring voxels through accumulated exposure, thereby allowing the use of relatively larger spacings without introducing voids. In this experiment, the hatching distance was

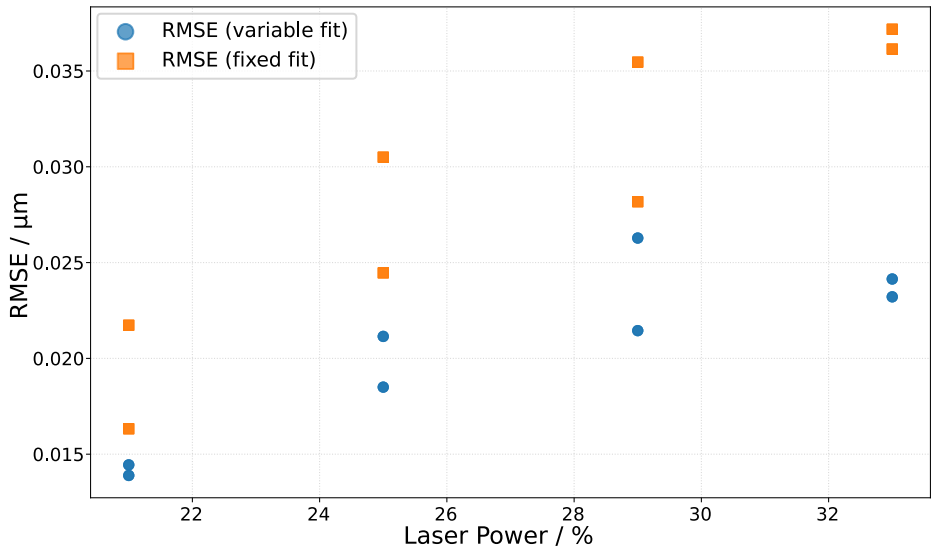

Figure 3.13: Surface error (RMSE) versus laser power for lenses printed at a fixed scan speed of 50 mm s^{-1}. Each power setting was fabricated twice; paired markers demonstrate print and reconstruction reproducibility. Two metrics are shown: RMSE of a spherical fit with variable radius (surface quality) and RMSE of a spherical fit with fixed design radius $R = 150$ µm (shape adherence). Higher laser power monotonically increases both errors; 21 % (just above the polymerization threshold) yields the best surface quality and design conformity.

maintained at 0.1 µm. To evaluate the influence of the slicing distance, the established optimization procedure was applied using representative values of 0.1 and 0.2 µm. As illustrated in Fig. 3.14, reducing the slicing distance to 0.1 µm consistently lowers the RMSE for both variable-radius and fixed-radius spherical fits across the tested laser-power range, indicating enhanced surface smoothness and improved conformity to the nominal design curvature.

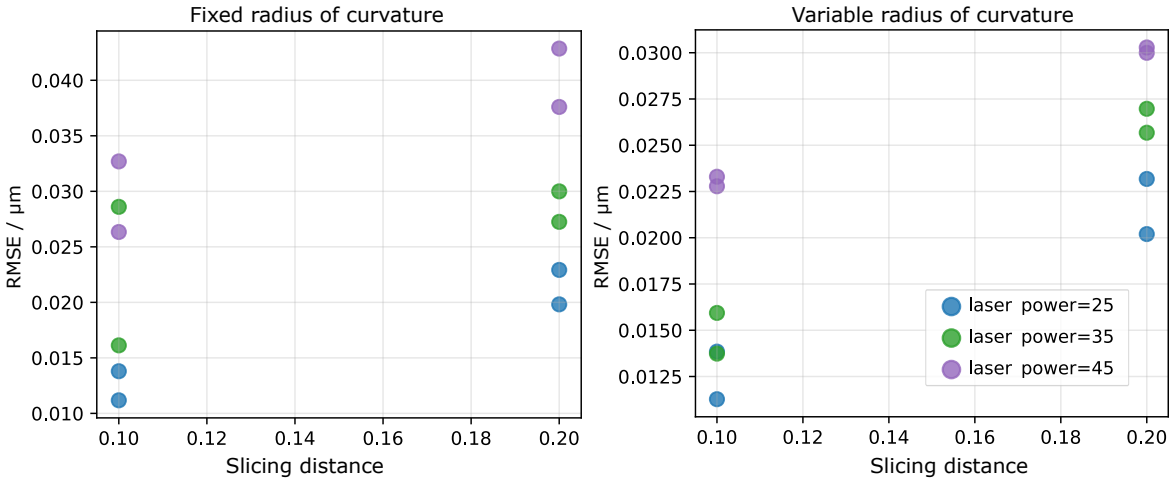

Figure 3.14: Surface error (RMSE) versus slicing distances (0.1 µm and 0.2 µm) for three laser powers. Both the variable-radius and fixed-radius spherical fits are shown. Reducing the slicing distance to 0.1 µm lowers both RMSE across the tested powers, indicating lower waviness and closer adherence to the target figure.

Contour lines Contour lines used in combination with the Perfect Shape setting are, in principle, a promising strategy for fabricating optical surfaces and are explicitly promoted for micro-optics production [29]. For further details see Section 4.1.2. Lenses with 0, 1, 4, and 6 contour lines were fabricated and their surface quality compared to lenses printed without contour lines using the optimization workflow. The corresponding RMSE results are shown in Fig. 3.15. Contrary to expectations, introducing contour lines cause a monotonic increase in the RMSE value for both variable and fixed surface fit. A representative reconstructed surface for a lens printed with 6 contour lines is presented in Fig. 3.16. The reconstruction indicates partial collapse or inward deformation of regions of the lens, accompanied by a camel-hump–like elevation near the center. The underlying cause of this defect is not yet established. The NanoGuide documentation notes that the scan speed of contour trajectories must be adapted to local curvature because the galvanometer mirrors have finite acceleration; overly high speeds on tight circular paths can introduce surface inhomogeneities [29]. In the present case this should intrinsically be mitigated by the Perfect Shape routine, which dynamically adjusts scan speed while compensating deposited dose via laser-power modulation [30]. One plausible explanation is the enforced print order: although DeScribe allows choosing the relative sequencing of core hatching and contour exposure, the individual contour loops themselves are always written from the outside inward when using the standard import tool. The outermost contour(s)—particularly on the lower hemisphere of the lens—have minimal previously cured support and may deform or slump before the inner contours and interior hatch are deposited.

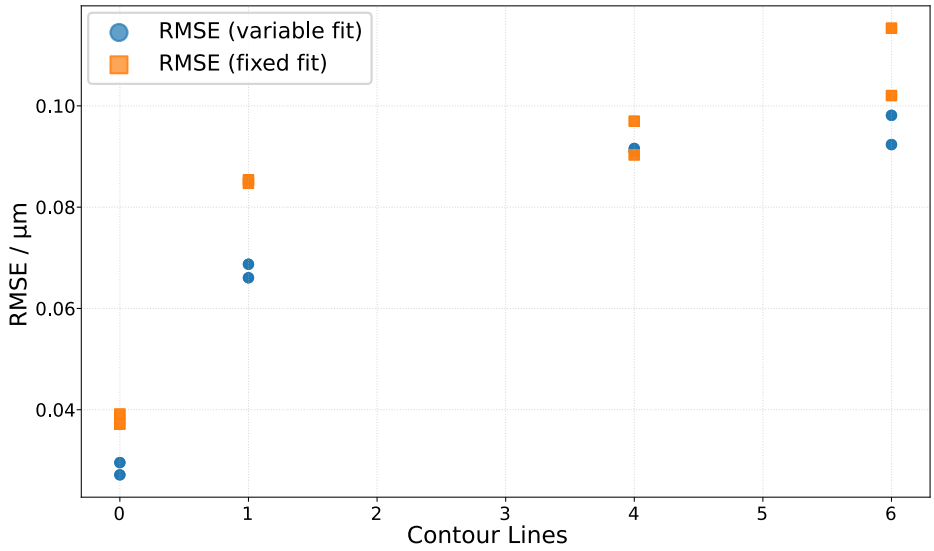

Figure 3.15: Surface error (RMSE) versus number of contour lines $(0, 1, 4, 6)$. Both metrics are shown: variable-radius spherical fit (surface quality) and fixed-radius fit ($R = 150\,\mu m$, design conformity). RMSE increases monotonically with added contour lines, indicating degraded surface quality and poorer adherence to the target curvature, contrary to the expected improvement. Paired markers denote duplicate prints and show good reproducibility of fabrication and measurement.

Given that this procedure is explicitly recommended by Nanoscribe for fabricating optical surfaces, a systematic evaluation in future experiments is strongly warranted, ideally in collaboration with Nanoscribe.

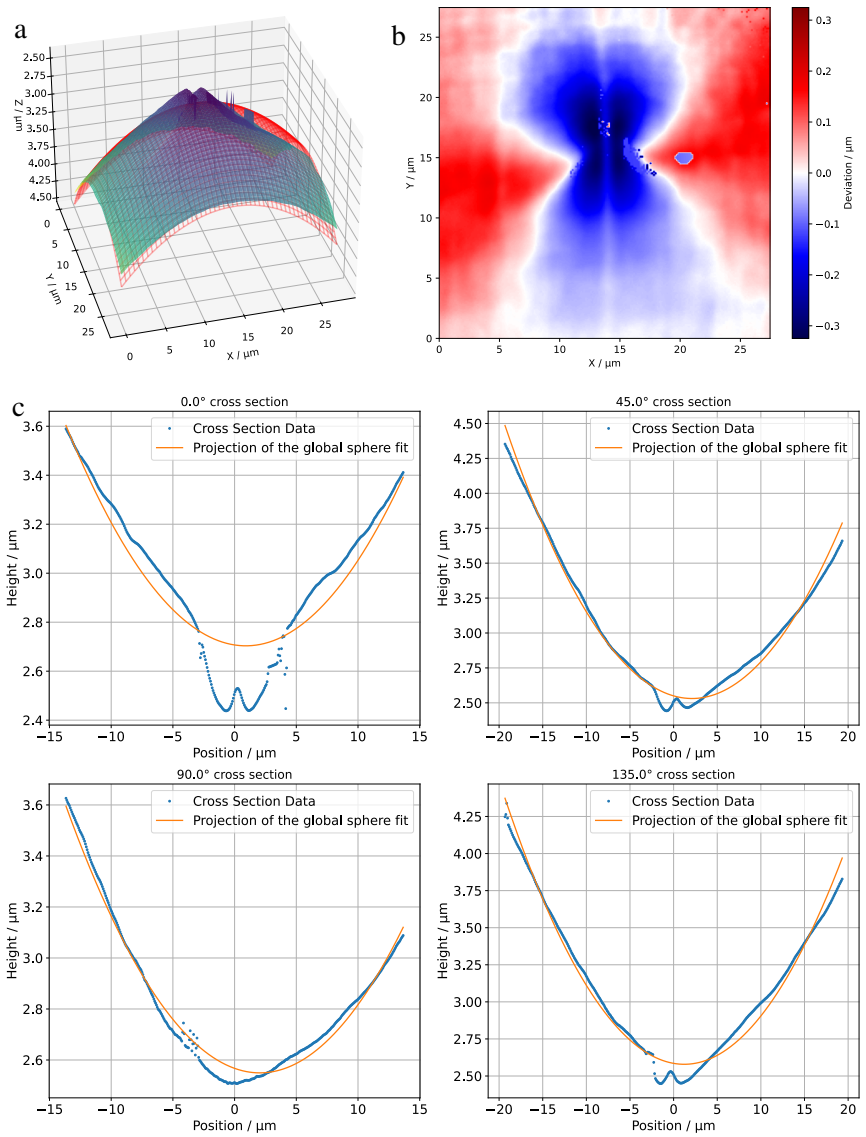

Figure 3.16: Reconstructed surface of a lens printed with 6 contour lines (Perfect Shape enabled). Pronounced form errors are visible: inward deformation of peripheral regions and a central camel-hump elevation, yielding a strongly increased RMSE for both fixed and variable spherical fits. The deformation supports the hypothesis that the current contour exposure sequence (outside–in) induces partial slump before interior hatching cures and stabilizes the structure. (a) 3D surface reconstruction with a spherical fit (fixed radius) to the surface (red mesh). (b) Surface deviation from the spherical fit. (c) Cross sections through the surface reconstruction (blue points) and a projection of the global spherical fit (orange line). An interactive 3D model is provided for detailed inspection.[1] The z- axis is upscaled by a factor of 10 for better visibility. Artifacts are manually removed from the model and leave holes in the surface.

3.5 Printing optimized assemblies

Although lens optimization remains in its early stages, we present and analyze results obtained using the currently best-performing set of print parameters, and compare these to the predictions of the Zemax simulations. The objective is to introduce the measurement methodology and document the present status of the process. To assess and validate both the developed lens optimization strategy and the suitability of the RMSE surface-error metric for this specific application, three assemblies were fabricated at the lowest laser power that ensured reliable polymerization (21 %, corresponding to the minimum RMSE), and three at a higher laser power (33 %, corresponding to the maximum RMSE). While RMSE is a widely accepted metric for optical surface quality [31, 32], its applicability to this particular additively manufactured microlens geometry is explicitly verified in the following.

Using the current best-performing parameter set for the full assembly would require about 30 h of fabrication per device, which is impractical and would severely constrain manufacturing throughput. To enable systematic variation of exposure parameters, the lens was therefore decoupled from the remainder of the structure and fabricated separately with individualized parameter sets. Because DeScribe does not permit assigning distinct process parameters to sub-regions of a single imported part, separate STL files (lens and remaining components) were imported and then spatially adjusted to form the composite assembly. The back part containing the ferrule and the rest of the expansion tube is printed with coarser hatching and slicing distances of 0.2 µm and 0.4 µm, while laser power is again adjusted to be just above the polymerization threshold which is 41 % for the writing speed and resin used for this print. This reduces the manufacturing time of the entire assembly to about 6 h. The tested lens part is produced with the until now best known print parameters:

- Scan Speed: $50\,\mathrm{mm\,s^{-1}}$
- Hatching Distance: 0.1 µm
- Slicing Distance: 0.1 µm
- Laser Power: 21 % (and 33 % for comparison)
- No Contour Lines
- Woodpile ordering

3.5.1 Optical performance evaluation and comparison to simulations

First, we present a detailed analysis of a representative assembly fabricated at a laser power of 21 %, representing the to date best known print parameter set. Beam characterization was performed with a custom-built beam profiler; its design, calibration, and operation are described in Sec. 4.3. The focal length was determined from the axial separation between the beam's smallest width and the physical lens vertex, the latter identified by sharply focusing the microscope on the lens surface. The beam cross section on the lens is shown in Fig. 3.17(a) together with the $1/e^2$ intensity radius fit (red) and the traced contour line of the lens (black). The assembly is illuminated with a flashlight from above to make the lens visible through the scattered light. The center of both circles coincide and are marked with a black cross. The beam is perfectly spherical with a semi-major and minor axis of 46.33 µm. This result differs slightly from the expected beam radius on the lens of 53.3 µm as calculated in Sec. 3.3. This discrepancy can be attributed to fitting uncertainties, likely exacerbated by stray illumination from the auxiliary flashlight and by the slight inward deformation of the printed lens surface that pre-focuses the peripheral beam regions at the lens vertex. The measured focus length is 0.99 mm which deviates by only 1 % away from the target specification of 1 mm.

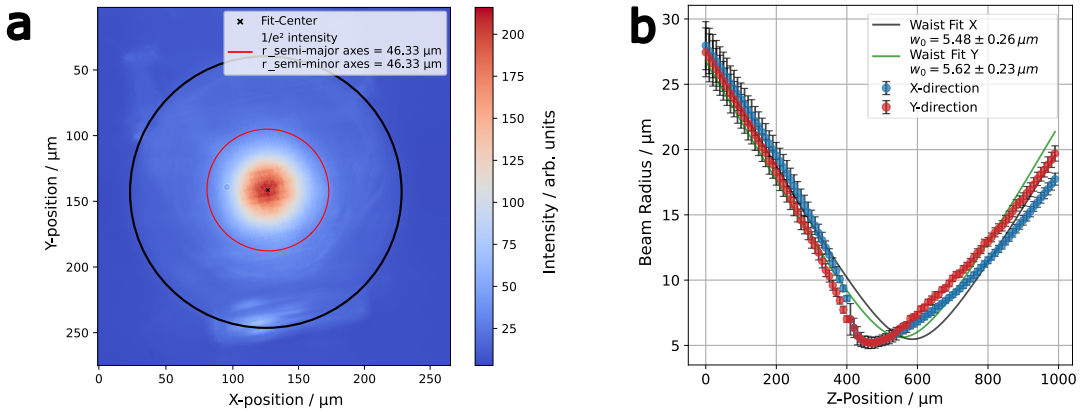

Figure 3.17: (a) Beam profile at the lens for an assembly printed with the optimized lens parameters (laser power 21 %). The red circle marks the fitted $1/e^2$ intensity radius (w = 46.3 µm, identical for x and y); the black contour traces the lens edge; their coincident centers (black cross) indicate good coaxial alignment. (b) Measured beam radii versus axial position obtained from elliptical 2D Gaussian fits (projected onto the fixed x and y axis) together with the fitted beam ellipticity. The width is measured over 1 mm in steps of 10 µm. The waist evolution is fitted using the Gaussian propagation model of Eq. 4.8. The reduced fit quality arises from pronounced asymmetry of the beam on either side of the focus.

The beam-waist evolution was recorded over an axial range of 1 mm in 10 µm increments with the nominal focus located near the center of the scan (Fig. 3.17(b)). The data was fitted with the Gaussian propagation model of Eq. 4.8. Pronounced divergence asymmetry of the width about the focus degrades the quality of the fits and inflates the extracted parameter uncertainties. The fitted $1/e^2$ waist radii are (5.50 ± 0.26) µm and (5.60 ± 0.23) µm for the x and y axis respectively, with corresponding

[1] For this view Acrobat Reader or a compatible viewer is required.

far-field divergence half-angles of 3.5° and 3.3°. These values are in reasonable agreement with the Zemax predictions of a 4.78 µm waist and 3.01° divergence. Further refinement of the lens surface is expected to reduce this asymmetry and improve fit fidelity.

The transverse irradiance profiles (Fig. 3.18) show pronounced deviations from the fundamental mode between the lens surface and the focal region (Fig. 3.18(a)). These deviations largely disappear in and past the waist as the field relaxes toward a near-Gaussian distribution (see 3.18(b) and (c)). An analogous axial evolution has been described for spherical-aberration–dominated propagation [33], where an initially Gaussian beam acquires a halo approaching focus. In the present case the sequence is effectively reversed: a halo-like near field collapses into a cleaner Gaussian beyond the waist, consistent with residual spherical-aberration–induced phase errors imposed by the lens surface.

These distortions are consistently observed across all samples and, given their appearance immediately downstream of the lens, are most plausibly attributed to residual mid-spatial-frequency (MSF) surface texture of the printed lens surface. Analogous effects have been documented in the fabrication of aspheric and freeform optics, where radially symmetric MSF errors similarly induce beam profile perturbations [34]. In those cases, the reported waviness patterns exhibit height amplitudes of approximately 200 nm, which is almost an order of magnitude greater than those observed in the present work.

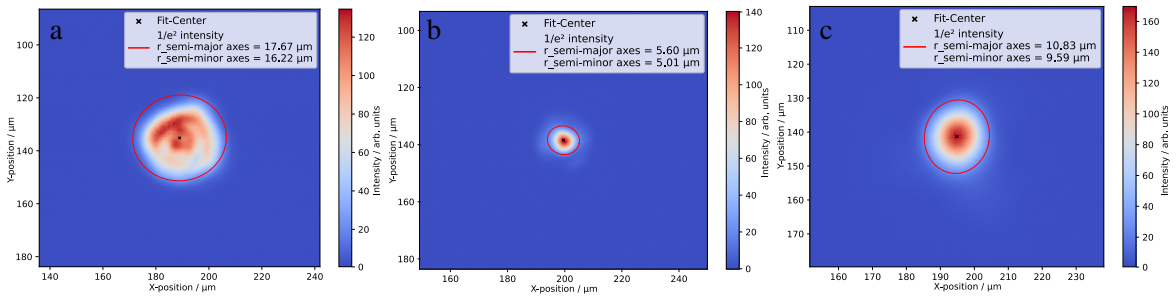

Figure 3.18: Transverse beam profiles recorded upstream (a), in focus (b), and downstream the focus of the beam waist (c). Measured positions are 250 µm apart. Each profile is fitted with a 2D Gaussian from which the $1/e^2$ intensity contours are overlaid (red). Pronounced non-Gaussian halo/ring structures present upstream disappear downstream, consistent with residual spherical-aberration–induced phase errors originating from mid-spatial-frequency (MSF) waviness of the printed lens surface (cf. Fig. 3.19). An increased beam width can be observed upstream of the focus due to beam deformations compared to the beam width in the same distance to the focus downstream.

Surface metrology of lenses fabricated with the above parameter set (Fig. 3.19(a)) confirms the radially symmetric waviness inferred from the beam-profile distortions. The residual height map relative to the fitted sphere with variable radius (Fig. 3.19(b)) exhibits concentric, nearly azimuthal invariant rings. Radial cross-sections overlaid with the projected fitted spherical profile (Fig. 3.19(c)), particularly the 0° section, further highlight the periodic mid-spatial-frequency waves. A horizontal cross section through the lens surface deviations from the spherical fit are provided in Fig. 3.20. There is a recognizable waviness pattern with peak-to-valley amplitudes of ≈ 40 nm and a spatial frequency of ≈ 2 to 5 µm^{-1}. The low amplitude of the waviness in comparison to the used wavelength of 780 nm demands further investigation on their influence on observed beam deformations. The spherical fit with a variable radius parameter yields $R = 151.2$ µm, indicating good agreement with the design

target of 150 µm.

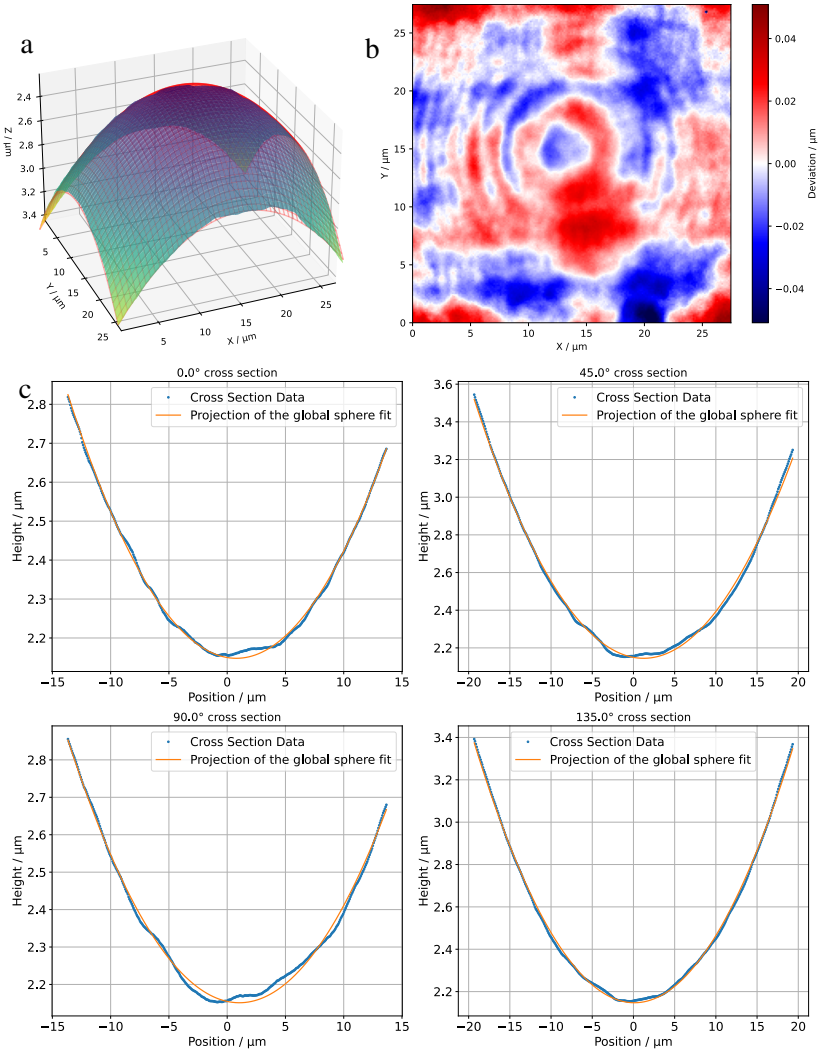

Figure 3.19: 3D surface reconstruction of a representative printed lens (optimized parameters, no contour lines). (a) Reconstructed surface with best-fit sphere (fixed design radius $R = 150\ \mu$m) overlaid (red mesh). (b) Height residuals after subtraction of the fixed-radius sphere showing concentric mid-spatial-frequency rings (peak–valley ≈ 40 nm) that cause the observed near-field beam distortions (see Fig. 3.18). (c) Radial cross-sections (blue) with projected global fixed-radius spherical profile (orange). Variable-radius fit (not shown) yields $R = 151.2\ \mu$m. An interactive 3D model is provided for detailed inspection.[1] The z-axis is upscaled by a factor of 10 for better visibility.

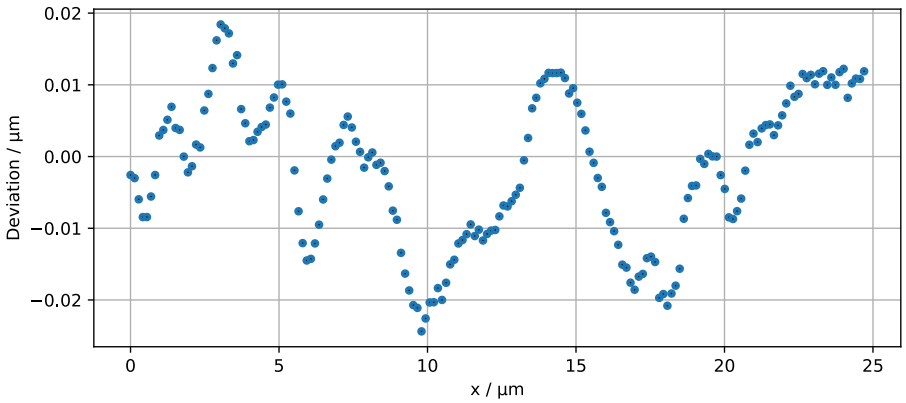

Figure 3.20: Horizontal cross section through the lens surface deviations from the variable radius spherical fit (Fig. 3.19(b)). The pronounced mid-spatial-frequency modulations are clearly visible.

The close agreement between the fitted and nominal radii accounts for the focal length lying within a small deviation of the design specification.

3.5.2 Validating lens surface optimization strategy and RMSE metrics

In this section, we assess the validity of the RMSE-based lens surface optimization strategy by investigating its relationship to key optical performance metrics. Specifically, we examine the correlation between the RMSE metrics, the beam quality factor M^2, and the focal length of printed lenses. Representative beam waist evolution curves for 21 % laser power Fig. 3.21(a) and 33 % laser power Fig. 3.21(b) are presented. As previously discussed, pronounced asymmetry in the waist evolution leads to imperfect fits of the beam waist. The extracted beam quality factors exhibit only minor variations: for 21 % laser power, $M_X^2 = 1.0826$, $M_Y^2 = 1.1056$, and combined $M^2 = 1.0941$; for 33 % laser power, $M_X^2 = 1.0769$, $M_Y^2 = 1.0801$, and combined $M^2 = 1.0785$. Within the current measurement uncertainty, these differences are not statistically significant, and no systematic trend with laser power is observed (Fig. 3.22(a)).

The focal length data (Fig. 3.22(b)) show a clear dependence on the lens printing laser power. Lenses printed at 21 % laser power yield a mean focal length of (0.99 ± 0.02) mm, i.e. a deviation of only 1.0 % from the design target of 1 mm. In contrast, lenses printed at 33 % laser power exhibit a mean focal length of (0.92 ± 0.06) mm, corresponding to a larger deviation of about 8 %. The non-overlap of the mean values within one standard deviation indicates a systematic shift associated with the higher laser power. This supports the interpretation that the lower RMSE obtained from the fixed-radius sphere fit at 21 % laser power reflects improved adherence to the intended radius of curvature, which in turn produces a focal length close to specification.

Overall, the observed correlation between focal-length accuracy and the RMSE metric indicates that the implemented optimization strategy is an effective means to refine the lens surface. However, the observed beam-profile distortions which could be traced back to the MSF surface texture of the lens, have so far prevented further correlation analysis with the M^2 value, requiring further investigation. Once MSF surface defects are mitigated and the near-field deformations suppressed, the correlation between variable fit RMSE and M^2 should be re-examined.

[1] For this view Acrobat Reader or a compatible viewer is required.

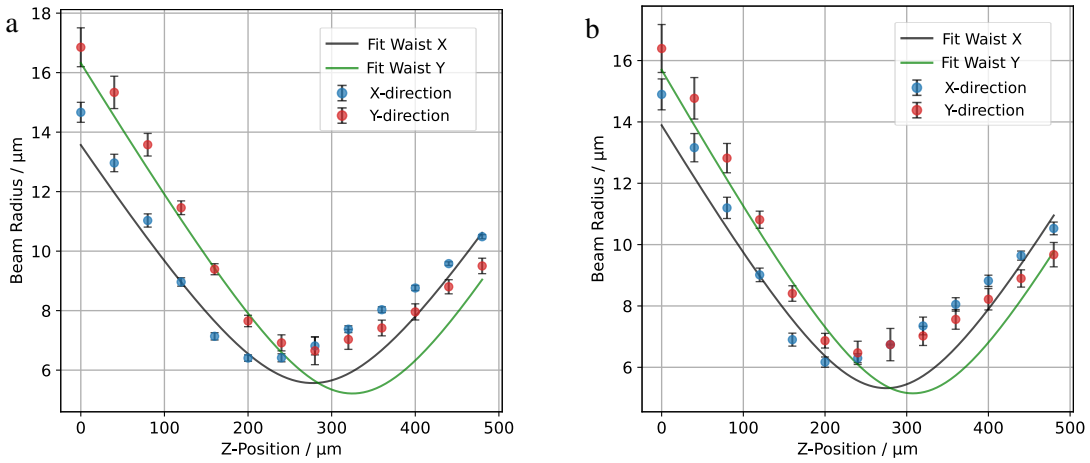

Figure 3.21: Measured beam radii versus axial position for lenses printed at two laser powers. Radii are obtained from elliptical 2D Gaussian fits (projected onto fixed x and y axis). Sampling spans 500 µm in 40 µm steps. The waist evolution in each axis is fitted with the Gaussian propagation model of Eq. 4.8. (a) 21 % laser power (low RMSE). (b) 33 % (high RMSE). Axial asymmetry for both laser powers arise from residual mid-spatial-frequency surface phase errors (see Fig. 3.18).

3.6 General comments on the design

Bottom plate A bottom plate is integrated to provide reliable adhesion of the print to the glass substrate during printing and development. Optimal adhesion is a tradeoff that must be tuned: it should be sufficiently strong to prevent delamination during development, yet weak enough to allow controlled release of the structure when the fiber is inserted and gentle force is applied. This balance is achieved by hollowing the bottom plate, while lateral slits are incorporated to promote drainage of uncured resin during development. The Nanoscribe import software, DeScribe, permits defining a dedicated *Base* region with independent print parameters; this enables a stable parameter set for the bottom plate that is decoupled from the parameters for the rest of the print.

Pillars / alignment flange For the final insertion of the fiber in the ferrule, the retention of the alignment is crucial while still protecting the lens from touching the stop, which the assembly is pushed against. Small pillars are integrated at the end of the expansion tube. These pillars function as mechanical standoffs and as an alignment flange: the assembly can be pressed against a flat reference surface, since the pillar faces are printed perpendicular to the optical axis. As portions of the pillars are intersected by the expanded beam, they can introduce stray light; consequently, their footprint and height are minimized while maintaining sufficient stiffness to avoid bending during insertion, which would otherwise induce tilt or decenter.

Ramp During fiber insertion, the fiber must be pre-aligned with the ferrule bore. If the fiber is pressed against the ferrule edge, there is a substantial risk of damaging the ferrule or causing premature detachment of the assembly from the substrate. Achieving the correct vertical alignment is particularly

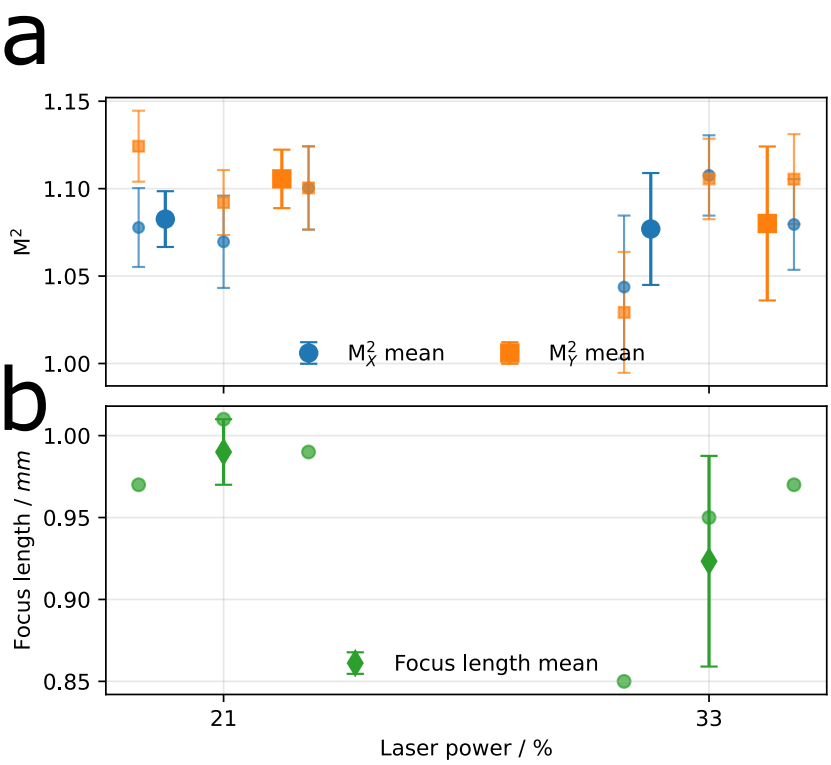

Figure 3.22: Beam-quality factor M^2 ((a)) and focal length ((b)) for lenses printed at 21 % (low RMSE) and 33 % (high RMSE) laser power. No statistically significant trend of M^2 with laser power is resolved; robust extraction of M^2 is impeded by pronounced near-field beam distortions (see Fig. 3.18). In contrast, the focal length shows a clear dependence: lenses printed at 21 % lie much closer to the design target of 1 mm than those printed at 33 %. This agrees with the lower fixed-radius RMSE at 21 %, indicating a correlation between reduced surface form error and focal-length accuracy. Each data point represents a single lens; focal-length uncertainties are smaller than the symbol size. Measurement points for each laser power are slightly shifted on the x-axis for better visibility.

challenging when image sharpness is the only height cue. To mitigate these risks, we added a small ramp in front of the ferrule that passively guides the fiber into the bore. The ramp is printed as a separate feature and remains on the substrate after the assembly has been broken off, thus not affecting the final device.

Orientation of the print The orientation of the print on the substrate is a primary design consideration. Prior work by McKeever[20] employed a vertical build to align the major axis of the elliptical voxel with the optical axis. However, it showed to be disadvantageous because the lens surface must contact the substrate during fabrication, which introduces defects upon release. Rotating the complete assembly by 180° would avoid lens-substrate contact but would require detaching and fixation of the assembly before fiber insertion, complicating handling and alignment. Following former work of our group [1], we therefore adopt a horizontal orientation with the optical axis parallel

[1] Internal documentation

to the substrate. This prevents lens-substrate contact and agrees with observations by Tenbrake[2] that surfaces printed with the voxel major axis parallel to the surface exhibit reduced roughness.

3.7 Future manufacturing strategies

Although priority should remain on the strategy outlined, several additional exploratory concepts could be investigated in future studies if justified.

Different resin and objective for the 2PP process IP-S resin was selected for its pronounced proximity effect, which is expected to promote smooth optical surfaces. However, comparative experiments with resins exhibiting lower proximity effects and higher intrinsic resolution (e.g., IP-Dip, IP-L, IP-G) could be performed to quantitatively verify the suspected advantage of the high proximity effect. The slicing-distance study already indicated that reducing the discretization scale improves surface quality; further refinement could be achieved using the Small Feature workflow provided by Nanoscribe [35]. This would require replacing the 25×, NA 0.8 objective with the 63×, NA 1.4 objective and adopting a high-resolution resin (IP-Dip, IP-L, or IP-G). A principal drawback is the substantially increased fabrication time, as the expansion tube and ferrule would likewise need to be fabricated using the finer parameter set.

Post-processing of the lens The desired approach is to print a lens whose surface meets specification as this is the most reproducible method. This also allows quick and flexible adjustments to the produced lens shape. If, despite further refinement, the achieved surface quality remains inadequate, post-processing could be considered. Laser-induced sub-millisecond thermal reflow has been shown to smooth patterned polymer surfaces by transiently melting the outermost layer and allowing surface-tension–driven relaxation [36]. This method, however, requires an acrylate-based, extreme-ultraviolet (EUV) sensitive resin [29], a condition not satisfied by IP-S. An additional post-processing approach would be oxygen-plasma ashing to gently etch the surface in an attempt to reduce roughness and waviness. However, the effect on the global lens figure (e.g., radius of curvature and potential form errors) is uncertain and may compromise dimensional fidelity.

Compensation of shrinkage and other systematic errors Although initial improvements to lens surface quality and figure should prioritize optimization of print parameters, settings, and overall strategy, certain systematic errors may persist. For example, as described in Sec. 4.1.2, the IP-S resin exhibits intrinsic volumetric shrinkage of 2 to 12 % upon polymerization [22], which can induce systematic deviations from the target geometry. An established approach to mitigate such effects is the iterative compensation methodology reported by Siegle et al. [17]. In this procedure, the surface deviation between the manufactured and nominal shape is measured, the CAD model is modified locally to pre-compensate these errors, and the adjusted design is reprinted. After a small number of iterations, the realized surface converges toward the intended form.

[2] Internal communication

CHAPTER 4

Manufacturing und characterization setups

This chapter presents the experimental setups employed in our research. Each configuration is optimized for specific experimental requirements and measurement objectives, ensuring accurate data acquisition for subsequent analysis. From the outset, a high degree of automation in the characterization setups and scalability of the fabrication and characterization workflows was identified as critical for maximizing throughput. This allows expanding the searchable design space and enabling statistically robust results -especially for lens optimization- in future work based on this.

4.1 3D microprinting with Nanoscribe

The main objective of this work is the fabrication of micro-optical elements using 3D direct laser writing (DLW) with a Nanoscribe Photonic Professional GT+ system. The commercially available platform enables high-resolution additive microfabrication. This chapter provides a concise overview of the relevant principles and, in particular, introduces the process parameters and settings used in this work. More detailed descriptions of the printing process and underlying theory can be found in the masterthesis' of Stachanow [37] and Mc Keever [20] or the PhD thesis of Faßbender [38].

4.1.1 Nanoscribe Photonic Professional GT interface

The Nanoscribe Photonic Professional GT+ is operated with the in-house software *DeScribe* and *NanoWrite*. The former imports 3D models, configures scan strategies and process parameters, and generates the writing trajectories. The latter is used to calibrate and control the system as well as executing the print.

4.1.2 Printing process

The printing process is based on two-photon polymerization (TPP), which enables feature sizes in the sub-micrometer regime [28]. A focused, pulsed laser beam induces polymerization of a photosensitive resin only where the local intensity exceeds the material's polymerization threshold. The size and shape of the written volume element (voxel) can be approximated by the iso-intensity surface of the Gaussian laser beam at the polymerization threshold, which is ellipsoidal in the focal region [39].

The laser beam is steered by a pair of galvanometric mirrors, enabling high scan velocities but constraining the effective write field due to off-axis aberrations. The optical layout is shown in Fig. 4.1. The maximum printable field specified by Nanoscribe is approximately 400 µm in diameter for the 25× objective used in this work. To cover larger areas, the substrate is translated between consecutive writing blocks by the stage translation motor. Adjacent blocks are written with a small intentional overlap to ensure seamless stitching. [40] Each structure is built layer by layer. Within each layer,

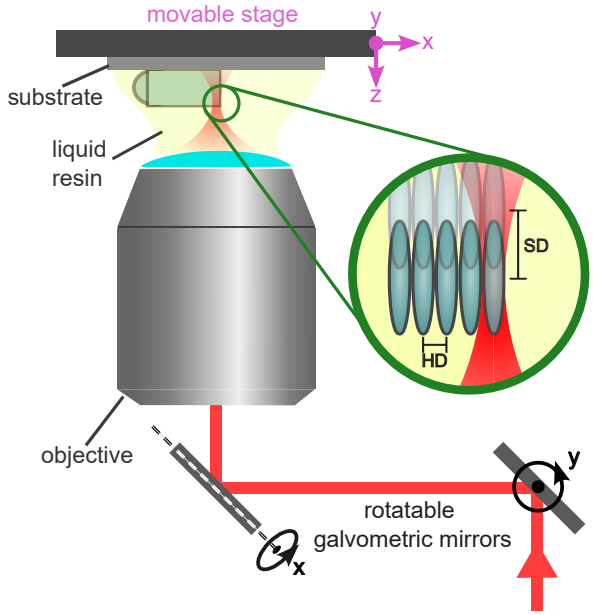

Figure 4.1: Optical layout of the Nanoscribe Photonic Professional GT+. The substrate is positioned by a stage translation motor; an immersion objective is dipped into the photoresin, and the polymerizing laser is focused through the objective. Focus motion is provided by galvanometric beam steering during a writing block whereas stage translation is performed between consecutive blocks. Fabrication is line-based; the lateral hatching distance (HD) and vertical slicing distance (SD) set the line spacings. This graphic is adapted from Stachanow [37].

parallel scan lines (hatching lines) are traced in the x–y plane. The distances between successive layers and lines are the slicing distance (SD) and hatching distance (HD), respectively. Those parameters can be set independently. For the prints in this work, we use *Continuous mode*, in which the laser emission stays uninterrupted for each scan line. Although a single pulse would, in principle, generate an individual voxel, the repetition rate of 80 MHz [41] yields pulse spacings of only a few nanometers at typical scan speeds, so the exposure forms an effectively continuous trace. The cross-section of these written lines are governed primarily by the laser power and scan speed. Laser power sets the voxel size by expanding or shrinking the iso-intensity surface. The influence of scan speed is material dependent and relates to the cumulative dose delivered to the photoinitiator (see Sec. 4.1.2). A rough estimation for compensating laser power and scan speed given by Nanoscribe is

$$\frac{LP_1^n}{v_1} = \frac{LP_2^n}{v_2} \tag{4.1}$$

where LP is the laser power, v is the scan speed, and n is a resin-dependent exponent. For the resin

used in this work (IP-S), $n \approx 3$–3.5 [42]. A schematic representation of a printing block is shown in Fig. 4.2(a), illustrating the arrangement of printed lines separated by the hatching and slicing distances, with lines stacked in woodpile order. An electron micrograph of a fabricated structure is presented in Fig. 4.2(b), providing a visualization of the actual print scale.

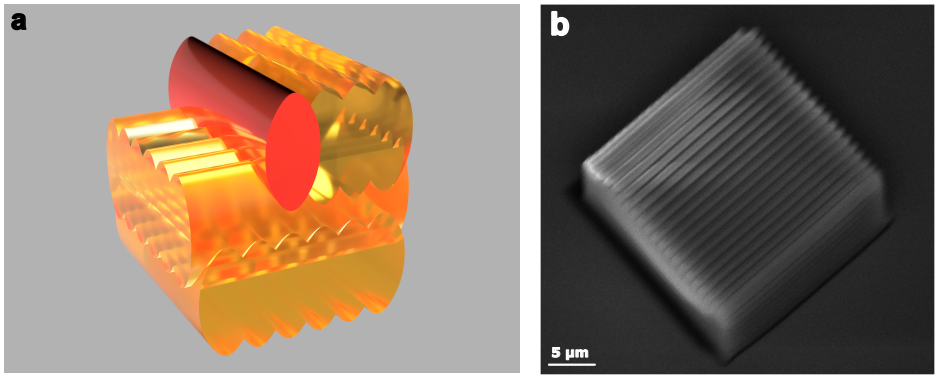

Figure 4.2: Depiction of the printing process. (a) The voxel lines are separated in lateral direction by the hatching distance and in vertical direction by the slicing distance. The red highlighted voxel line serves as a guide to the eye for the fabrication procedure. (b) Electron micrograph of a block written in woodpile order according to the design depicted in (a). This graphic is adapted from Faßbender [38].

Photoresin

Nanoscribe offers a range of resins tailored to different applications. For micro-optical elements, IP-S is recommended because it enables optically smooth surfaces, owing to a high proximity effect [29]. IP-S consists predominantly of monomers and photoinitiators that generate radicals upon excitation; the radicals initiate polymerization of the monomers into long chains that define the written geometry. For a more detailed chemical description, see [38]. The proximity effect refers to the accumulation of effective dose and radical concentration from overlapping pulses, which allows the resin to polymerize through consecutive overlapping laser pulses. This spatial averaging smooths high-spatial-frequency surface texture, thereby reducing roughness [43].

The refractive index of IP-S after curing for a wavelength of 780 nm is $n \approx 1.507$ as stated by Nanoscribe [22]. We follow the development procedure recommended by Nanoscribe, which involves firstly a 20 min bath in Propylene Glycol Methyl Ether Acetate (PGMEA) to remove uncured resin, followed by a 10 min rinse in isopropanol (IPA) to remove residual PGMEA. Finally the print is cured under an UV lamp for 5 min to ensure complete polymerization and as a consequence, consistency of the refractive index.

The resin exhibits a volumetric shrinkage of approximately 2 to 12 % upon polymerization [22]. The specific shrinkage of the structures fabricated in this work has not yet been quantified as the influence of other sources of errors can not be distinguished.

IP-S exhibits gradual performance drift after a syringe is opened, which shifts the effective polymerization threshold. Consequently, *LaserPower* and *ScanSpeed* must be re-established at regular intervals. This is accomplished by fabricating calibration test patterns over a laser-power sweep and identifying the lowest power at which all features are fully formed. Because usable process windows scale relative to this threshold, absolute writing parameters are not directly comparable across different resin batches

or ages; only values normalized to the contemporaneously measured threshold permit meaningful comparison. To date, comparisons for influences of print parameter are made within a single print; consequently, this effect has no influence yet. For future fabrication campaigns, and for establishing an overall optimum parameter set, the effect must be quantified and reported.

Contour lines

To mitigate stair-stepping from the line discretization within each slice, Nanoscribe supports the use of contour lines—perimeter-following trajectories that trace the outer boundary before or after bulk hatching. The intent is to produce a smooth, differentiable outer surface. In Galvo scan mode, tight curvature or sharp corners can challenge the galvo accelerator at high *ScanSpeed*, leading to local over/underexposure and corner rounding. Galvo *PerfectShape* mitigates this by adapting the galvo velocity to the local curvature and co-modulating the *LaserPower* so that the effective dose remains approximately constant despite speed changes, consistent with Eq. (4.1) [30, 44]. Combined with the strong proximity effect of IP-S, this yields the lowest surface roughness reported by Nanoscribe. [29]

4.2 Fiber insertion and alignment setup

Working with micro-optical components requires high precision handling. Therefore, this system for precise alignment and insertion of optical fibers into micro-optical components has been built. The general concept of the design is adapted from McKeever [20] and has been improved as well as adjusted to our micro-optical design.

4.2.1 System architecture

The fiber insertion setup comprises two 3-Axis RollerBlock translation stages from THORLABS (compare [45]). One stage carries an Elliot Scientific fiber holder [46]; the other carries two clamps that secure the glass substrate bearing the printed micro-optical structures. The substrate stage is mounted on a linear rail to (i) provide additional clearance for mounting and (ii) enable post-insertion microscope access without disassembly. A Dino-Lite 220× USB microscope [47] is mounted on a swiveling arm for visual inspection after insertion. For visual inspection during the insertion procedure a Stemi 305 from Zeiss is used [48]. A picture of the setip is shown in Fig. 4.3.

4.2.2 Fiber insertion and alignment procedure

The fiber insertion procedure is illustrated in Figs. 4.4(a) to 4.4(f). Here mostly a fiber without index matching gel applied is used to give better visual insights. First, the optical fiber is secured in the holder and the substrate is clamped in place. The fiber is positioned above the assembly to verify lateral and angular alignment (Fig. 4.4(a)), then retracted and lowered to the height of the ferrule (Fig. 4.4(b)). The fiber is subsequently advanced into the ferrule (Fig. 4.4(c)) until either the printed assembly detaches from the substrate or a substantial increase in insertion force is observed; in the latter case, the fiber is pulled upward to deliberately break the assembly from the substrate. Optionally, a visible alignment laser can be coupled into the fiber to assess alignment and the residual gap to the expansion tube by eye (Fig. 4.4(d)). To minimize bending, the free fiber length in the holder is reduced

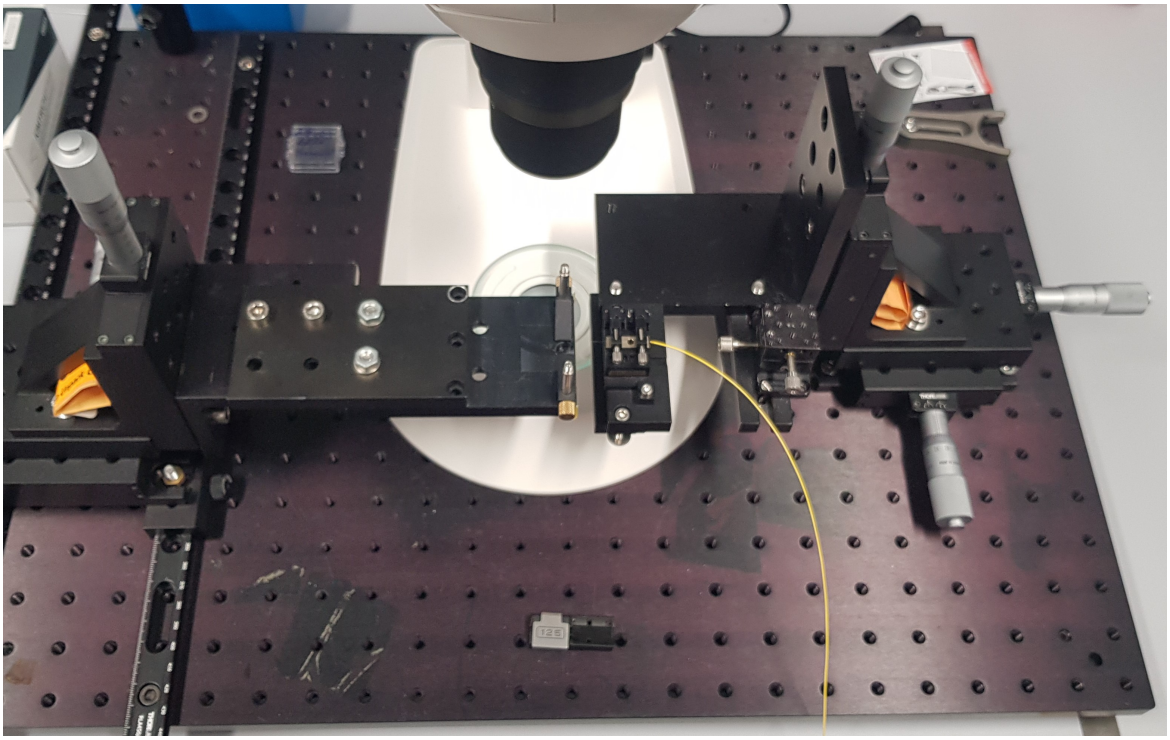

Figure 4.3: Fiber insertion and alignment setup. The fiber is held in an Elliot Scientific fiber holder mounted on a 3-Axis RollerBlock stage. The substrate is clamped on a second RollerBlock stage, which is mounted on a linear rail for additional clearance and microscope access. The Dino-Lite USB microscope is positioned under the left RollerBlock, but is not mounted in the current configuration.

as far as possible before the assembly is gently pressed against an orthogonal stop (Fig. 4.4(e)). To ensure orthogonal alignment between the assembly and the wall, the pressure is periodically released, allowing the assembly to reposition itself against the wall. It is essential to insert only until the fiber tip reaches the expansion tube; further insertion would bend the fiber and introduce an off-axis tilt. Finally, the result is inspected (Fig. 4.4(f)), confirming that the beam inside the expansion tube is well aligned with the optical axis of the assembly and no gap remains between fiber and expansion tube. The final image shows an insertion performed with index-matching gel applied to the fiber. The gel is visibly extruded from the ferrule relief holes, indicating that the fiber has approached the expansion tube and that any further advance must be executed with extreme caution.

4.3 Beam profiler

This section presents the custom-built beam profiler employed for the characterization of fabricated micro-optical elements. Accurate assessment of beam quality is essential, as it serves as a key performance metric for the micro-optical lenses developed in this work. The following subsections detail the measurement principles, system architecture, and control software.

Beam profiling enables quantitative analysis of the transverse intensity distribution and its evolution along the propagation axis. The implemented system measures beam radii and ellipticity at discrete

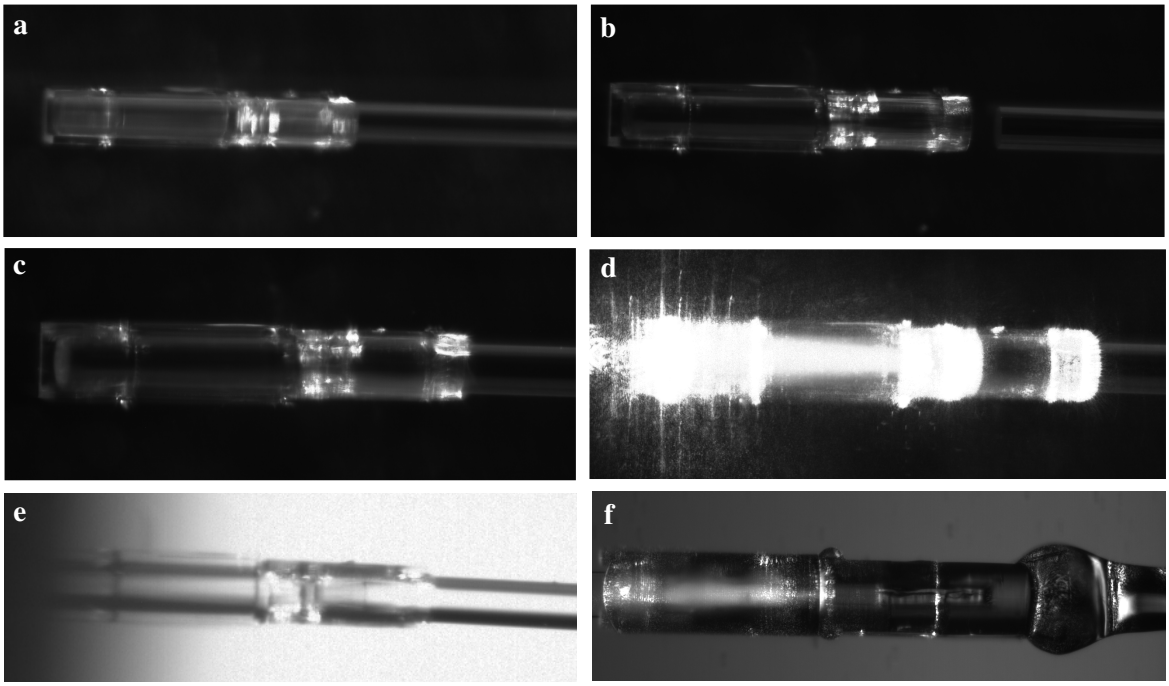

Figure 4.4: Fiber insertion and alignment procedure: (a) align fiber above the assembly; (b) retract and lower to ferrule height; (c) advance into the ferrule; (d) optionally couple a visible laser to check alignment and gap to the expansion tube; (e) minimize free fiber length and seat gently against an orthogonal stop; (f) inspect with a visible laser, confirming beam alignment with the optical axis in the expansion tube. The final image shows an insertion performed with index-matching gel applied to the fiber. The gel is visibly extruded from the ferrule relief holes.

axial positions, allowing for the extraction of Gaussian beam parameters such as waist location, Rayleigh range, and beam quality factor (M^2) through model fitting. These parameters provide a rigorous basis for evaluating the beam-shaping performance of the fabricated micro-optical components.

Our configuration combines a monochrome CMOS camera with microscope imaging and a precision translation stage. The original setup was built by Madhavakkannan Saravanan [49]; the control software used here is derived from code initially ported to Python by Paul Steinmann and has been adapted for this work.

4.3.1 System architecture

A schematic overview of the beam profiler is shown in Fig. 4.5. The positioning stage consists of a three-axis translation system assembled from three Newport MFA-CC stages [50], augmented with a tip–tilt stage for precise alignment of the device under test with the optical axis of the profiler. The microscope is built around a Mitutoyo Plan Apo NIR infinity-corrected objective [51] with a nominal magnification of 20× and numerical aperture NA = 0.40. The objective is paired with the specified tube lens to achieve the desired magnification. Imaging is performed by a Thorlabs DCC1545M monochrome CMOS camera with a physical pixel size of 5.4 µm × 5.4 µm [52].

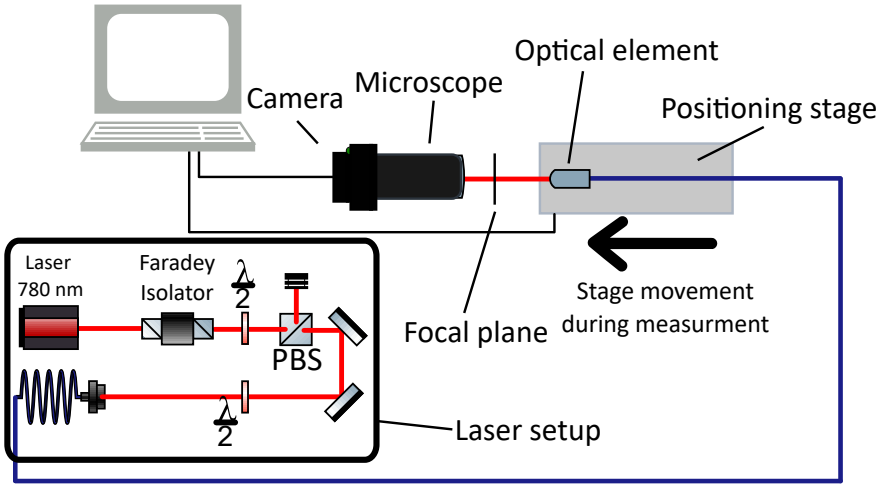

Figure 4.5: Schematic overview of the beam profiler setup. The optical element under test is mounted on a three-axis Newport MFA-CC translation stack (with auxiliary tip–tilt) and is translated through the fixed focal plane of a 20×, NA = 0.40 objective. The objective together with the tube lens form an infinity-corrected microscope projecting the transverse intensity onto a Thorlabs DCC1545M CMOS camera. A control PC is connected to the translation stage and camera to perform alignment and measurement control. This graphic is adapted from McKeever [20].

4.3.2 Working principle

The device under test is positioned on the translation stage and systematically translated through the fixed focal plane of the microscope objective. This arrangement utilizes the microscope's magnification to enhance the effective spatial resolution of the camera. The narrow depth of field provided by the objective ensures that only light originating from the focal plane is sharply imaged, thereby enabling precise measurement of the beam's transverse intensity profile at discrete axial positions. By incrementally advancing the device along the optical axis, the evolution of the beam profile as a function of propagation distance can be accurately characterized.

4.3.3 Control software and interface

The profiler is operated through a custom Python application derived from the implementation by Paul Steinmann and extended for the requirements of this work. The interface provides a graphical user interface (GUI) for: (i) automated beam alignment routines; (ii) motion control and data acquisition; (iii) live visualization of the current beam profile; (iv) data processing as well as; (v) export of structured data. In addition, a second GUI which allows import of acquired data and subsequent analysis is implemented. Screenshots of both GUIs are shown in Fig. 4.6.

4.3.4 Automated beam alignment

To reduce alignment time, an automated alignment routine was implemented. The algorithm places square region of interest (ROI) across several z-planes. The procedure iteratively readjusts the position and shrinks the squares converging to the center of the beam. The readjustment is performed by center-of-mass calculations from the intensity sum in images taken at the edges and center of the

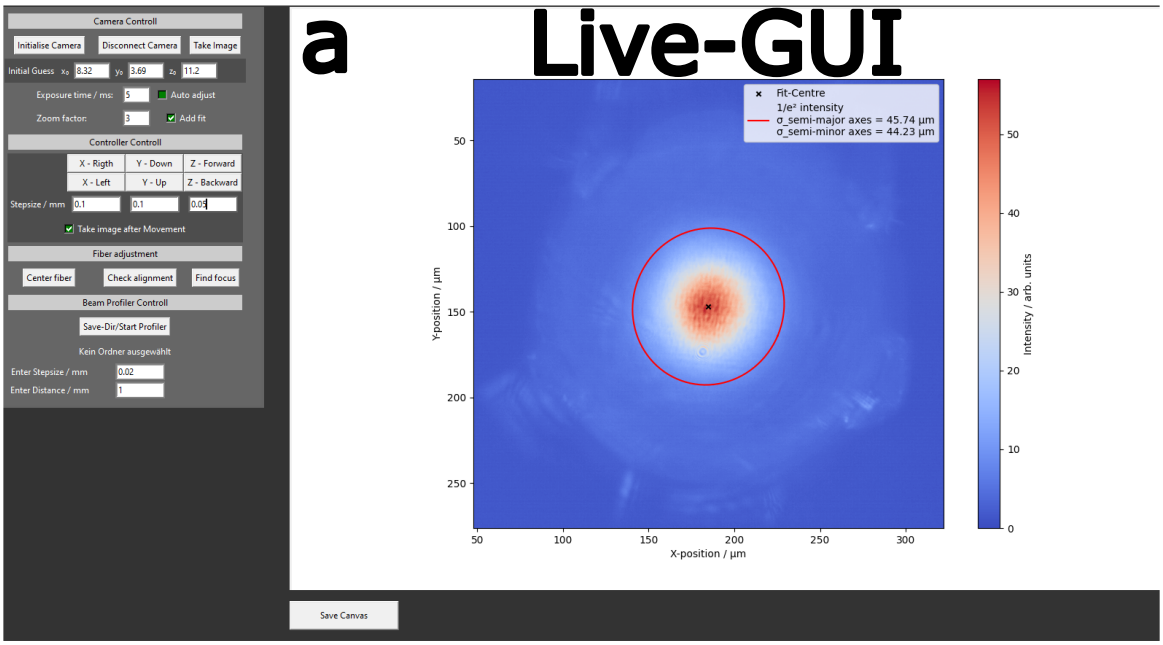

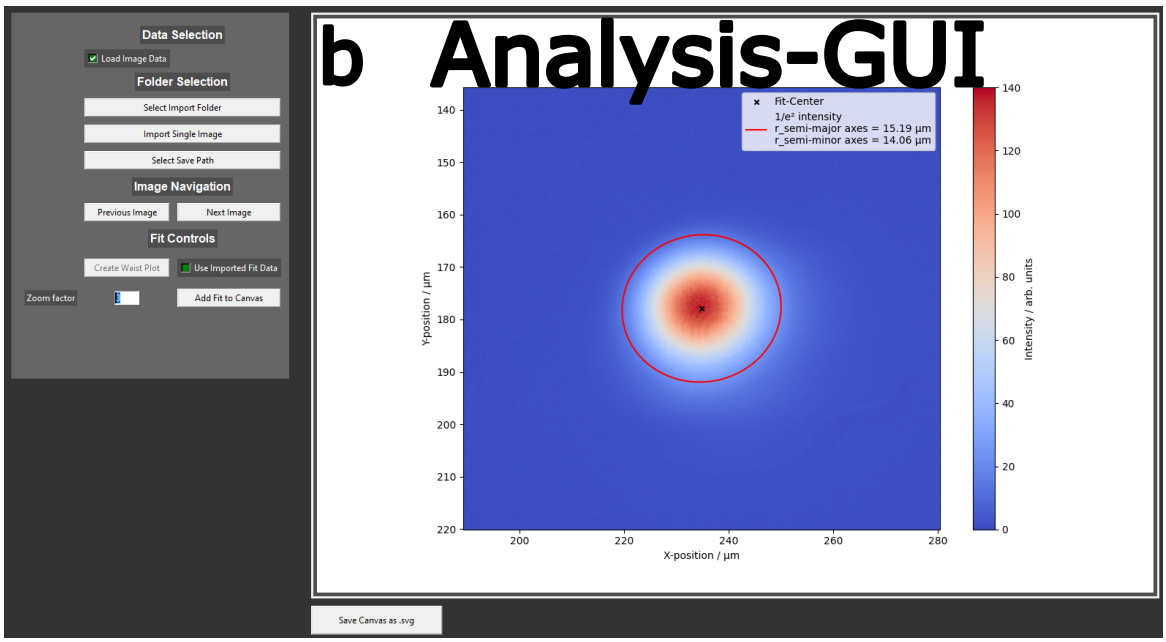

Figure 4.6: Screenshots of the beam profiler live GUI (a) and the analysis GUI (b). The profiler live GUI allows for live visualization and control of the beam profiler, while the analysis GUI enables post-processing and analysis of acquired data.

squares. Finally, a two-dimensional Gaussian fit is performed to determine the beam center in the final z-plane. The stage is then moved to the estimated beam center. The principle of systematically repositioned shrinking squares is illustrated in Fig. 4.7. Subsequently, the beam center is measured over several z-positions; residual angular misalignment is minimized by iteratively adjusting the tip–tilt stage to co-align the profiler optical axis with that of the device under test.

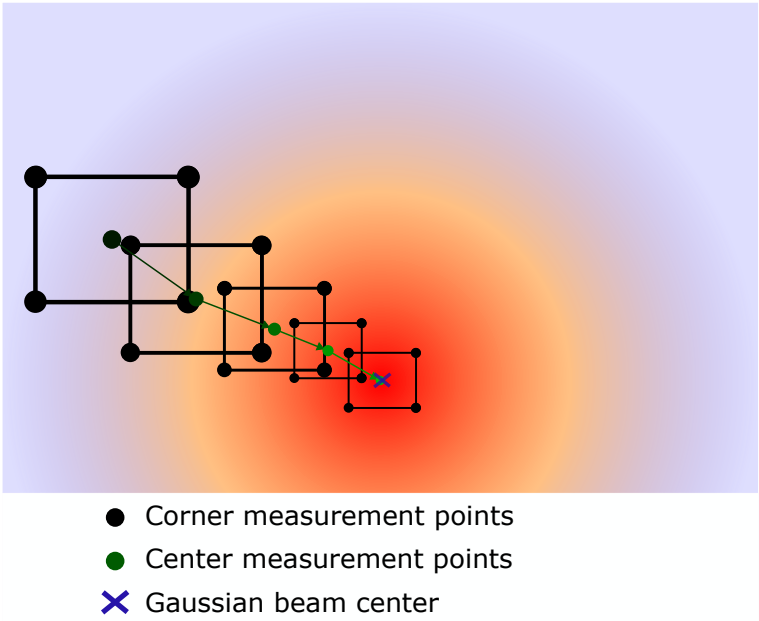

Figure 4.7: Automated beam-centering routine: schematic of repositioned shrinking square ROIs. Edge and center samples are used to compute iterative COM estimates across multiple planes before a final 2D Gaussian fit determines the beam center.

4.3.5 Measurement procedure

Prior to measurement, the beam is co-aligned with the profiler axis using the alignment routine described in Sec. 4.3.4. Start and end axial positions and the step size are then defined in the GUI.

Pixels are converted to metric units using the camera pixel size divided by the microscope magnification. In our setup this yields an effective lateral pixel size of:

$$s = \frac{5.4\,\mu\text{m}}{20} \approx 0.27\,\mu\text{m/px}, \qquad x\,[\mu\text{m}] = s\,x_{\text{px}},\ y\,[\mu\text{m}] = s\,y_{\text{px}}. \tag{4.2}$$

The lateral resolution determined with the Rayleigh criterion is:

$$d = \frac{0.61\,\lambda}{\text{NA}} \approx 1.19\,\mu\text{m}, \tag{4.3}$$

where $\lambda \approx 0.78\,\mu m$ is the wavelength of the laser used. This corresponds to approximately 4.4 pixels, indicating that the systems resolution is not limited by pixel size. At each axial position z, the intensity distribution is modeled by a rotated, elliptic Gaussian. The parametric model used in the analysis is

$$I(x,y) = A\,\exp\left[-2\left(\frac{x'^2}{\sigma_x^2} + \frac{y'^2}{\sigma_y^2}\right)\right] + C, \tag{4.4}$$

with the rotated coordinates

$$\begin{aligned} x' &= (x - x_0)\cos\theta + (y - y_0)\sin\theta, \\ y' &= -(x - x_0)\sin\theta + (y - y_0)\cos\theta, \end{aligned} \tag{4.5}$$

where (x_0, y_0) is the beam center, σ_x and σ_y are the $1/e^2$ radii along the principal axes, θ is the rotation angle, A is the amplitude and C a constant background offset. The $1/e^2$ contour is the ellipse defined by

$$\frac{x'^2}{\sigma_x^2} + \frac{y'^2}{\sigma_y^2} = 1, \tag{4.6}$$

which is used to plot the contour in the GUI.

For the specification of the beam a fixed laboratory coordinate system is used. The rotated radii are projected to obtain horizontal and vertical beam radii in the laboratory frame:

$$w_x = \sqrt{(\sigma_x \cos\theta)^2 + (\sigma_y \sin\theta)^2}, \qquad w_y = \sqrt{(\sigma_x \sin\theta)^2 + (\sigma_y \cos\theta)^2}, \tag{4.7}$$

while the ellipticity is defined as $\varepsilon = \sigma_x/\sigma_y$.

The axial evolution of the beam is characterized by fitting the Gaussian-beam waist model independently to $w_x(z)$ and $w_y(z)$:

$$w(z) = w_0\sqrt{1 + \left(\frac{z - z_0}{z_R}\right)^2}, \qquad z_R = \frac{\pi w_0^2}{\lambda}, \tag{4.8}$$

where w_0 is the waist radius, z_0 the axial location of the waist, z_R the Rayleigh range, and λ the wavelength. The laser used for the analysis has a wavelength of $\lambda \approx 0.78\,\mu m$.
The M^2 value is calculated by fitting:

$$w^2(z) = w_0^2 + M^4\left(\frac{\lambda}{\pi W_0}\right)^2 (z - z_0)^2, \tag{4.9}$$

to the measured beam profile, where $w(z)$ is the $1/e^2$ radius of the beam at axial position z, w_0 is the waist radius at the focus position z_0, λ is the wavelength, and M^2 is the beam quality factor. An exemplary waist plot is shown in Fig. 4.8.

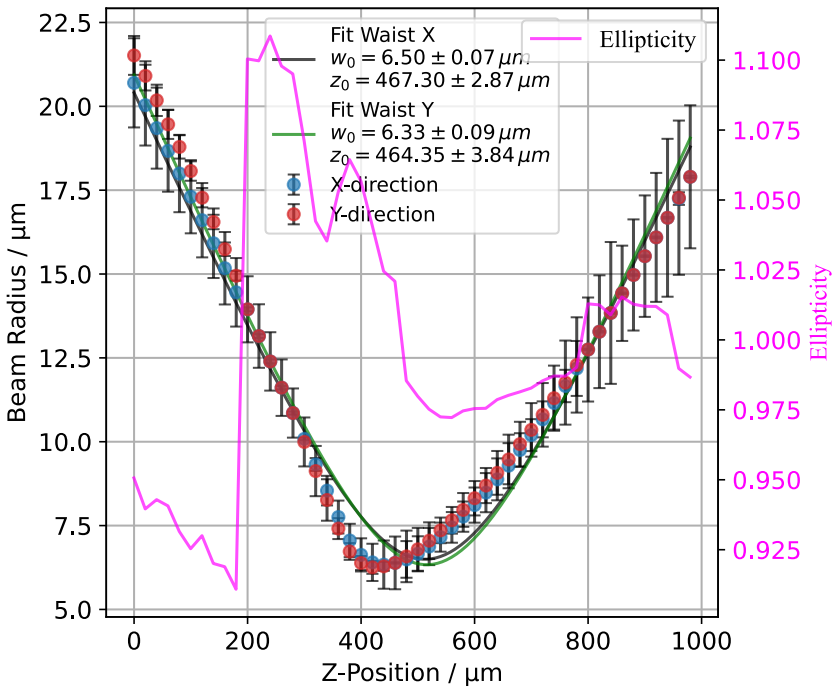

Figure 4.8: Example beam waist measurement in the two fixed laboratory axes x (blue) and y (orange). The $1/e^2$ beam radii $w_x(z)$ and $w_y(z)$ versus axial position z with least-squares fits to the Gaussian waist model of Eq. (4.8) (solid lines) are displayed. In addition, the ellipticity $\varepsilon(z)$ is shown (pink, right axis).

4.4 Scanning White-light interferometer (SWLI)

Scanning white-light interferometers (SWLI) are a key instruments for non-destructive surface metrology. They enable high-resolution surface characterization by recording interference patterns from broadband light reflected from both the sample and a reference mirror, comparable to building a Michelson interferometer configuration between reference mirror and sample. By exploiting the short coherence length of broadband illumination, these systems overcome the 2π-phase ambiguity that constrains single-wavelength interferometers, enabling characterization of surfaces exhibiting both roughness and step-like features over micrometer-scale height ranges. The technique involves recording interference patterns within a defined scanning range of a broadband light source using a camera, subsequently enabling reconstruction of surface height for each pixel.
This chapter provides a comprehensive overview of the SWLI configuration, encompassing underlying theoretical principles and practical implementation. The installed components and calibration procedures employed to ensure measurement accuracy are described in detail.

4.4.1 System architecture

Fig.: 4.9 presents a detailed schematic representation of the complete SWLI setup. The system comprises four principal components: illumination, objective, imaging subsystems, and sample mount,

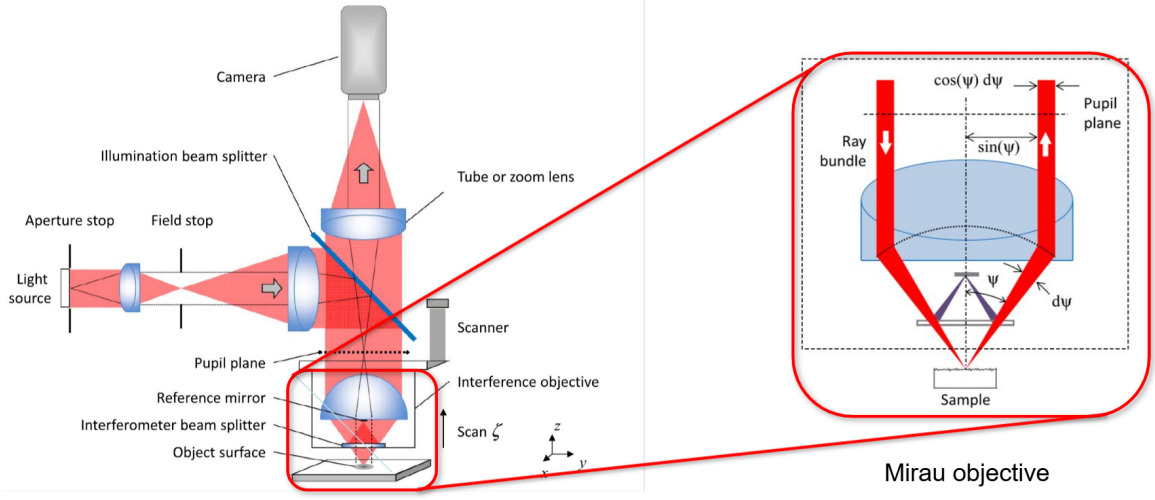

Figure 4.9: Scanning white-light interferometer (SWLI) configuration (left) and Mirau objective detail (right). Left: broadband Köhler illumination, field/aperture stops, tube lens + monochrome camera, Mirau objective mounted on a piezo z-scanner, and sample. Right: internal Mirau layout with beam splitter and reference mirror producing interference between reference and sample reflections after round-trip propagation. This graphic is adapted from Grooter [53].

which are detailed in the following sections.

Illumination Illumination is provided by a broadband light source, specifically a THORLABS QTH10(/M) Quartz Tungsten-Halogen Lamp [54]. To achieve the desired interferogram shape, the spectral profile should ideally exhibit a Gaussian shape [53]. The light source is spectrally filtered using a bandpass filter to transform the thermal emission spectrum into a more Gaussian like profile. A detailed spectral characterization is presented in Sec.: 4.4.5. The goal is to achieve uniform sample illumination which has a wide angular distribution while avoiding imaging of the filament. Illumination in Köhler configuration maximally defocuses individual source points at both the sample and camera planes (represented by black lines in Fig.: 4.9), preventing imaging the light source structure. An additional advantage of the Köhler configuration is the independent control of illuminated spot size and illumination angles through field and aperture stops, respectively. This can be understood by examining the aperture effects on optical paths. The aperture stop constrains the light path from the entire source (indicated by red shading), adjusting the illuminated area on the objective lens and determining the maximum illumination angle on the sample. The field stop limits the collimated beam size from individual point sources, thereby controlling the illumination angle at the objective lens and ultimately determining the spot size at both sample and camera.[53] In our configuration, a diffuser plate is positioned in front of the aperture stop to act as an approximately isotropic secondary light source.

Objective A high numerical aperture (NA) is required to achieve high resolution and to capture reflections at large angles, which are common when measuring curved surfaces. Additionally, a high

magnification is desired. Since interference objectives with external reference mirrors are limited in their working distance, a Mirau objective is employed. Mirau objectives incorporate an internal semi-transparent beam splitter and reference mirror, enabling a compact design while providing high numerical apertures and large magnifications as depicted in Fig. 4.9. [55] Incident light is focused by the objective lens and divided at the semi-transparent mirror: a portion reflects toward the reference mirror while the remainder transmits to the sample. Typically, a larger fraction transmits to compensate for the sample's lower reflectivity relative to the reference mirror. Reflected light from both sample surface and reference mirror recombines at the beamsplitter, creating interference. These objectives are typically infinity-corrected, producing a collimated output beam.
We employ a Mirau objective manufactured by Nikon [56], as illustrated in Fig.: 4.9 (right), engineered for 50× magnification when used with the specified tube lens and featuring an NA of 0.55. Detailed magnification analysis and characterization are provided in Sec.: 4.4.5.
The interferograms for each pixel are taken at different sample positions, which are achieved by moving the objective in the axial direction. This is done using a piezo stage, where the objective is mounted on represented as *Scan* ζ in Fig.: 4.9. Since the accuracy of the piezo stage is crucial for the measurement, a PIFOC High-Precision Objective Scanner[57] is used, enabling precise axial movement. The High-Precision Objective Scanner consists of a piezo for the positioning and a capacitive position readout. Detailed piezo stage characterization is documented in Sec.: 4.4.5.

Imaging The imaging subsystem consists of a THORLABS Kiralux 12.3 MP Monochrome CMOS Camera[58] and a tube lens[59] with a focal length of 200 mm.

Sample mount Sample positioning is achieved using a THORLABS 3-Axis NanoMax Stage[60] combined with a M-GON40-U tip-tilt Goniometric Rotation Stage by Newport[61]. This configuration enables precise positioning and optical axis alignment by hand for the sample.

4.4.2 Creation of interference patterns

The following section describes interference pattern generation in an SWLI microscope. To illustrate the underlying theoretical principles, comprehensive numerical simulations are performed that model the complete interferometric process from light source characteristics to final interferogram formation.

The simulation approach systematically models each component of the interferometric system: First, the broadband light source is represented as a collection of individual spectral components, each characterized by a specific wavelength drawn from a Gaussian spectral distribution. Second, the beam splitting process at the Mirau objective is modeled, where each spectral component is divided between the reference mirror path and the sample path. Third, the interference of reflected beams from both paths is calculated for various optical path differences (Δz). Finally, the integrated intensity across all spectral components is computed to generate the characteristic interferogram that varies with sample position i.e. optical path differences between sample and reference mirror.

This simulation methodology enables systematic investigation of how spectral characteristics and optical path differences influence the resulting interference patterns, providing crucial insights for understanding measurement principles and optimizing reconstruction algorithms.

The simulation is performed with 100000 individual spectral components and 5000 steps in the optical path difference.

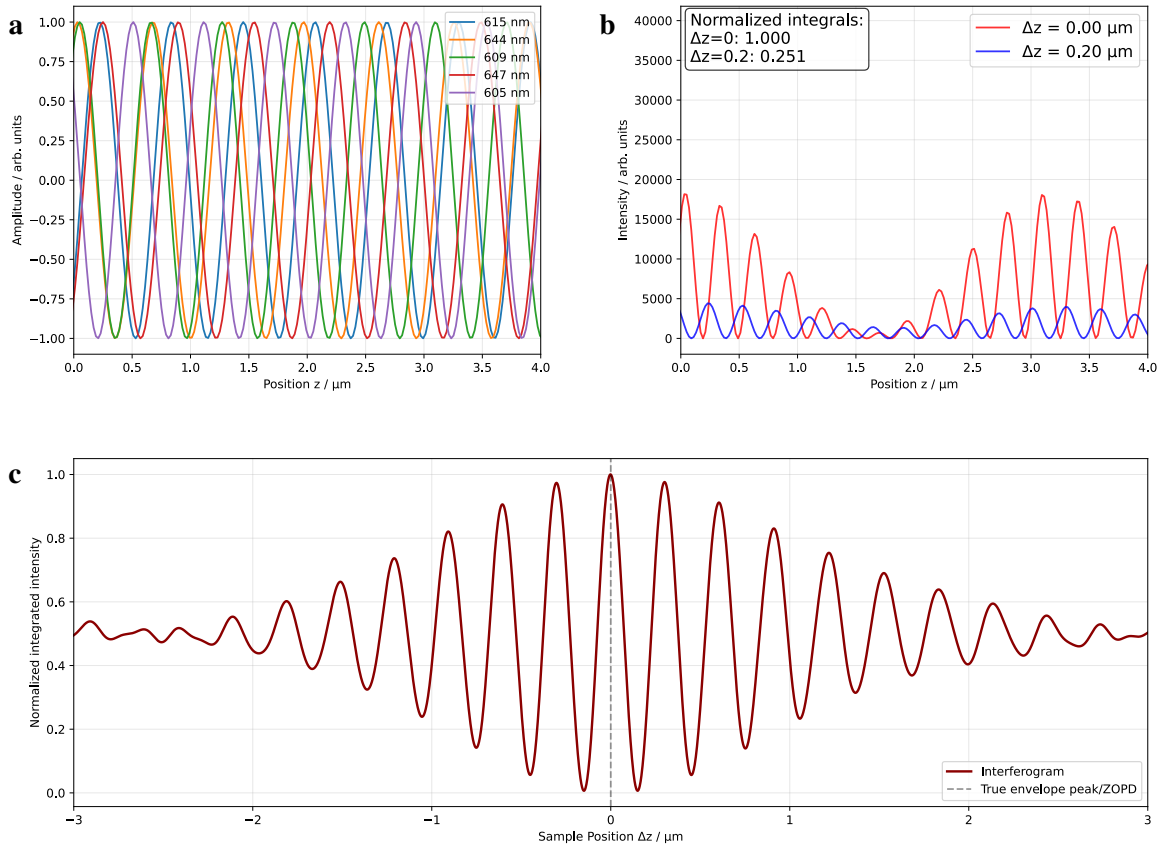

Figure 4.10: Simulation of the individual spectral components (a) of a broadband light source. For better visibility only a selection of individual components are shown. Plot (b) shows the interference after a beamsplitter with and without an optical path difference, together with their respective normalized integrated intensities. The interferogram shown in (c) is created by integrating and normalizing the intensities over time for varying sample positions.

Fig. 4.10(a) displays a selection of individual spectral components randomly sampled from a Gaussian distribution whose sum represents our filtered broadband light source. The parameters of the Gaussian distribution are chosen to match the characteristics of the light source in the build setup. The central wavelength λ_0 is 605 nm and the FWHM spectral bandwidth $\Delta\lambda$ is 175 nm. The waves are calculated for $t = 0$ in front of the beamsplitter as:

$$E(z) = \cos(k_i \cdot z + \phi), \tag{4.10}$$

where $k_i = \frac{2\pi}{\lambda_i}$ is the wavenumber of the i-th spectral component, λ_i is the wavelength of the i-th spectral component, z is the direction of propagation, and ϕ is the phase offset resulting from an incoherent light source. The E-fields are divided at the semi-transparent mirror of the Mirau objective: one portion reflects to the reference mirror while the other transmits to the sample. Reflected light from both sample and reference mirror recombines at the beamsplitter where interference occurs. The resulting intensities behind the beamsplitter both with (blue curve) and without (red curve) optical path difference between sample and reference mirror paths are shown in Fig. 4.10(b). This illustrates

the effect of changing optical path difference, on the interference behind the beamsplitter. Intensity integration over time behind the beamsplitter yields a normalized[1] integrated intensity of unity when no path difference exists, and results in a normalized integrated intensity < 1 for path differences $\neq 0$. The interferogram generated by calculating normalized integrated intensities for varying sample positions is presented in Fig. 4.10(c). The sample position Δz represents the optical path difference between the sample and reference mirror. The zero optical path difference (ZOPD) position ($\Delta z = 0$) i.e., the surface height is marked with a dashed black line. The theoretical function describing these interferograms is given by:

$$I(z) = I_0 + I_m \exp\left(-4\left(\frac{z - z_0}{L_c}\right)^2\right)\cos((z - z_0)K + \Phi_A), [53] \tag{4.11}$$

where

$$K = \frac{2 \cdot 2\pi}{\lambda_0}.$$

Here, I_0 represents the constant intensity component, I_m is the modulation amplitude, z_0 denotes the sample position where the optical path difference between reference mirror and sample equals zero (set to 0 µm in our simulation), Φ_A is a constant phase offset, and the factor of 2 in the definition of K accounts for the round-trip path of the light to the sample and back to the beamsplitter. The wavelength λ_0 is the central wavelength of the illumination, and L_c is the finite coherence length, arising from the broadened light spectrum.[55]. The coherence length can be calculated as $L_c = \frac{\lambda_0^2}{\Delta\lambda}$ [62] resulting in a coherence length of $L_c = 2.09$ µm for the simulated light source. The interferograms in the simulation have a coherence length of 2.32 µm. The measured value for the coherence length in the simulation matches with the theoretically expected value, where the slight deviation can be explained by the discretization in space and spectral components.
In Eq.: 4.11, the phase offset Φ_A is introduced as a constant for a given interferogram. For different interferograms recorded by different camera pixels corresponding to various sample positions, this phase offset may vary. Fig.: 4.11 illustrates how the phase offset induces a shift between the envelope peak and maximum fringe.

The phase offset originates from phase differences between the E-fields returning from sample and reference mirror [53]. The parameter Φ_A is subject to multiple influencing effects, including surface tilt, curvature [63, 64], roughness, measurement noise, aberrations and dispersion introduced by the objective [65], differential phase changes upon reflection, and multiple scattering effects [66, 67]. For some surface reconstruction methods the hereby introduced shift between the envelope peak and maximum fringe peak leads to errors in the reconstructed surface position. Additionally, the signal-to-noise ratio (SNR) and thereby the contrast of the interferograms show a large effect on reconstruction performance. Examples are shown in Appendix A.1. The following section describes three different surface reconstruction methods. The effect of a phase offset and interferogram quality on the reconstruction results is discussed.

[1] We normalize the integrated intensities to the integrated intensities when no path difference is present.

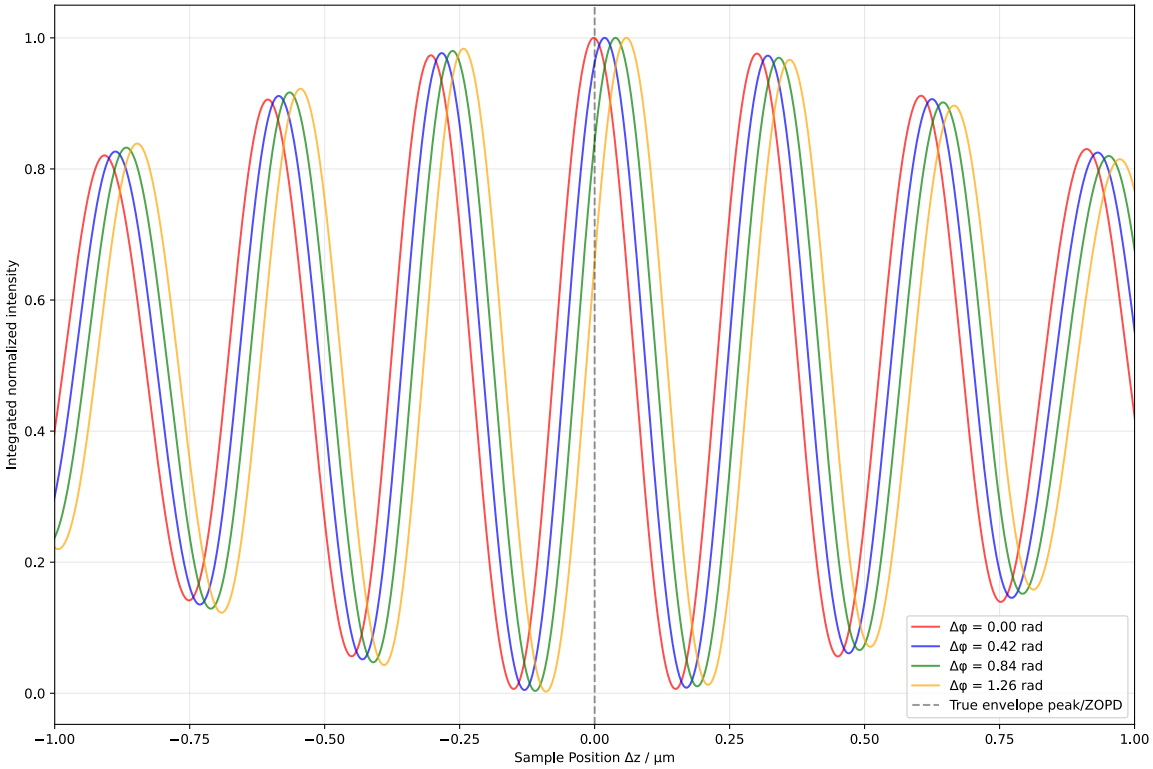

Figure 4.11: Interferograms with varying phase offsets Φ_A.

4.4.3 Surface reconstruction methods

Multiple algorithms have been developed for surface reconstruction from recorded interferogram sets. [55] Algorithm performance depends on experimental conditions and resulting interferogram characteristics. We have implemented three algorithms covering a broad range of conditions. The following sections explain and evaluate these methods using simulated data and comparing their performance on real sample reconstruction.

Direct fit method

The direct fit method represents a straightforward approach to surface profile reconstruction from interferometric data. This technique involves fitting the theoretical model described by Eq.: 4.11 to interferogram data. A critical requirement is that the phase offset Φ_A remains either constant or known throughout the reconstruction area. Small phase deviations result in minor surface position errors, while larger deviations cause failure in assigning the correct cosine fringe corresponding to ZOPD, leading to surface discontinuities in the reconstruction. Our direct fit implementation includes internal quality control mechanisms that assess interferogram SNR, fit root mean square error (RMSE), distance between central fringe peak and envelope peak[2] positions, and verification that fit parameters remain within realistic ranges. Pixels failing any of these criteria are rejected and excluded from

[2] The envelope peak position in determined using the Hilbert transform method explained in Sec. 4.4.3

surface reconstruction minimizing defects in the reconstructed surface profile.
Fig.: 4.12 demonstrates the direct fit method applied to interferograms with various phase offsets,

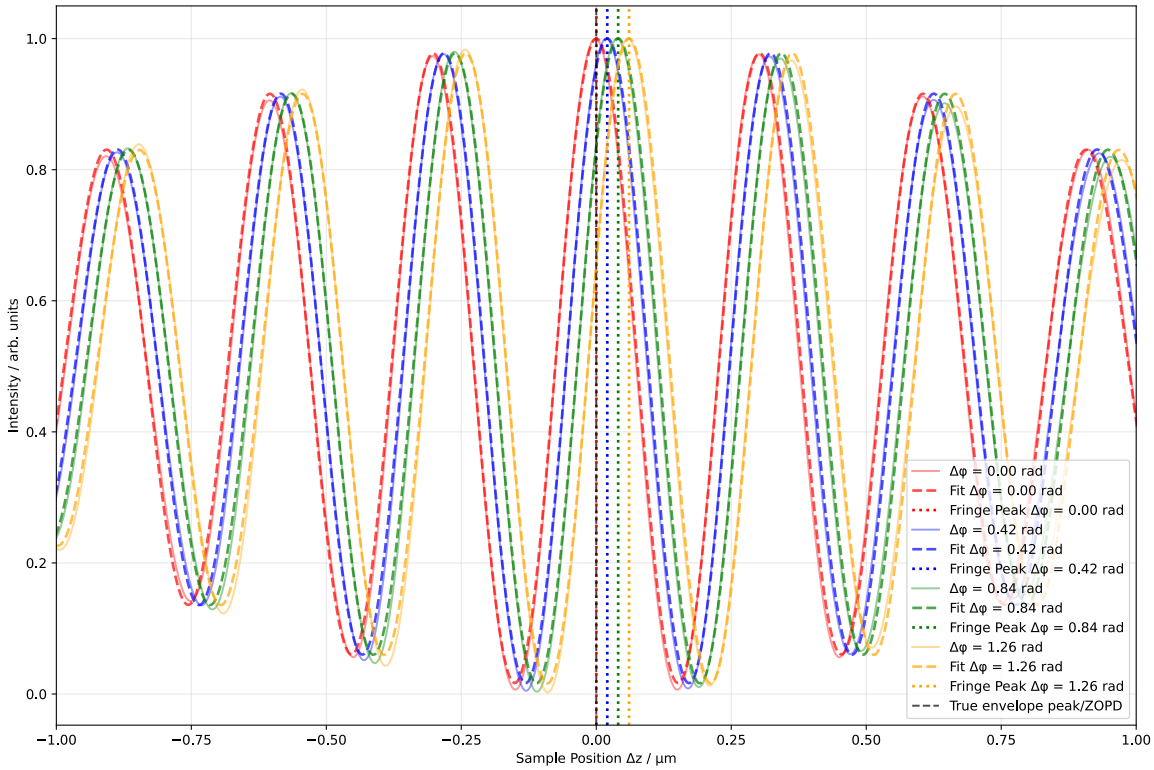

Figure 4.12: Direct fit method applied to interferograms with different phase offsets Φ_A.

where the parameter Φ_A is set to 0 in the fit function according to Eq.: 4.11.
As illustrated in Fig.: 4.12, the method accurately reconstructs surface position for interferograms with $\Phi_A = 0$, yielding negligible error at the true surface position of zero. For interferograms with nonzero phase offset ($\Phi_A \neq 0$), the fit fails to recover the correct surface position, as it tracks the maximum fringe position, which no longer coincides with the ZOPD.
One might attempt to include the phase offset Φ_A as a fit parameter to account for its effect and recover the true ZOPD. While this approach improves data fitting, it results in partial transfer of surface position information into the phase offset parameter, particularly in the presence of noise. Consequently, surface position information is lost and cannot be recovered, leading to greater errors in reconstructed surface position than with a constant phase offset.

Hilbert transform method

An alternative approach for surface profile reconstruction employs the Hilbert transform method. This technique utilizes the Hilbert transform to generate the analytical signal associated with the interferogram. Specifically, for a real-valued signal $x(t)$, the Hilbert transform constructs an orthogonal imaginary component $\tilde{x}(t)$, yielding the complex signal $y(t) = x(t) + i\tilde{x}(t)$. The envelope of the

original interferogram is obtained by calculating the modulus of the complex signal:

$$|y(t)| = \sqrt{x(t)^2 + \tilde{x}(t)^2}. \tag{4.12}$$

This operation effectively eliminates the oscillatory phase component of the interferogram. A Gaussian function is subsequently fitted to the envelope $|y(t)|$ to determine its center, which corresponds to the ZOPD, i.e., the surface position.[68] The Hilbert transform method applied to the interferograms

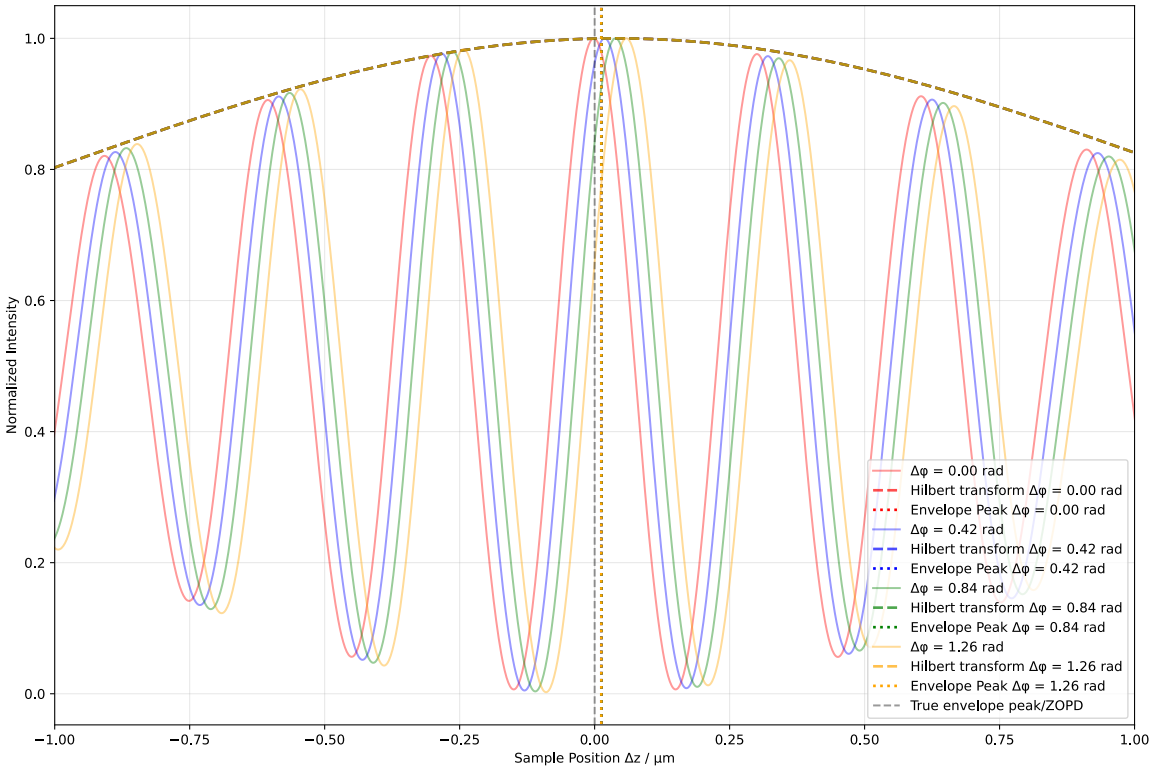

Figure 4.13: Hilbert transform method applied to interferograms with different phase offsets Φ_A.

with various phase offsets is shown in Fig.: 4.13. On the one hand it can be seen that the envelope is extracted correctly for all interferograms, even if the phase offset is not zero. On the other hand, the center of the envelope exhibits a significant error for the interferograms even with a phase offset of $\Phi_A = 0$ compared to the other methods, which is further discussed in Sec. 4.4.3. This represents the effect of a high sensibility to noise which makes this method predominantly reliable on low noise level and high contrast of the fringes in the interferograms. It is noticeable that the envelope peak determined by the Hilbert transform method is shifted by the same amount for all interferograms. The reason for this could not be determined. However, since the focus here is more on qualitative visualization than on quantitative analysis, this is acceptable.

Frequency domain analysis (FDA)

Surface reconstruction based on frequency domain analysis utilizes properties of the Fourier transform of the interferograms. The method exemplified follows the version from De Groot and Deck (1995) [69]. If we assume a constant phase offset of the interferograms in the selected image section, the surface hight difference between pixels can be reconstructed from the phase shift between the interferograms in a global reference frame. This technique is illustrated in Fig. 4.14 for a monochromatic light source i.e. an infinite coherence length. The interferograms for different sample positions with different surface heights are shown. These interferograms get shifted for different heights as expected in a Michelson interferometer. If an arbitrary position is fixed as the reference position (black dotted line) and a pixel is selected as the origin in space, the associated phase shift for each interferogram can be calculated to this reference interferogram at the fixed position. With the information of the central wavelength of the light source λ_0, the surface position can be calculated from the phase shift as:

$$z_{\mathrm{PS}} = \frac{\Delta\varphi\lambda_0}{2 \cdot 2\pi}. \tag{4.13}$$

Here $\Delta\varphi$ is the measured phase shift and the additional factor of 2 originates from the twice covered path difference. This alone suffers from a 2π phase ambiguity, which can be eliminated by unwrapping, but this requires the assumption of continuity in the surface profile, since jumps in the surface of $\frac{\lambda_0}{2\cdot 2}$ for neighboring pixels would be wrongly assigned by the unwrapping process.[53] Therefore we

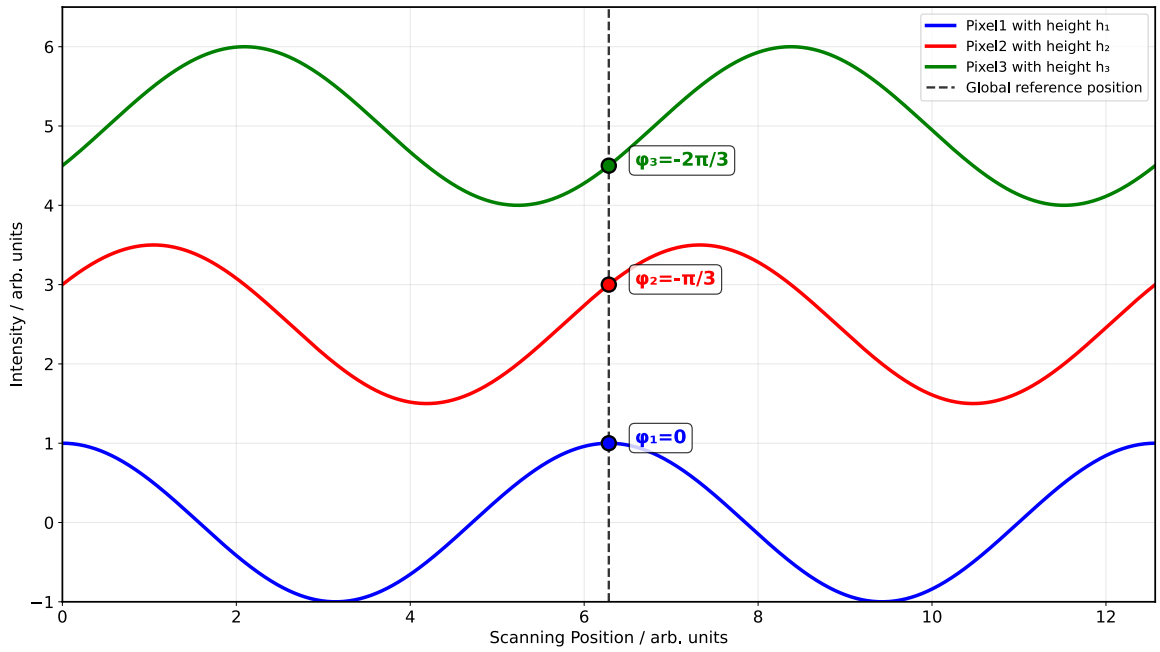

Figure 4.14: Illustration of phase shift analysis for a monochromatic light source.

utilize the space shifting property of the Fourier transform. A translation of a signal in position space corresponds to a slope of the phase in the Fourier domain according to:

$$\mathcal{F}\{f(z - z_0)\} = e^{-i2\pi k z_0}\mathcal{F}\{f\}, \tag{4.14}$$

where $\mathcal{F}$ denotes the Fourier transform, $f(z)$ is the original signal and k is the spatial frequency or wavenumber.[70] This property allows us to track the envelope of our signal in position space by extracting the phase of the frequencies in the Fourier transform. Those can be calculated as:

$$\phi(k) = \arg\left(\mathcal{F}\{f(z)\}(k)\right). \tag{4.15}$$

The phase of the individual Fourier frequencies is unwrapped from the 2π phase ambiguity. Importantly, this unwrapping process preserves all information and simply ensures phase continuity if the number of included frequencies in the Fourier transform is sufficient. A linear function of the form

$$\phi(k) = k \cdot a + b, \tag{4.16}$$

is fitted to extract the slope a and intercept b.[3][69] These parameters are then used to calculate the phase at the central wavenumber k_0:

$$\phi_0 = \phi(k_0) = k_0 \cdot a + b. \tag{4.17}$$

According to Eq.: 4.14, the envelope position recovered with the Fourier transform method z_{FDA} can be determined from the slope a:

$$z_{\mathrm{FDA}} = \frac{-a}{2\pi}. \tag{4.18}$$

The key step is now to resolve the phase ambiguity of the central wavenumber k_0 not only by unwrapping as it would be done for monochromatic phase shift methods as discussed above but the following correction is applied:

$$z'_{\mathrm{FDA}} = \frac{1}{2}\left[\frac{\phi_0 - \Phi_A}{k_0} - \frac{2\pi}{k_0}\mathrm{round}\left\{\frac{(\phi_0 - \Phi_A) - (2k_0 z_{\mathrm{FDA}})}{2\pi}\right\}\right] \tag{4.19}$$

where round denotes rounding to the nearest integer. Thus, the surface position determined by the phase shift is adjusted by integer multiples of $\frac{\lambda_0}{2}$ to minimize deviation from the envelope peak position.
Fig.: 4.15 illustrates the application of the FDA method to an interferogram with a phase offset of $\Phi_A = 0$ in detail. The interferogram and the reconstructed surface position using the FDA method is shown in (Fig. 4.15(a)). In (Fig. 4.15(b)) the Fourier transform, with the frequencies used for analysis indicated in red are displayed. Although frequency amplitudes are used as weights for the linear fit, it is advantageous to set a lower threshold for inclusion, as frequencies with low amplitude primarily contribute as noise. The Gaussian profile of the light source is clearly reconstructed in the Fourier domain. The bottom plot (Fig. 4.15(c)) presents the unwrapped phase of the Fourier frequencies with a linear fit according to Eq.: 4.16. The FDA method is also applied to the interferograms with different phase offsets shown in Fig.: 4.16. It can be seen that the FDA method is able to track the peak of the central fringe precisely, but of course also lacks the capability to account for a phase offset.

Comparison of the ZOPD position reconstruction performance A summary of the three surface reconstruction methods is presented in Fig. 4.17. The surface reconstruction with the Hilbert method is not influenced by the phase offset, whereas the deviations from the true surface position for

[3] Higher-order terms may be included to account for second-order dispersion in the interferogram.

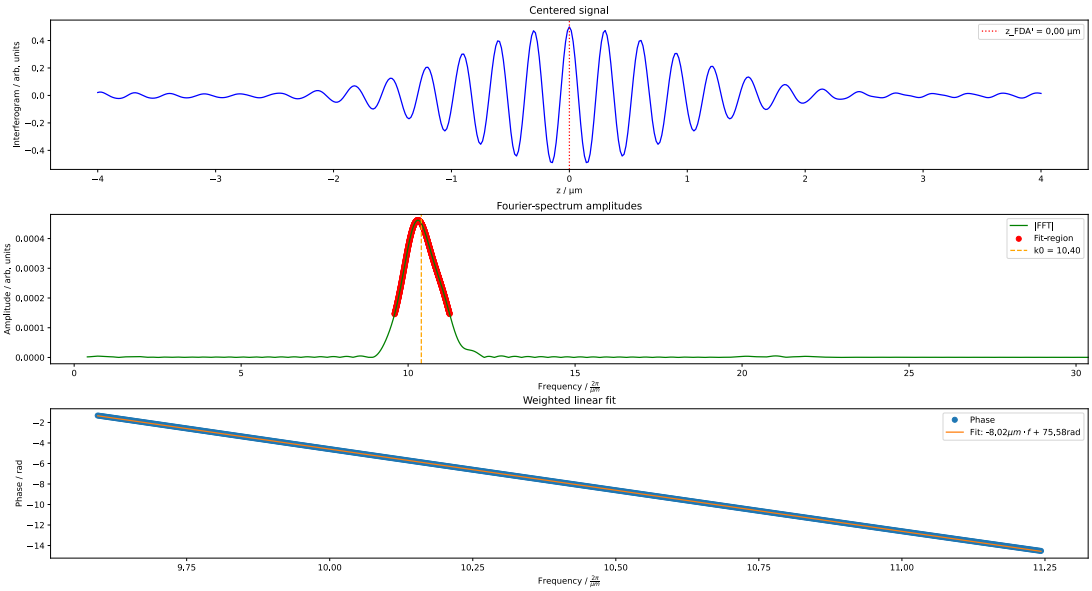

Figure 4.15: Steps of the Frequency Domain Analysis (FDA) method for an interferogram with a phase offset of $\Phi_A = 0$. (a) Interferogram with the reconstructed surface position with the FDA method. (b) Fourier transform of the interferogram with the frequencies used for the analysis indicated. (c) Phase of the Fourier frequencies with a linear fit (Eq.: 4.16).

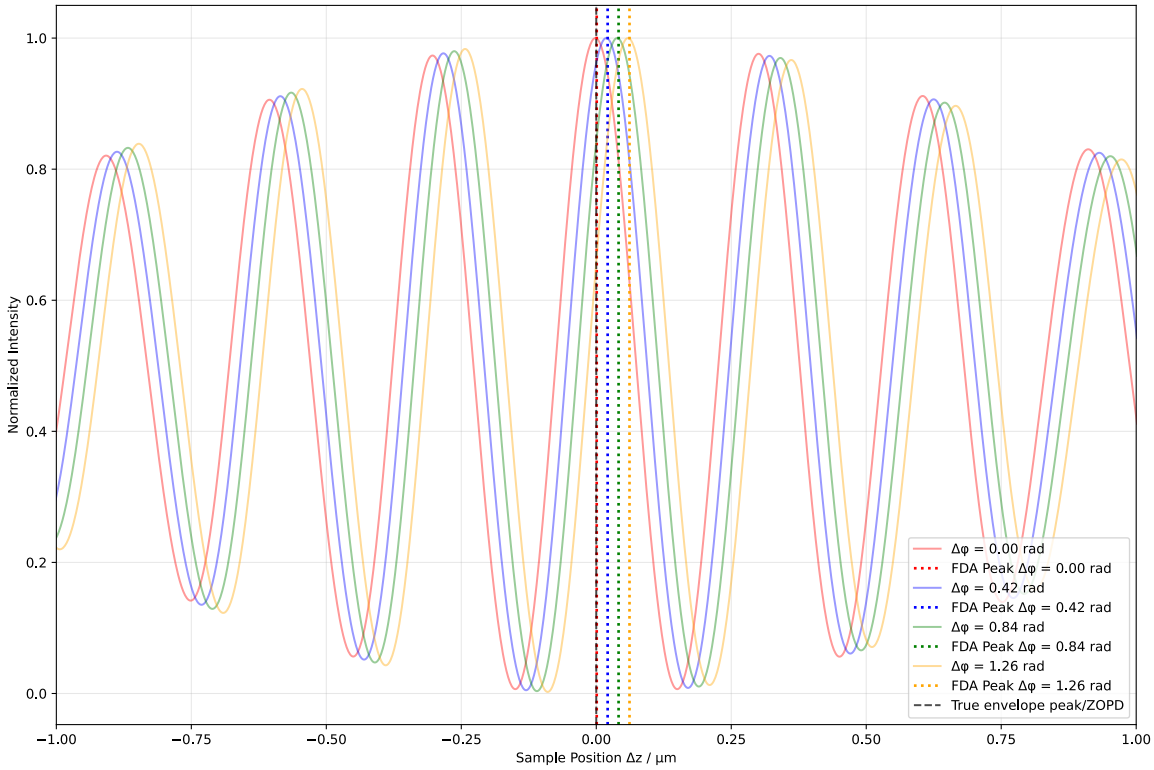

Figure 4.16: Frequency Domain Analysis applied to interferograms with different phase offsets Φ_A.

the direct fit and the FDA method increase with increasing phase offset.

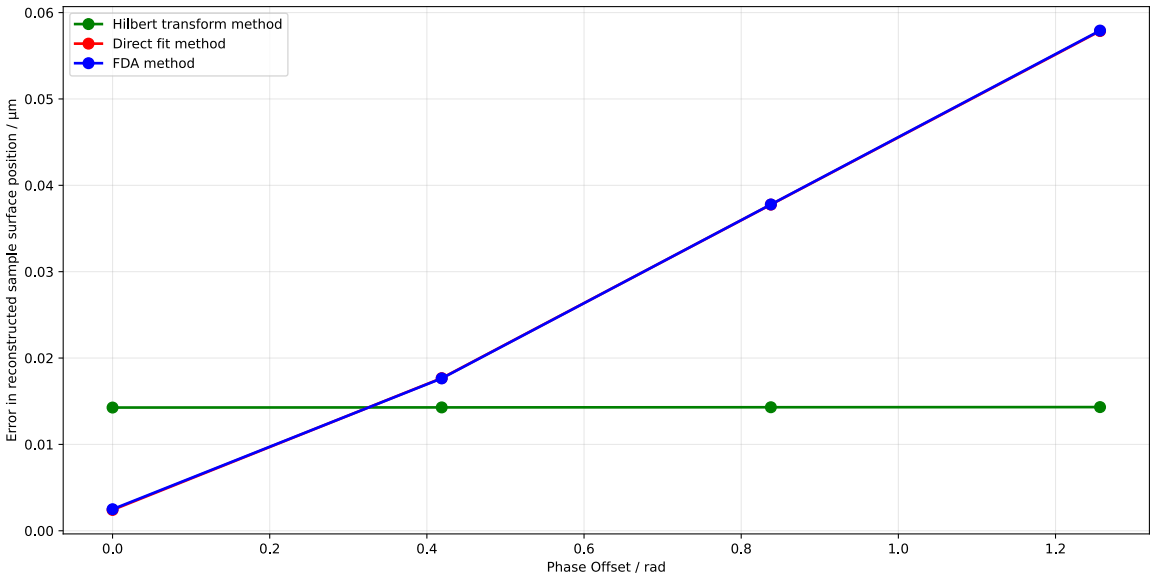

Figure 4.17: Comparison of different surface reconstruction methods with respect to the phase offset Φ_A.

4.4.4 Comparison of computational efficiency for the reconstruction methods

Since the measured samples typically need to be measured on large image fields with pixel counts exceeding 200×200, and multiple surfaces need to be reconstructed, the efficiency of the methods are of special interest. All methods are implemented in Python and are thereby limited to single core processing without any further optimization. An expansion has been implemented allowing processing of either surfaces or methods in parallel mode, speeding up the reconstruction process in case of multiple surfaces or methods. For comparison of the methods surface reconstructions were performed on a 150×150 pixel image of printed lenses. For the single core processing, we reconstructed 5 surfaces with each method, while for the parallel processing we reconstructed 12 surfaces with each method. The average reconstructed pixels for the three methods are printed in Tab.: 4.1. The measurements were performed on a computer with an AMD Ryzen 5 3600 CPU[4] overclocked to 4.2 GHz and 32 GB RAM. The three methods show a significant difference in reconstruction

Method	Single core / pixels$\cdot s^{-1}$	Parallel / pixels$\cdot s^{-1}$
Direct Fit Method	146.0 ± 4.4	1071.4
Hilbert Transform Method	624.3 ± 13.4	3461.5
FDA method	340.9 ± 3.8	2045.5

Table 4.1: Comparison of reconstruction speeds for the three methods in single core and multiprocessing configuration.

speed. The direct fit method is the slowest, as it requires fitting a function to each interferogram as

[4] The processor occupies 6 physical cores and 6 virtual cores allowing a maximum of 12 processes in parallel.

well as checking all rejection criteria, which is computationally expensive. The Hilbert transform method is significantly faster and the FDA method is slightly slower than the Hilbert transform method, however, it is still faster than the direct fit method by a factor of approximately 2, since fast Fourier transforms are computationally very efficient. This also explains why this rather elaborate method was implemented, even though, as described above, it does not offer a significant advantage in the accuracy of the surface reconstruction compared to the direct fit method. The comparison between single core and parallel processing shows a substantial speedup for all methods within a range of 5 to 7×.

4.4.5 Characterization of the SWLI setup

In this section, we will review the characterization of the SWLI setup to ensure accurate measurement and reliable results from the microscope. In the following, we will firstly characterize its components, which are crucial for the performance of the SWLI. Secondly, we will review sample measurements to evaluate the performance of the SWLI setup.

Magnification and effective pixel size

The magnification of the system is determined by the focal length of the objective and tube lens as:

$$M = \frac{f_{\text{tube}}}{f_{\text{obj}}} \tag{4.20}$$

where f_{tube} is the focal length of the tube lens and f_{obj} is the focal length of the objective lens. The Mirau objective used here has a 4 mm focal length and is used in combination with a 200 mm tube lens, resulting in a theoretical magnification of 50. The magnification has been tested using the known dimensions of the lines on the 2" x 2" Positive, USAF 1951 Hi-Resolution Target[71] over the central region of the camera chip as depicted in Fig.: 4.18. Therefore we will measure the size of single lines and the square on the test target in pixels and compare it to their specified size.

The magnification for individual objects can be calculated as:

$$M = \frac{S_{\text{chip}}}{S_{\text{object}}} = \frac{N_{\text{pixels}} \cdot b \cdot p_{\text{cam}}}{\frac{N_{\text{LP}}}{\text{LP}_{\text{density}}} \cdot 1000} \tag{4.21}$$

where S_{chip} is the size of the object on the camera chip, S_{object} is the size of the object on the test target, N_{pixels} is the number of pixels determined by the sigmoid fit in Fig.: 4.18, b is the binning factor of the camera which is set to 3, p_{chip} is the pixel size of the camera chip which is 3.45 µm[58], N_{LP} is the number of lines per group on the test target and $\text{LP}_{\text{density}}$ is the line pair density of the test target in mm^{-1}. The edge positions recovered from the sigmoid fits fot the intensity profile are summarized in Tab.: 4.2, in which the lines are numbered from left to right in the image. The magnification results are shown in Tab.: 4.3. The average magnification of the system is $\bar{M} = 49.93 \pm 0.09$, which is in good agreement with the theoretical magnification of 50. The resulting effective pixel size is $p_{\text{eff}} = \frac{p_{\text{chip}}}{M} = 0.207\,\mu\text{m}$.

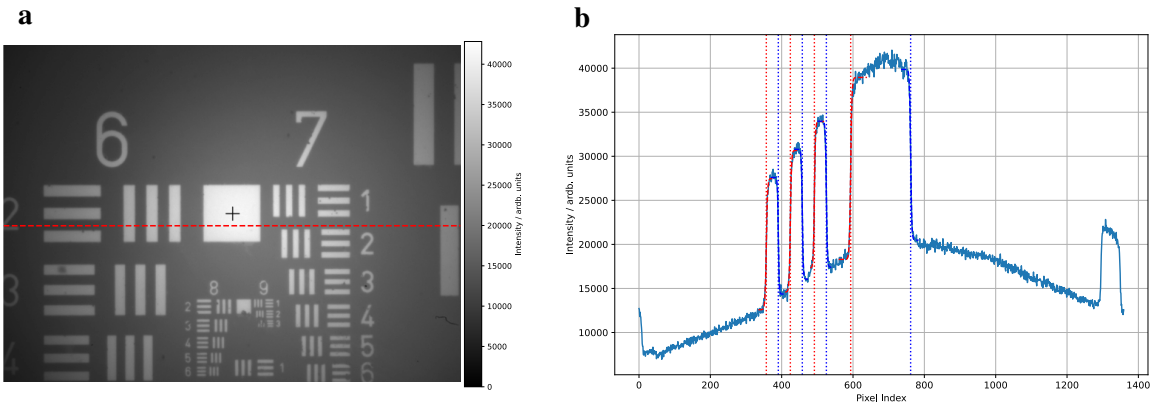

Figure 4.18: Magnification test results using USAF 1951 Hi-Resolution Target at different positions on the camera chip. (a) 1365 × 1000 pixel image of the USAF 1951 Hi-Resolution Target, where the dashed red line marks the pixels used for the magnification evaluation in (b). (b) 1D intensity profile over 1365 pixels across the red line in the USAF 1951 Hi-Resolution Target shown in (a). Sigmoid fits are applied to determine the right and left edge positions of the test target lines and the square.

Feature	x-value
Square left edge	593.4
Square right edge	761.5
Line 1 left edge	356.9
Line 1 right edge	390.6
Line 2 left edge	424.3
Line 2 right edge	457.8
Line 3 left edge	491.7
Line 3 right edge	525.3

Table 4.2: Edge positions from intensity profile in Fig.: 4.18.

White light source spectrum

The spectrum of the white light source has been measured using a Red Tide USB650 Fiber Optic Spectrometer from Ocean Optics [72] and is shown in Fig.: 4.19. The spectrometer has an optical resolution of 2 nm FWHM and a detection range of 200 to 1 100 nm. The spectrum shows that the thermal light source has been successfully shaped to a Gaussian profile using a bandpass filter. The central wavelength has been extracted both from a Gaussian fit and from the centroid method following:

$$\lambda_c = \frac{\sum_i \lambda_i \cdot I_i}{\sum_i I_i}, \text{[73]}, \tag{4.22}$$

where I_i is the intensity of the i-th spectral component. Since the FDA reconstruction algorithm uses the centroid method to extract the central wavelength[5], it is important to verify the accordance of

[5] Although the Gaussian fit provides a more accurate estimation of the central wavelength, this method is computationally more intensive and would therefore noticeably increase the algorithm runtime.

Object	M	ΔM
Square region	49.97	0.05
Left line	49.96	0.22
Center line 2	49.84	0.22
Right line	49.95	0.20

Table 4.3: Magnification results for the USAF test target shown in Fig.: 4.18.

both methods. From the extracted FWHM of the Gaussian fit $\Delta\lambda$, the coherence length L_c can be calculated as:

$$L_{\text{coh}} = \frac{\lambda_0^2}{\Delta\lambda}[62]. \tag{4.23}$$

The spectral characteristics results for the filtered thermal light source are shown in Tab.: 4.4. The

Parameter	Value	Uncertainty
Spectral Centroid	605 nm	4.57 nm
Center Wavelength (μ)	605.1 nm	0.29 nm
FWHM ($\Delta\lambda$)	174.8 nm	0.84 nm
Coherence Length (L_c)	2.1 µm	0.0 µm

Table 4.4: Spectral characteristics of the filtered thermal light source.

coherence length in the interferograms have been measured for 3 surface reconstructions of glass substrates with a image field of 300×300 pixels. The average coherence length is $L_c = (2.20\pm0.02)$ µm, which is in good agreement with the coherence length calculated from the spectrum. The slight deviation may be attributed to the fact that the spectrum is not a perfect Gaussian, as assumed in the calculation of the coherence length in Eq. 4.23.

Piezo mounting stage movement

The accuracy of the piezo stage used to move the Mirau objective is crucial for the performance of the SWLI. Any error in the positioning of the objective is directly transferred to the surface height reconstruction. The stage consists of two primary parts, the piezo actuator itself and a built-in capacitive measurement gauge which is used for the position readout. The included software from Ocean Optics allows scanning a defined distance in defined steps while measuring the actual position of the stage for each step. The stated accuracy for the position readout is ±5 nm [57]. The measurement results are shown in Fig.: 4.20. The piezo stage exhibits the expected linear behavior with a slope of 1.000009 ± 0.000025. The linearity error in the limited scan region can be calculated as:

$$\text{Linearity Error} = \frac{\max_i |r_i|}{\text{Position Range}} \times 100\%, \tag{4.24}$$

where $\max_i$ is the maximum over i and $|r_i|$ is the deviation from the linear fit in the i-th step. The linearity error for the piezo stage is $0.171 \pm 0.034\%$. Since we use a very limited range of the piezo

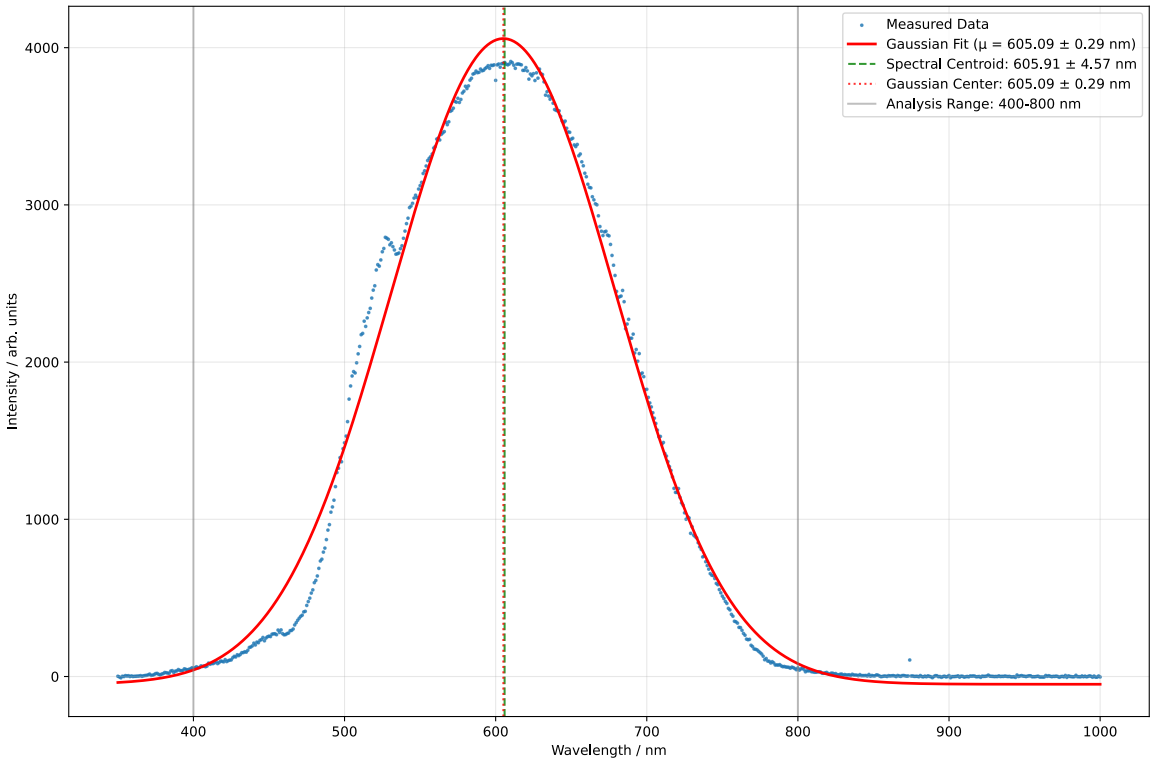

Figure 4.19: Spectrum of the thermal light source filtered by a bandpass filter (blue points) together with a Gaussian fit (red line). Also marked are the central wavelength extracted from the Gaussian fit as well as the calculated central wavelength using the centroid method.

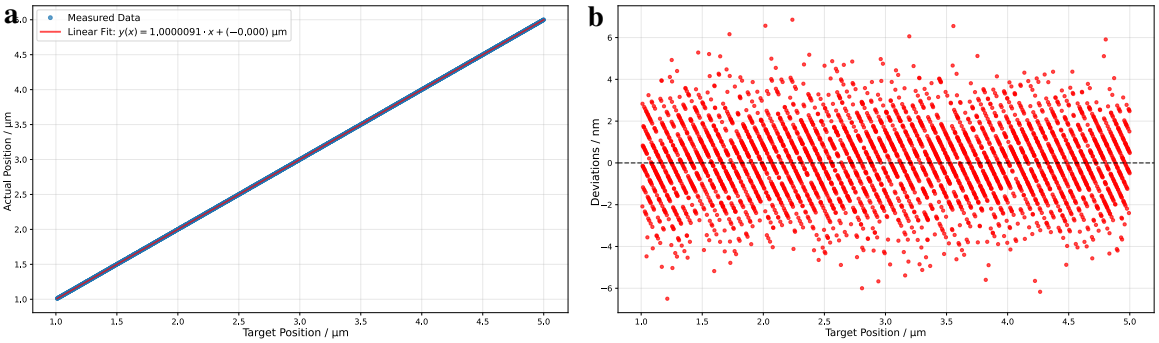

Figure 4.20: Piezo stage characterization. (a) Position readouts of the piezo stage (blue points) for a position scan over 4 µm in 10 nm steps with a linear fit (red line). (b) Deviations between the measured position and the target position.

stage for the characterization[6], the travel range should be artificially extended to the full range of 100 µm to be comparable to the specified linearity error of 0.03% [57]. The adapted linearity error for the extended range is 0.007 ± 0.001%, which is well below the specified error. The deviation distribution is also in good agreement with the repeatability of the position stage specified as ±5 nm [57].
Since this position readout is the only validation source for the piezo position, we rely on its accuracy. The accuracy of the capacitive measurement gauge is not characterized here but should be checked in the future. A possible method could be setting up an laser interferometer which provides a well-defined external length standard.

Influence of step sizes

When measuring a surface, a crucial parameter is the step size of the piezo stage. Too small steps lead to longer measurement times during which external influences such as temperature fluctuations or air turbulence can affect the measurement. Too large steps lead to limited statistics and increase the influence of noise on the acquired interferograms. Therefore, 3 measurements for each of the selected step sizes of 2, 5 and 15 nm respectively are performed on the same stripped optical fiber. As a performance measure, the radius of curvature of the fitted cylinder is used, where the true value for the radius of curvature is 62.5 µm. The results are shown in Tab. 4.5 and Fig.: 4.21 and suggest that the step size of 15 nm is the best choice for the current setup since the measured radius of curvature is most accurate across all reconstruction methods.

Table 4.5: Radius of curvature measurements for different reconstruction methods and step sizes

Method/Step size	2 nm	5 nm	15 nm
Direct method	64.7 ± 3.6	67.2 ± 3.5	63.1 ± 2.1
FDA method	64.2 ± 2.9	69.8 ± 1.2	63.8 ± 1.6
Hilbert transform method	48.9 ± 8.9	60.6 ± 4.0	61.4 ± 1.3
True value		62.5	

Reconstruction of sample surfaces

To evaluate the performance of the three reconstruction methods on data taken on real-world surfaces, we analyze two test samples: a glass substrate and a stripped optical fiber. These samples offer complementary validation scenarios—the glass substrate serves as a reference flat surface to assess systematic errors and aberrations, while the optical fiber provides a well-defined cylindrical geometry for evaluating reconstruction accuracy of curved surfaces. As specifically the performance on curved surfaces is of special interest since it is expected that interferograms from curved surfaces suffer from bad contrast as some portion of the reflection is lost. To give an idea of such effects on the recorded interferograms we show exemplary interferograms in Figure A.1.

[6] The piezo stage comes with a travel range of 100 µm from which only 30 µm are usable at this point. The limited travel range is sufficient for our application, but a complete measurement of the linearity error over the whole travel range is no longer possible for this reason.

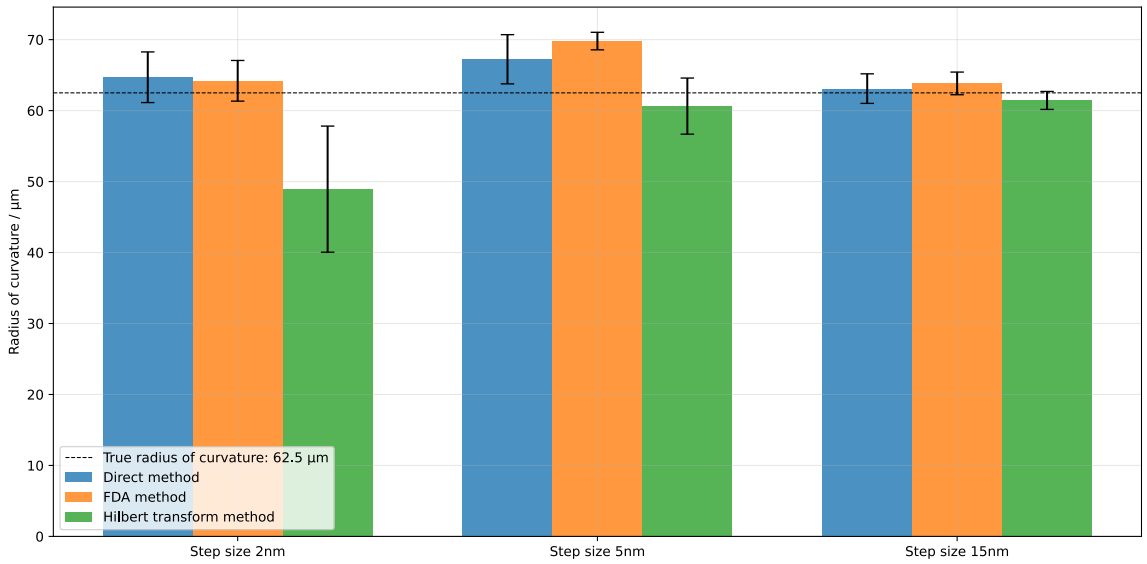

Figure 4.21: Comparison of reconstruction performance with different step sizes. The sample surface is a stripped optical fiber with a radius of curvature of 62.5 µm. The radius of curvature of the fitted cylinder is shown for each step size with each reconstruction method.

When the true surface profile is known, an outlier correction procedure can be applied by fitting the expected surface shape to the initially reconstructed profile and identifying deviations exceeding a predefined threshold. These outliers are replaced with corresponding values from the fitted surface, followed by surface re-fitting to obtain a refined reconstruction. This post-processing step effectively suppresses artifacts, particularly for the Hilbert transform method, which is otherwise highly susceptible to noise-induced outliers.
The real data measurements serve dual purposes: evaluating algorithm performance and identifying the influence of various error sources on the experimental setup.

Glass substrate The glass substrate[7] presents a flat surface across an extended field of view, making it ideal for detecting systematic errors related to the distance from the optical axis. Optical aberrations, considered as potential error sources, are specifically evaluated using this test sample.
The following sections present comparative results from all three reconstruction methods, with each method evaluated using identical metrics: 3D surface reconstruction with plane fitting, surface deviation analysis, cross-sectional profiles, and interferogram phase offset estimations.

Direct fit method In Fig. 4.22, the direct fit method demonstrates excellent performance on the glass substrate. The 3D surface reconstruction (Fig. 4.22(a)) shows minimal reconstruction error, with only minor spikes reaching approximately 50 nm in height, likely caused by dust particles. The surface deviation from the plane fit (Fig. 4.22(b)) and cross-sectional analysis (Fig. 4.22(c)) confirm excellent agreement to the expected flat geometry. The deviation between fitted central fringe peak

[7] The surface of the substrate has on purpose not been cleaned before the individual calibration measurements.

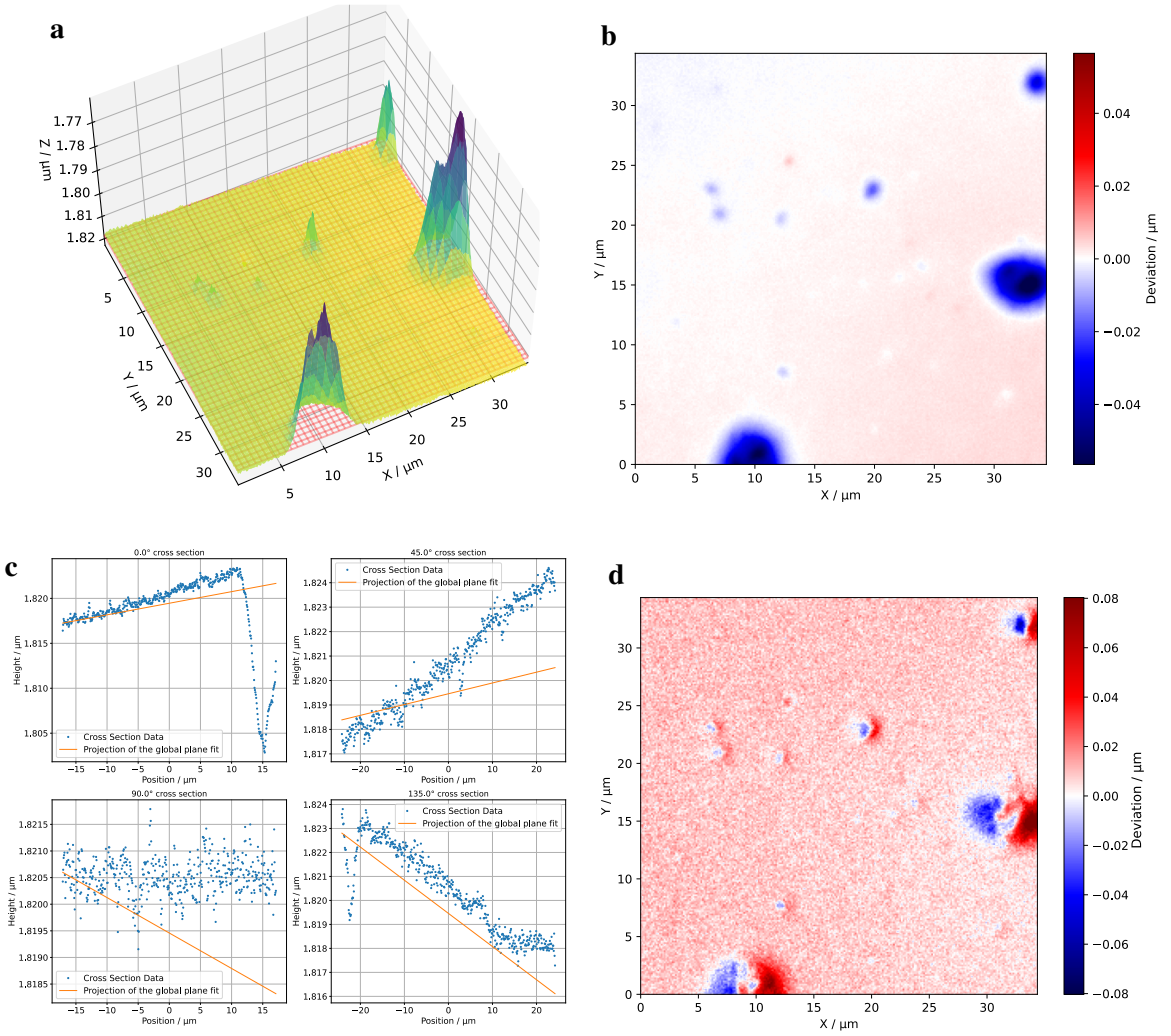

Figure 4.22: Surface reconstruction of a glass substrate using the direct fit method. (a) 3D surface reconstruction with a plane fit to the surface (red mesh). (b) Surface deviation to the plane fit. (c) Cross sections through the surface reconstruction (blue points) and a projection of the global plane fit (orange line). (d) Deviation between the fitted central fringe peak position and the envelope peak position determined by the Hilbert transform method.

positions and envelope peak positions determined by the Hilbert transform method (Fig. 4.22(d)) remains nearly constant across the image field, indicating consistent phase offset, with increases only at spike locations.

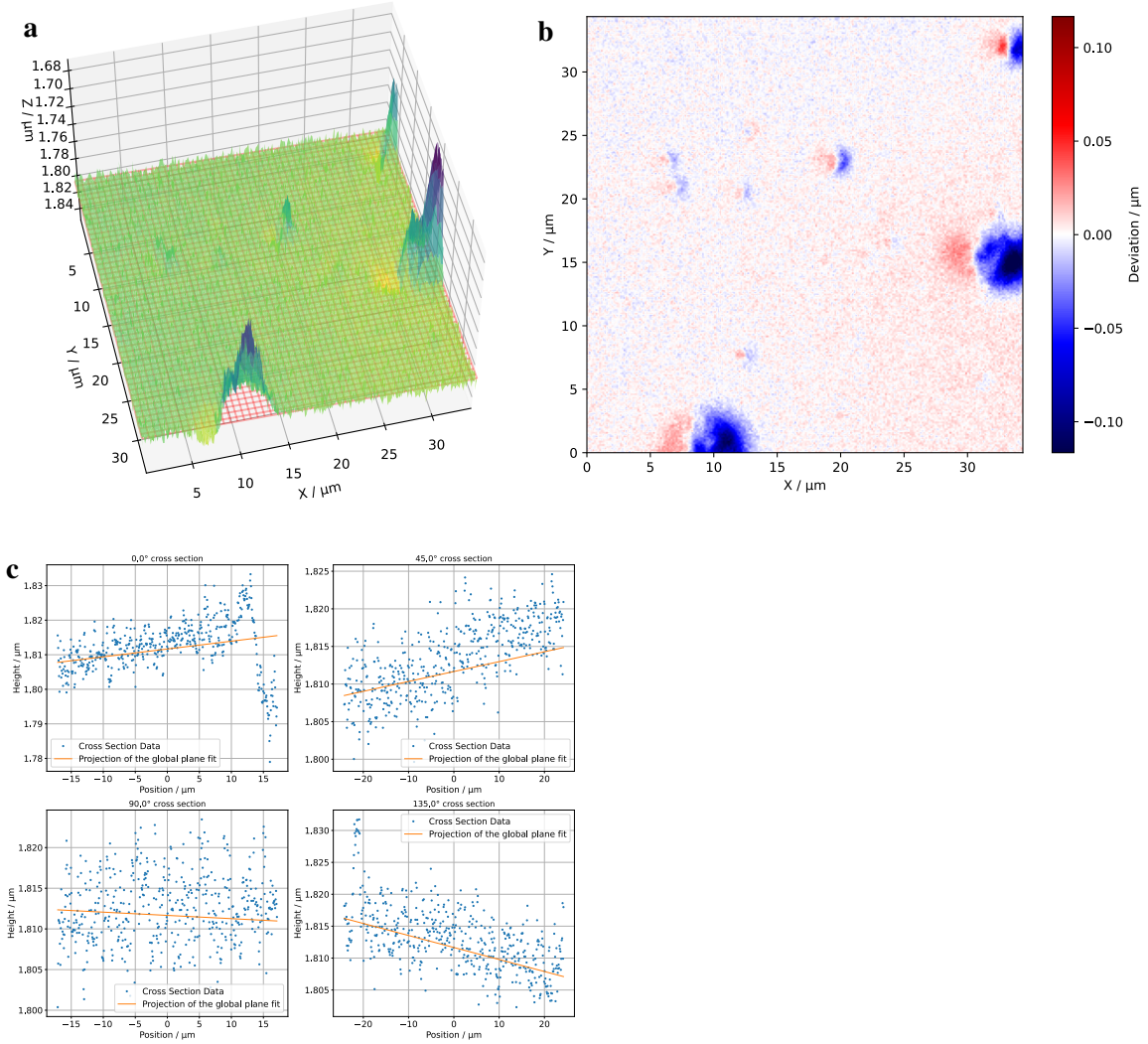

Figure 4.23: Surface reconstruction of a glass substrate using the Hilbert transform method. (a) 3D surface reconstruction with a plane fit to the surface (red mesh). (b) Surface deviation from the plane fit. (c) Cross sections through the surface reconstruction (blue points) and a projection of the global plane fit (orange line).

Hilbert transform method The Hilbert transform method results (Fig. 4.23) show general agreement with the plane fit but exhibit larger reconstruction noise compared to both the direct fit and FDA methods, consistent with simulated data predictions. This demonstrates that robustness against phase offsets comes at the cost of increased surface reconstruction error, particularly evident in real data. The surface deviation heatmap (Fig. 4.23(b)) reveals a distinctive pattern where spikes appear bidirectional, creating shadow-like regions with reduced surface height around elevated features.

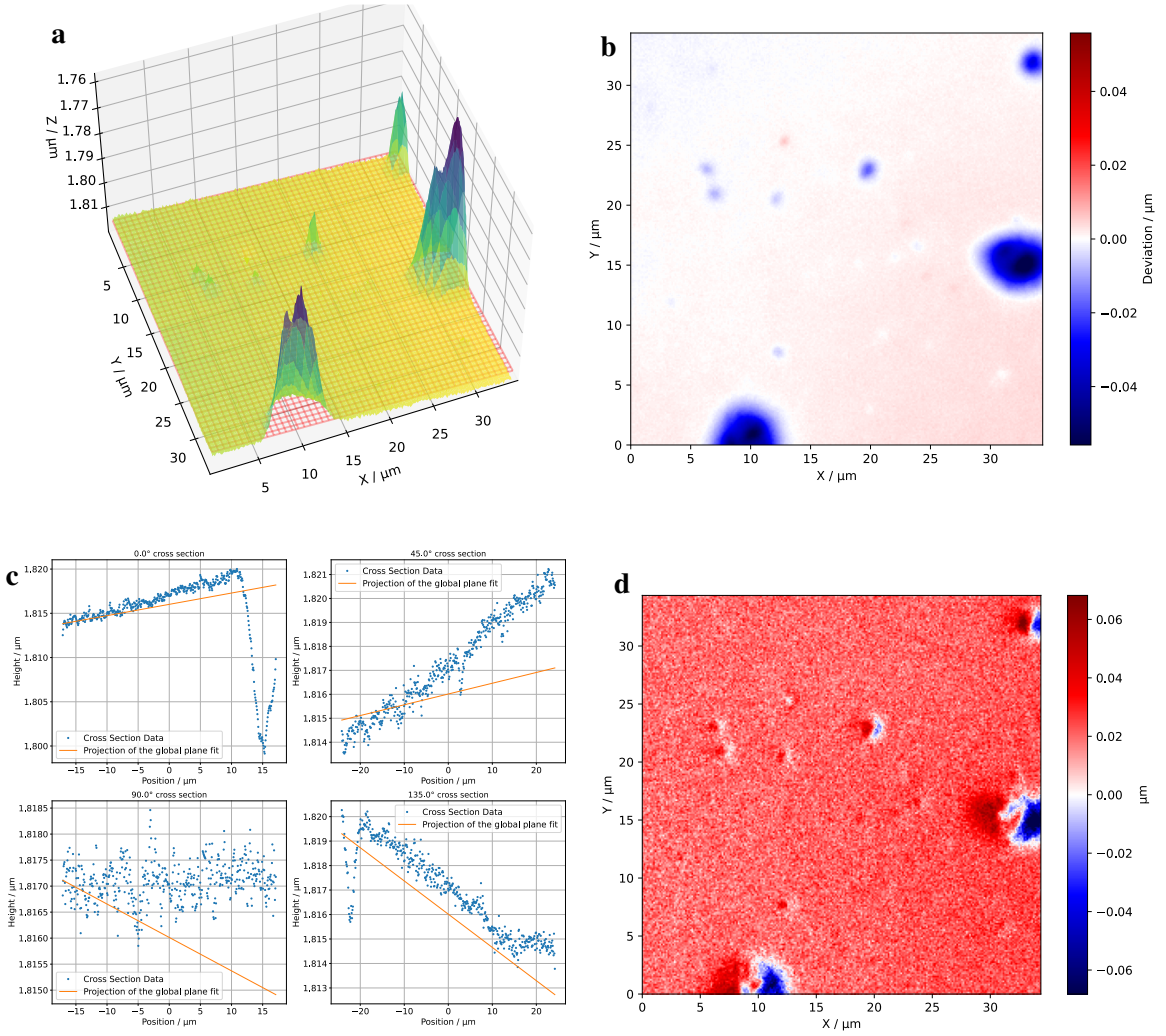

Figure 4.24: Surface reconstruction of a glass substrate using the FDA method. (a) 3D surface reconstruction with a plane fit to the surface (red mesh). (b) Surface deviation from the plane fit. (c) Cross sections through the surface reconstruction (blue points) and a projection of the global plane fit (orange line). (d) Deviation between the fitted central fringe peak position and the envelope peak position determined by the Hilbert transform method.

FDA method The FDA method results (Fig. 4.24) demonstrate performance matching the direct fit method, as anticipated. The surface shows minimal deviation from the plane fit except for dust-induced spikes consistent across all methods. The deviation between reconstructed central fringe peak positions and envelope peak positions (Fig. 4.24(d)) remains nearly constant across the image field within expected Hilbert transform method tolerances, with increases only at spike locations.

Comparative analysis of glass substrate results All three methods perform within their respective expected ranges on the glass substrate, with no significant dependence on distance from the optical axis, confirming that off-axis aberrations do not substantially affect surface reconstruction. The direct fit and FDA methods achieve superior accuracy, while the Hilbert transform method shows

increased noise sensitivity.
Notably, large deviations between fitted/reconstructed central fringe peak positions and Hilbert transform envelope peak positions occur at spike locations. The bidirectional surface deviations observed with the Hilbert transform method are reflected in corresponding deviation maps for both direct fit (Fig. 4.22(d)) and FDA methods (Fig. 4.24(d)). The bidirectional nature of these deviations in the surface reconstruction of the Hilbert transform method suggests that the error might be founded here since dust particles on the glass substrate should not cause bidirectional deviations. It is also striking that the shadows are always cast in the same direction. This made us suspect a misaligned illumination, but careful realignment did not resolve the issue. Curved surfaces appear to degrade interferogram quality, which may explain the increased Hilbert transform errors. However, the mechanism by which the additional noise leads to systematic errors—such as those observed here—remains unclear. Further investigation is strongly recommended to better understand this phenomenon.

Stripped optical fiber The optical fiber consists of a core and cladding surrounded by a protective coating layer. The coating can be stripped residue-free, allowing direct cladding measurement. The cladding consists of nearly pure silica with precisely specified dimensions—the THORLABS fiber used has a cladding diameter of (125 ± 1) µm [74].
Silica fiber measurement presents two primary challenges: low reflectivity (approximately 4 to 6 % [75]) resulting in poor fringe contrast, and curvature-induced contrast reduction at fiber edges. Consequently, measurements are restricted to the central 16 µm × 16 µm region.
Surface radius of curvature is determined by fitting a rotatable cylinder[8]:

$$z(x, y) = z_0 - \sqrt{R^2 - y_{\text{rot}}^2} \tag{4.25}$$

where $y_{\text{rot}} = -(x - x_0)\sin\theta + (y - y_0)\cos\theta$ and parameters include center coordinates (x_0, y_0), z-offset z_0, cylinder radius R, and rotation angle θ.

Direct fit method The direct fit method results (Fig. 4.25) demonstrate excellent cylindrical surface reconstruction. The extracted radius of curvature (61.1 µm) closely matches the expected value (62.5 µm). Surface analysis reveals good adherence to cylindrical geometry with one protruding elevation, likely from dust or residual coating material. A subtle wave-like pattern in the surface deviation heatmap (Fig. 4.25 (b)) shows elevations and depressions up to approximately 5 nm. The asymmetric nature of these patterns around the cylinder axis suggests they represent actual fiber surface features rather than measurement artifacts, since piezo stage errors would produce symmetric patterns. This interpretation is supported by deviations well below the stated 1 µm fiber diameter tolerance.
However, significant systematic deviations (up to approximately ±100 nm) occur between fitted central fringe peak positions and Hilbert transform envelope peak positions (Fig. 4.25(d)), accompanied by systematic drift across the image field.

Hilbert transform method The Hilbert transform method successfully reconstructs the fiber surface (Fig. 4.26) but with larger errors compared to direct fit and FDA methods due to higher

[8] Rotation is restricted to the x, y plane, assuming correct tip-tilt stage adjustment eliminates other rotational components.

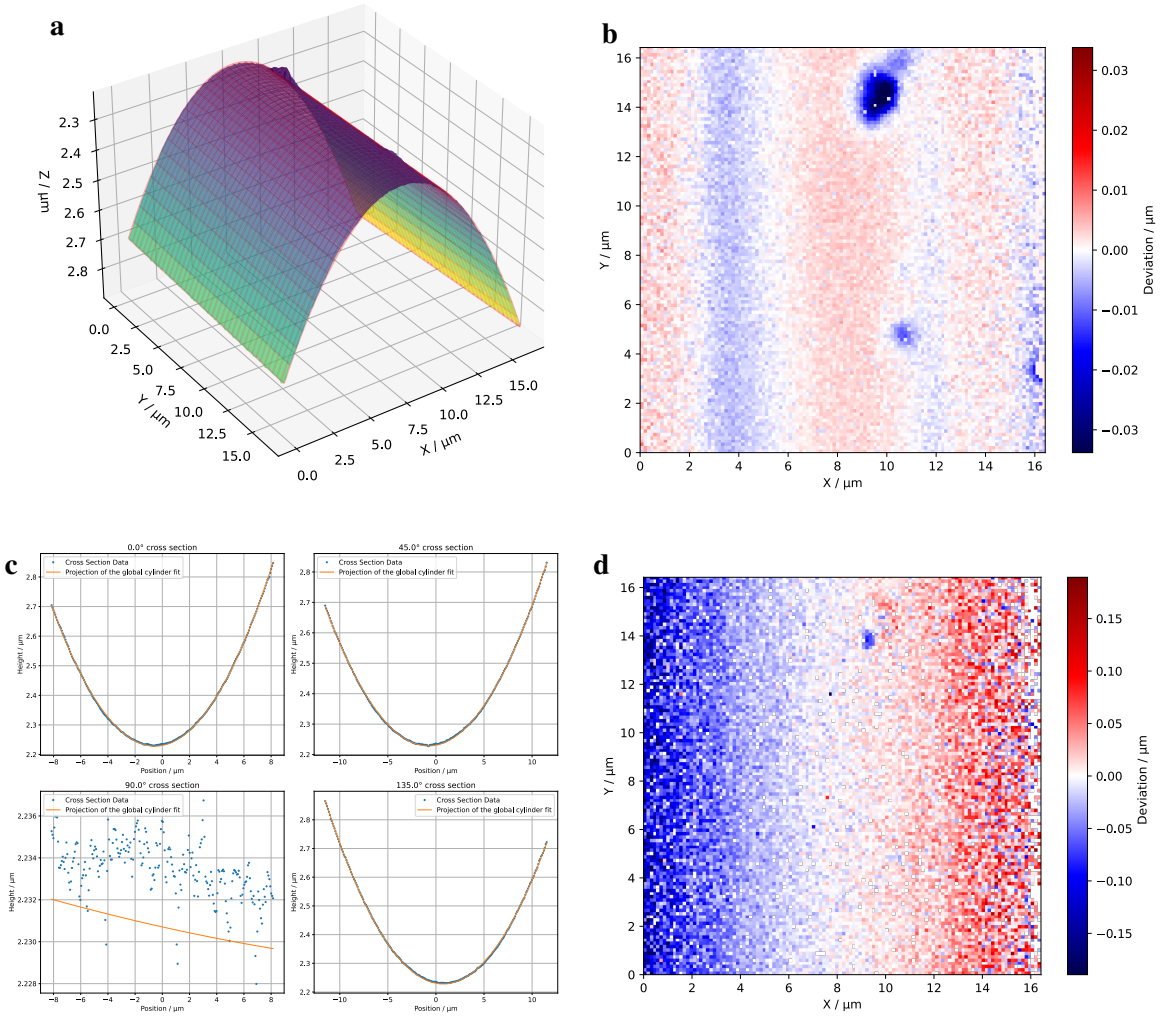

Figure 4.25: Surface reconstruction of a stripped optical fiber using the direct fit method. (a) 3D surface reconstruction with a cylinder fit to the surface (red mesh). (b) Surface deviation from the cylinder fit. (c) Cross sections through the surface reconstruction (blue points) and a projection of the global cylinder fit (orange line). (d) Deviation between the fitted central fringe peak position and the envelope peak position determined by the Hilbert transform method.

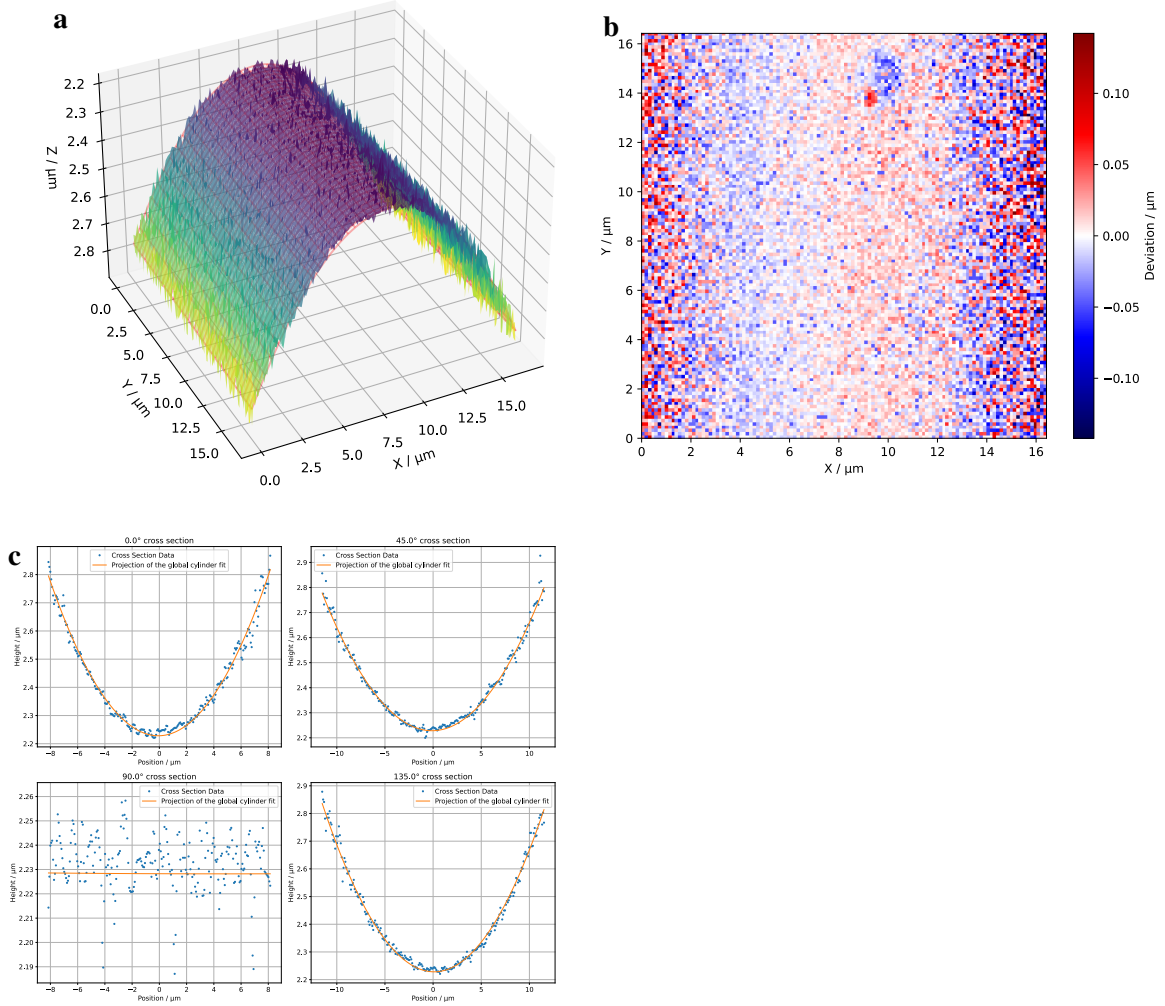

Figure 4.26: Surface reconstruction of a stripped optical fiber using the Hilbert transform method. (a) 3D surface reconstruction with a cylinder fit to the surface (red mesh). (b) Surface deviation from the cylinder fit. (c) Cross sections through the surface reconstruction (blue points) and a projection of the global cylinder fit (orange line).

noise sensitivity. Edge regions, where interferogram contrast is reduced and noise dominates, show particularly pronounced reconstruction errors (Figs. 4.26(b) and 4.26(c)). Despite substantial noise, the fitted cylinder radius (60.6 µm) maintains reasonable agreement with the expected value (62.5 µm).

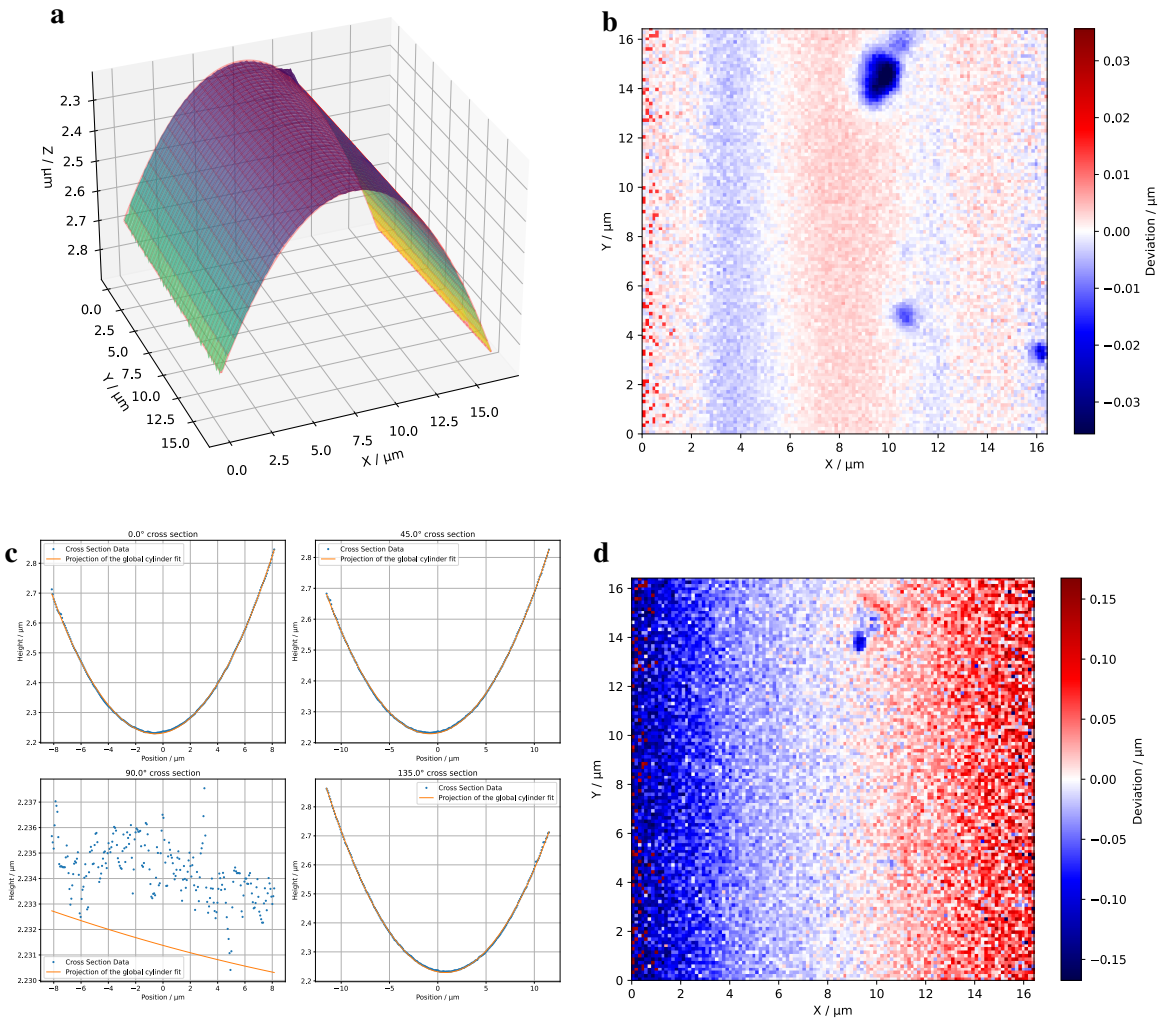

Figure 4.27: Surface reconstruction of a stripped optical fiber using the FDA method. (a) 3D surface reconstruction with a cylinder fit to the surface (red mesh). (b) Surface deviation from the cylinder fit. (c) Cross sections through the surface reconstruction (blue points) and a projection of the global cylinder fit (orange line). (d) Deviation between the fitted central fringe peak position and the envelope peak position determined by the Hilbert transform method.

FDA method The FDA method results (Fig. 4.27) exhibit identical characteristics to the direct fit method, as expected from their theoretical equivalence. The extracted radius of curvature (61.7 µm) demonstrates excellent agreement with the expected value (62.5 µm).

Comparative analysis of optical fiber results The direct fit and FDA methods demonstrate excellent performance on the stripped optical fiber, achieving accurate radius measurements within manufacturing tolerances. The Hilbert transform method, while suffering from higher noise sensitivity, still provides reasonable geometric reconstruction despite challenging measurement conditions.
The systematic deviations between fitted/reconstructed central fringe peak positions and Hilbert transform envelope peak positions (Figs. 4.25(d) and 4.27(d)) mirror observations from the glass substrate spike analysis and highlight the need for further investigations.

Overall real data assessment Both test samples validate the theoretical performance predictions from simulated data. The direct fit and FDA methods consistently achieve superior accuracy and precision, while the Hilbert transform method demonstrates increased noise sensitivity. The systematic phase deviation patterns observed with curved surfaces represent an important area for future investigation to better understand the suspected noise-to-systematic-error conversion mechanisms in Hilbert transform-based reconstruction.

CHAPTER 5

Conclusion and outlook

In summary, this thesis presents the advancements in the design and fabrication of a ferrule-based slip-on micro-optical assembly for fiber integration. Through a stepwise refinement, the ferrule and expansion tube geometries were optimized to ensure sufficient axial alignment and to suppress stray light and parasitic interference. The work shed light on the complexity of establishing an optimal printing strategy for the lens. Therefore, an efficient, robust optimization workflow for rapid future progress was developed. A systematic approach was implemented for optimizing lens figure and mid-spatial-frequency (MSF) waviness, integrating high-throughput surface metrology with automated root mean square error (RMSE) analysis across large print batches. RMSE was employed as the principal metric for assessing optical performance. Initial sample series processed using this workflow exhibited systematic trends in RMSE with changing printing parameters, suggesting consistent improvements with future iterations. An assembly fabricated using a first iteration of optimized parameters was characterized, yielding a beam waist of approximately 5.5 µm at a wavelength of 780 nm, close to the target range of 3 to 5 µm and the simulated value of 4.78 µm. The front focal length was measured at 0.99 mm, in good agreement with both simulation and the target value of 1 mm. However, the beam profile exhibited notable distortions impairing the beam quality, likely attributable to residual MSF waviness on the lens surface.

Dedicated characterization instruments and processing tools were developed or adapted for this work, including a high-precision fiber alignment and insertion stage, a beam profiler, and a scanning white-light interferometer (SWLI). Automation was implemented wherever feasible to maximize measurement throughput and workflow scalability. For the SWLI in particular, comprehensive calibration and performance characterization were conducted to secure reproducible measurements and to quantify instrumental limitations. The accuracy and stability of the developed meterological tools was shown to be sufficient for first figure and MSF waviness assessments.

Despite the substantial performance gains anticipated from the established workflow and the numerous remaining avenues for improvement, it remains uncertain whether the present manufacturing route can ultimately deliver the optical quality required for all intended ultra-cold atom experiments. A rigorous benchmarking against conventional solutions—such as macroscopic glass optics, fiber cavity assemblies or microscopic commercially available GRIN-lenses—should therefore accompany development for each application respectively. If the micro-optical assembly cannot demonstrably surpass these established technologies, the additional fabrication complexity and process overhead may not be justified.

An experiment-ready design and manufacturing strategy has not yet been realized; therefore, a structured roadmap for future work is outlined. Remaining challenges include:

SWLI refinement for improved measurement fidelity. Because the SWLI-based surface metrology is central to the lens characterization and optimization workflow, the remaining instrumental limitations (see Sec. 4.4) should first be mitigated to maximize measurement fidelity.

Lens figure and MSF waviness optimization. After metrology refinement, the print parameter space should be explored systematically with the established workflow, emphasizing interaction effects. A renewed evaluation of contour line strategies, in consultation with Nanoscribe, is recommended given their theoretical potential to improve surface quality significantly.

Validation of RMSE as a performance metric. Once improved surface quality is obtained, the previously initiated correlation study between M^2 and RMSE for different print parameters should be repeated to confirm that RMSE reliably predicts beam quality.

Assessment of alternative fabrication routes or post-processing methods. If surface quality remains inadequate, a change of print configuration should be considered—particularly a higher-magnification objective or additionally a resin with reduced proximity effects for enhanced resolution. Complementary post-processing methods should be evaluated.

Integration trials in an ultracold atom apparatus. After approaching optical performance targets, integration trials should assess installation procedures, vacuum compatibility, influence of cold atom proximity, mechanical stability, alignment tolerances under representative conditions, and fluorescence collection efficiency.

APPENDIX A

Useful information

A.1 Interferogram comparison

Several factors can degrade recorded interferograms and reduce the signal-to-noise ratio. In this study, the primary source of degradation is the curvature of the measured surface. Fig. A.1 compares interferograms obtained from flat and curved surfaces. The interferogram from the flat surface exhibits higher contrast and more distinct fringesv (Fig. A.1(a)). Both the central fringe peak reconstruction and the envelope peak recovery method accurately determine the surface position, yielding nearly identical results. In contrast, the interferogram from the curved surface shows reduced contrast and suppressed fringes (Fig. A.1(b)). While the central fringe peak reconstruction method continues to accurately identify the central fringe position, the envelope peak reconstruction method becomes more susceptible to noise, resulting in surface position estimates that vary between pixels and deviate from those obtained by the central fringe peak method. Additionally, the interferogram from the curved surface displays a greater number of fringes. This phenomenon is not yet fully understood, but it is hypothesized that surface curvature may cause reflections from neighboring pixels to interfere, leading to the appearance of additional fringes.

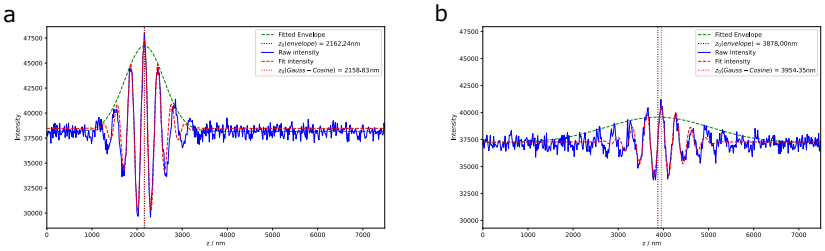

Figure A.1: Comparison of interferograms from flat and curved surfaces. The recorded data is shown in blue, the direct fit in red and the Gaussian fit applied to the Hilbert transform is displayed in green. (a) The flat surface interferogram shows higher contrast and distinct fringes. Reconstructed surface positions are nearly identical. (b) In contrast, the curved surface interferogram exhibits reduced contrast. The envelope peak reconstruction method is more susceptible to noise, leading to varying surface position estimates.

Bibliography

[1] A. Ashkin, J. M. Dziedzic, J. E. Bjorkholm and S. Chu,
Observation of a single-beam gradient force optical trap for dielectric particles,
Optics letters **11** (1986) 288 (cit. on p. 1).

[2] C. Gabbanini, A. Fioretti, A. Lucchesini, S. Gozzini and M. Mazzoni,
Cold rubidium molecules formed in a magneto-optical trap,
Physical review letters **84** (2000) 2814 (cit. on p. 1).

[3] M. Saffman, T. G. Walker and K. Mølmer, *Quantum information with Rydberg atoms*,
Reviews of modern physics **82** (2010) 2313 (cit. on p. 1).

[4] H. Bernien et al., *Probing many-body dynamics on a 51-atom quantum simulator*,
Nature **551** (2017) 579 (cit. on p. 1).

[5] A. W. Young et al.,
Half-minute-scale atomic coherence and high relative stability in a tweezer clock,
Nature **588** (2020) 408 (cit. on p. 1).

[6] K. P. Nayak, J. Wang and J. Keloth,
Real-time observation of single atoms trapped and interfaced to a nanofiber cavity,
Physical Review Letters **123** (2019) 213602 (cit. on p. 1).

[7] L. Reynolds et al., *Direct measurements of collisional dynamics in cold atom triads*,
Physical review letters **124** (2020) 073401 (cit. on p. 1).

[8] D. Gonzalez-Hernandez, S. Varapnickas, A. Bertoncini, C. Liberale and M. Malinauskas,
Micro-optics 3D printed via multi-photon laser lithography,
Advanced Optical Materials **11** (2023) 2201701 (cit. on p. 1).

[9] S. Maruo, O. Nakamura and S. Kawata,
Three-dimensional microfabrication with two-photon-absorbed photopolymerization,
Optics letters **22** (1997) 132 (cit. on p. 1).

[10] R. Guo et al., *Micro lens fabrication by means of femtosecond two photon photopolymerization*,
Optics express **14** (2006) 810 (cit. on p. 1).

[11] T. Gissibl, S. Thiele, A. Herkommer and H. Giessen,
Sub-micrometre accurate free-form optics by three-dimensional printing on single-mode fibres,
Nature communications **7** (2016) 11763 (cit. on p. 1).

[12] T. Gissibl, S. Thiele, A. Herkommer and H. Giessen,
Two-photon direct laser writing of ultracompact multi-lens objectives,
Nature photonics **10** (2016) 554 (cit. on p. 1).

[13] M. Ali, F. Alam, N. Vahdati and H. Butt, *3D-Printed holographic Fresnel lenses*,
Advanced Engineering Materials **24** (2022) 2101641 (cit. on p. 1).

[14] A. Asadollahbaik et al.,
Highly efficient dual-fiber optical trapping with 3D printed diffractive fresnel lenses,
ACS photonics **7** (2019) 88 (cit. on p. 1).

[15] S. Cabrini et al.,
Axicon lens on optical fiber forming optical tweezers, made by focused ion beam milling,
Microelectronic engineering **83** (2006) 804 (cit. on p. 1).

[16] I. V. Reddy, A. Bertoncini and C. Liberale,
3D-printed fiber-based zeroth-and high-order Bessel beam generator, Optica **9** (2022) 645
(cit. on p. 1).

[17] L. Siegle, S. Ristok and H. Giessen,
Complex aspherical singlet and doublet microoptics by grayscale 3D printing,
Optics Express **31** (2023) 4179 (cit. on pp. 1, 28).

[18] P. Nair S, J. Trisno, H. Wang and J. K. W. Yang,
3D printed fiber sockets for plug and play micro-optics,
International Journal of Extreme Manufacturing **3** (2020) 015301,
URL: https://dx.doi.org/10.1088/2631-7990/abc674 (cit. on p. 1).

[19] P. Ruchka et al., *Microscopic 3D printed optical tweezers for atomic quantum technology*,
Quantum Science and Technology **7** (2022) 045011,
URL: https://dx.doi.org/10.1088/2058-9565/ac796c (cit. on p. 1).

[20] M. S. Mc Keever, *Scalable 3D Printing of Micro-Optical Elements for Optical Fibres*,
Masters Thesis: University of Bonn, 2024 (cit. on pp. 2, 27, 29, 32, 35).

[21] M. Prof. Franz Kärtner, *Fundamentals of Photonics: Quantum Electronics*,
URL: https://ocw.mit.edu/courses/6-974-fundamentals-of-photonics-quantum-electronics-spring-2006/download/ (visited on 25/09/2025) (cit. on p. 4).

[22] Nanoscribe, *IP-S Tables*,
URL: https://support.nanoscribe.com/hc/en-gb/articles/360009156133-IP-S-Tables#T:IPSRIndexSolid (visited on 18/08/2025) (cit. on pp. 5, 10, 11, 28, 31).

[23] THORLABS, *P3-780A-FC-2 - Single Mode Patch Cable, 780 - 970 nm*,
URL: https://www.thorlabs.com/thorproduct.cfm?partnumber=P3-780A-FC-2
(visited on 21/08/2025) (cit. on pp. 5, 10, 11).

[24] THORLABS, *G608N3 - Index Matching Gel*,
URL: https://www.thorlabs.de/thorproduct.cfm?partnumber=G608N3 (visited on
14/08/2025) (cit. on p. 9).

[25] M. Schmid, D. Ludescher and H. Giessen, *Optical properties of photoresists for femtosecond 3D printing: refractive index, extinction, luminescence-dose dependence, aging, heat treatment and comparison between 1-photon and 2-photon exposure*, Optical Materials Express **9** (2019) 4564 (cit. on p. 12).

[26] E. Optics, *Optical tests*, URL: https://www.edmundoptics.com/knowledge-center/application-notes/optics/understanding-surface-roughness/?srsltid=AfmBOopgYrNn36BG-IgK2LfglcEFDasEeqg4DsHQvmqQq4e-AylkMkv5 (visited on 21/08/2025) (cit. on pp. 14, 15).

[27] F. Gao, R. K. Leach, J. Petzing and J. M. Coupland, *Surface measurement errors using commercial scanning white light interferometers*, Measurement Science and Technology **19** (2007) 015303 (cit. on p. 14).

[28] Nanoscribe, *3D Printing using Two Photon Polymerization (2PP)*, URL: https://support.nanoscribe.com/hc/en-gb/articles/360008908273-3D-Printing-using-Two-Photon-Polymerization-2PP (visited on 15/08/2025) (cit. on pp. 17, 29).

[29] Nanoscribe, *Printing Microoptics with DeScribe*, URL: https://support.nanoscribe.com/hc/en-gb/articles/360003142594-Printing-Microoptics-with-DeScribe (visited on 16/08/2025) (cit. on pp. 19, 28, 31, 32).

[30] Nanoscribe, *Printing Modes*, URL: https://support.nanoscribe.com/hc/en-gb/articles/214082985-Printing-Modes (visited on 16/08/2025) (cit. on pp. 19, 32).

[31] Avantier, *Peak to Valley and Root Mean Square in Optics*, URL: https://avantierinc.com/resources/technical-article/how-peak-to-valley-and-root-mean-square-values-affect-the-quality-of-your-optic/#:~:text=A%20root%20mean%20square%20(RMS,providing%20the%20overall%20surface%20variation. (visited on 21/08/2025) (cit. on p. 21).

[32] AstroReflect, *Optical tests*, URL: https://www.astroreflect.com/optical-tests/ (visited on 21/08/2025) (cit. on p. 21).

[33] A. Rondepierre, D. Oumbarek Espinos, A. Zhidkov and T. Hosokai, *Propagation and focusing dependency of a laser beam with its aberration distribution: understanding of the halo induced disturbance*, Optics Continuum **2** (2023) 1351 (cit. on p. 23).

[34] J. M. Tamkin and T. D. Milster, *Effects of structured mid-spatial frequency surface errors on image performance*, Applied optics **49** (2010) 6522 (cit. on p. 23).

[35] Nanoguide, *Printing with the 3D Microfabrication Solution Set Small Features (3D SF)*, URL: https://support.nanoscribe.com/hc/en-gb/articles/360002424414-Printing-with-the-3D-Microfabrication-Solution-Set-Small-Features-3D-SF (visited on 01/09/2025) (cit. on p. 28).

[36] B. Jung, C. K. Ober and M. O. Thompson, *Controlled roughness reduction of patterned resist polymers using laser-induced sub-millisecond heating*, Journal of Materials Chemistry C **2** (2014) 9115 (cit. on p. 28).

[37] D. Stachanow, *Manufacturing Q-optimized polymer-based mechanical resonators for cavity optomechanics with 3D direct laser writing*, Masters Thesis: University of Bonn, 2024 (cit. on pp. 29, 30).

[38] A. Faßbender, *Adding New Functionalities to Optical Fiber Cavities by Direct Laser Writing*, PhD Thesis: University of Bonn, 2023 (cit. on pp. 29, 31).

[39] M. Deubel et al., *Direct laser writing of three-dimensional photonic-crystal templates for telecommunications*, Nature materials **3** (2004) 444 (cit. on p. 29).

[40] Nanoscribe, *3D Microfabrication Solution Set Medium Features (3D MF)*, URL: https://support.nanoscribe.com/hc/en-gb/articles/360001659613-3D-Microfabrication-Solution-Set-Medium-Features-3D-MF (visited on 13/08/2025) (cit. on p. 30).

[41] Nanoscribe, *Technical Parameters - Laser*, URL: https://support.nanoscribe.com/hc/en-gb/articles/360012401739-Technical-Parameters#Ch:Laser_parameters (visited on 16/08/2025) (cit. on p. 30).

[42] Nanoscribe, *Adjusting the Dose*, URL: https://support.nanoscribe.com/hc/en-gb/articles/360001159713-Adjusting-the-Dose (visited on 15/08/2025) (cit. on p. 31).

[43] Nanoscribe, *3D Printing using Two Photon Polymerization (2PP)*, URL: https://support.nanoscribe.com/hc/en-gb/articles/360008908273-3D-Printing-using-Two-Photon-Polymerization-2PP#Ch:Linewidth (visited on 16/08/2025) (cit. on p. 31).

[44] Nanoscribe, *Shape Accuracy*, URL: https://support.nanoscribe.com/hc/en-gb/articles/360008483913-Shape-Accuracy (visited on 16/08/2025) (cit. on p. 32).

[45] THORLABS, *RB13M/M - 3-Axis RollerBlock*, URL: https://www.thorlabs.com/thorproduct.cfm?partnumber=RB13M/M (visited on 13/08/2025) (cit. on p. 32).

[46] E. Scientific, *MDE709 - Fibre Holder*, URL: https://www.elliotscientific.com/178-Fibre-Holders/Elliot-Martock-MDE709-Fibre-Holder-Bare-Mechanical-for-Elliot-Gold-Series-XYZ-Flexure-Stages (visited on 13/08/2025) (cit. on p. 32).

[47] DinoLite, *Dino-Lite AM4113T*, URL: https://asset.conrad.com/media10/add/160267/c1/-/en/001642351DS01/datenblatt-1642351-dino-lite-digital-mikroskop-digitale-vergroesserung-max-220-x.pdf (visited on 13/08/2025) (cit. on p. 32).

[48] Zeiss, *Stemi 305*, URL: https://www.micro-shop.zeiss.com/de/de/system/stemi+305-stemi+305-stereomikroskope/10285/#variants (visited on 25/08/2025) (cit. on p. 32).

[49] M. Saravanan, *Mode-Matched Fiber Fabry-Pérot Cavities for Quantum Technologies*, Masters Thesis: University of Bonn, 2020 (cit. on p. 34).

[50] Newport, *Motorized Linear Stage, Miniature, 25 mm Travel, DC Motor, M2 and M3*, URL: https://www.newport.com/p/MFA-CC (visited on 12/08/2025) (cit. on p. 34).

[51] E. Optics, *Mitutoyo Plan Apo NIR unendlich korrigiertes Objektiv, 20X*, URL: https://www.edmundoptics.de/Catalog/Specsheet/Specsheet/6834 (visited on 12/08/2025) (cit. on p. 34).

[52] THORLABS, *DCC1545M - CMOS Camera*, URL: https://www.thorlabs.com/_sd.cfm?fileName=ITN000563-D02.pdf&partNumber=DCC1545M (visited on 12/08/2025) (cit. on p. 34).

[53] P. De Groot, *Principles of interference microscopy for the measurement of surface topography*, Advances in Optics and Photonics **7** (2015) 1 (cit. on pp. 40, 43, 47).

[54] THORLABS, *QTH10(/M) Quartz Tungsten-Halogen Lamp Manual*, URL: https://www.thorlabs.com/_sd.cfm?fileName=DOC-101265.pdf&partNumber=QTH10 (visited on 18/07/2025) (cit. on p. 40).

[55] N. Ida, "Microwave and Millimeter wave nondestructive testing and evaluation", *Handbook of Advanced Non-Destructive Evaluation*, Springer, 2019 1 (cit. on pp. 41, 43, 44).

[56] E. Optics, *50X Nikon CF IC Epi Plan DI Mirau-interferenceobjective*, URL: https://www.edmundoptics.de/p/50x-nikon-cf-ic-epi-plan-di-interferometry-objective/16069/ (visited on 18/07/2025) (cit. on p. 41).

[57] P. Instrumente, *PIFOC High-Precision Objective Scanner P721 data sheet*, URL: https://www.physikinstrumente.co.uk/en/?type=5600&downloadUid=317&downloadFileUid=320 (visited on 18/07/2025) (cit. on pp. 41, 53, 55).

[58] THORLABS, *CS126MU - Kiralux 12.3 MP Monochrome CMOS Camera Manual*, URL: https://www.thorlabs.com/_sd.cfm?fileName=ITN002518-D02.pdf&partNumber=CS126MU (visited on 18/07/2025) (cit. on pp. 41, 51).

[59] E. Optics, *Nikon Tubuslinse 200 mm Specifications*, URL: https://www.edmundoptics.de/p/nikon-200mm-tube-lens/15374/ (visited on 18/07/2025) (cit. on p. 41).

[60] THORLABS, *MAX313D/M - 3-Axis NanoMax Stage, Differential Drives, No Piezos, Metric Manual*, URL: https://www.thorlabs.com/_sd.cfm?fileName=10997-D02.pdf&partNumber=MAX313D/M (visited on 18/07/2025) (cit. on p. 41).

[61] Newport, *M-GON40-U Anti-Backlash Goniometric Rotation Stages*, URL: https://www.newport.com/f/anti-backlash-goniometric-rotation-stages (visited on 18/07/2025) (cit. on p. 41).

[62] C. Akcay, P. Parrein and J. P. Rolland, *Estimation of longitudinal resolution in optical coherence imaging*, Applied optics **41** (2002) 5256 (cit. on pp. 43, 53).

[63] P. Lehmann, S. Tereschenko and W. Xie,
Fundamental aspects of resolution and precision in vertical scanning white-light interferometry,
Surface Topography: Metrology and Properties **4** (2016) 024004 (cit. on p. 43).

[64] P. Lehmann, "Systematic effects in coherence peak and phase evaluation of signals obtained with a vertical scanning white-light Mirau interferometer",
Optical Micro-and Nanometrology in Microsystems Technology, vol. 6188, SPIE, 2006 258 (cit. on p. 43).

[65] P. Lehmann, *Vertical scanning white-light interference microscopy on curved microstructures*,
Optics letters **35** (2010) 1768 (cit. on p. 43).

[66] J. Coupland, R. Mandal, K. Palodhi and R. Leach,
Coherence scanning interferometry: linear theory of surface measurement,
Applied optics **52** (2013) 3662 (cit. on p. 43).

[67] R. Su, J. Coupland, C. Sheppard and R. Leach, *Scattering and three-dimensional imaging in surface topography measuring interference microscopy*,
Journal of the Optical Society of America A **38** (2021) A27 (cit. on p. 43).

[68] P. Pavliček and V. Michalek,
White-light interferometry—Envelope detection by Hilbert transform and influence of noise,
Optics and lasers in engineering **50** (2012) 1063 (cit. on p. 46).

[69] P. De Groot and L. Deck,
Surface profiling by analysis of white-light interferograms in the spatial frequency domain,
Journal of modern optics **42** (1995) 389 (cit. on pp. 47, 48).

[70] D. W. Kammler, *A first course in Fourier analysis*, Cambridge University Press, 2007 (cit. on p. 48).

[71] E. Optics, *2" x 2" Positive, USAF 1951 Hi-Resolution Target*,
URL: https://www.edmundoptics.com/p/2-x-2-positive-1951-usaf-hi-resolution-target/15108/?srsltid=AfmBOopdxGC0zMuHoBDGJmnGTQYT5zzPqXQtcoHWHzXiEtqYgt-uns_3 (visited on 19/07/2025) (cit. on p. 51).

[72] O. Optics, *Red Tide USB650 Fiber Optic Spectrometer*,
URL: https://www.oceanoptics.com/wp-content/uploads/2024/12/USB-650-Red-Tide-Installation-and-Operation-Instructions.pdf (visited on 06/08/2025) (cit. on p. 52).

[73] K. Hieda, T. Maruyama and F. Narusawa, "P-15.3: The Importance of Centroid Wavelength for the Image Quality Evaluation of Laser Displays", *SID Symposium Digest of Technical Papers*, vol. 50, Wiley Online Library, 2019 1002 (cit. on p. 52).

[74] THORLABS, *S630-HP - Single Mode Optical Fiber, 630 - 860 nm, Ø125 µm Cladding*,
URL: https://www.thorlabs.com/_sd.cfm?fileName=TTN333622-S01.pdf&partNumber=S630-HP (visited on 06/08/2025) (cit. on p. 60).

[75] R. A. Synowicki, B. D. Johs and A. C. Martin,
Optical properties of soda-lime float glass from spectroscopic ellipsometry,
Thin Solid Films **519** (2011) 2907 (cit. on p. 60).

Acknowledgements

I would like to thank Sebastian Hofferberth for providing me with the opportunity to conduct my master's thesis within his research group. I appreciate the support, the constructive and helpful input, but also the freedom I got during my work. I also wish to thank my second supervisor, Prof. Dr. Linden, for insightful discussions and granting access to the Nanoscribe printer. Special thanks are extended to Hannes Pfeifer and the members of the FCO group for their assistance with the project and for the nice working atmosphere. I am particularly grateful to Gian-Marco and Paul for their support during laboratory work and for engaging in valuable scientific discussions. Furthermore, I thank Wolfgang for his fruitful discussions and the enlightenments included herein. Finally, I acknowledge the entire NQO group for their support and for making my time during these studies both productive and enjoyable.